REDUCING BARRIERS TO PET NEUROIMAGING RESEARCH USING ACCESSIBLE AND TRANSLATABLE TOOLS

By

Kylie Renae Smith

A DISSERTATION

Submitted to
Michigan State University
in partial fulfillment of the requirements
for the degree of

Biomedical Engineering—Doctor of Philosophy

2023

ABSTRACT

Molecular imaging is a critical tool for the management of neurodegenerative disease. In particular, positron emission tomography (PET) has provided new ways to identify distinct subtypes in Alzheimer's Disease, inform disease management, and monitor treatment progress. However, the power of PET imaging is challenged by limitations to accessibility that hinder its adoption. Opportunities to reduce risk of failure and improve the efficiency of PET research are of high priority, given the high costs of conducting a PET study and the urgent need for improved imaging techniques and interventions. This dissertation describes the design, development, and implementation of custom research tools to improve efficiency for pre-clinical PET imaging. A modular multi-rodent imaging bed was designed and validated for high throughput PET/MR, then de-risked for commercialization. Commercialization activities included evaluation of candidate materials for interference in pre-clinical imaging modalities, a value-in-use study, and incorporation of desirable features identified through informational interviews with end users. Anatomically derived 3D-printed phantoms were used to develop methods to track nose-to-brain transfer of radioactive imaging agents by PET, which were then applied in nonhuman primates. Using this approach, we were able to quantitatively determine the distribution of F-18-FB-insulin throughout the brain of Cynomolgus Macaques following nose-to-brain delivery. Clinically relevant dosing tools were prioritized to facilitate rapid translation to humans for evaluation of nose-to-brain insulin as a therapeutic for Alzheimer's Disease. Together, these methods are anticipated to reduce barriers to conducting and advancing PET neuroimaging research.

This dissertation is dedicated to my father, Daniel James Smith II, who taught me the beauty in curiosity and skepticism; to my mother Samara Kiriazis-Bowling, who taught me the power in showing up exactly as you are; and to my fellow students of error and dreamers of a better future.

ACKNOWLEDGEMENTS

This body of work could not have been written without the help of countless mentors, colleagues, and friends. I will name some of them here.

First, I'd like to acknowledge Crameri, Shephard, and Heron for providing the batlow and batlowK colormaps that represent data intuitively, accessibly for colour-vision deficient and color-blind people, and without visual distortion. Figures made using Biorender (Biorender.com) and Crameri colorbars are distributed throughout this document, including citations for the Crameri manuscripts.

Thank you to Dr. Michael Plazcek at the Athinoula A. Martinos Center for Biomedical Imaging, (The Institute for Innovation in Imaging, Massachusetts General Hospital and Harvard Medical School) for graciously sharing the 3D-printed bite bar design cited in Chapter 2.

I'd like to acknowledge the Molecular Imaging Department and Radiochemistry team at Charles River Laboratories for their help with primate handling and image acquisition, and the team at inviCRO for their help preparing the imaging data. Thank you especially to Scott Haller, Dr. Gwendolyn A. Marriner, and Ken Zasadny from these groups.

Thank you to the 3D Printing Core at the Institute for Quantitative Health Science and Engineering (Michigan State University), especially Dr. Cody Pinger, Dr. Nathan Redman, and Stephen Branch. I'm grateful for the literal hours spent in discussion and at the printer. Thank you, as well, for wall ball.

Thank you to the individuals that provided their expertise for the commercialization project, including students in the Michigan State University Library Makerspace, Dr. Alessandra Hunt, Beth Kenyon, and Jacob Reynolds. I'd also like to acknowledge Dr. Joe Affholter and Wei-an Ou with the Michigan Translational Research and Commercialization Program for their time, guidance, and gleeful support in commercialization efforts for the high throughput imaging system. Similarly, a big thank you is extended for Dr. Jon Debling at the Technology Transfer Office at Michigan State University. It has been my pleasure to work with you.

I'd like to separately acknowledge the molecular imaging researchers that shared their time with me for informational interviews – I'm very appreciative for your insights. Thank you very much to Dr. Felix Gremse for his thoughts and discussions regarding image processing for data gathered using our high throughput tools. A very warm thank you to the gentlemen at Phantech, LLC – Justin Jeffery and Dr. Ben Cox. I'm grateful for your warm welcome to the field and for your generosity in guidance and laughter. I will always value that.

A whole heaping mound of gratitude is reserved for the Purcell Lab, Shapiro Lab, and the Advanced Molecular Imaging Facility at the Institute for Quantitative Health Science and

Engineering. Thank you for sharing your stereotaxic frames and more – I couldn't have done much of my favorite work without you. MSU has a research agreement with Bruker BioSpin, and I appreciate their guidance with PET image acquisition and analysis. Thank you especially to Dr. Christiane Mallet for her help designing magnetic resonance imaging sequences with me, and for her patience when I would misplace my notes. You are a wonderful teacher and mentor. And finally, a very deep thank you to my colleague and friend, Jeremy Hix. I wish that every trainee could have someone in their corner as fiercely supportive as Jeremy has been for me.

I'd like to acknowledge Fan Lab members Jacob Richardson, Yongcheng Lu, Dr. Janaki Ramulu, who each contributed to the success of the nose-to-brain F-18-FB-insulin project through preparation or analysis of precursor compounds, for which I am very grateful. Thank you to Dr. Robert Kessler and Dr. John Gerdes for their warm and insightful guidance on the F-18-FB-insulin project over the years. I'm deeply thankful to Dr. Jinda Fan as well, for sternly believing in me, sharing with me, and for his hard work in the radiopharmacy and our office chemistry lectures.

I would have nothing to show if not for my lab mates, including Mitchell Gabalski, Kate Rodgers, Tanvi Sharma, Ece Erder, Lucy Xu, Dr. Satyendra Singh, Amanda Cournoyer, Chelsea Nayback, and Nate Kauffman. You have all made this time memorable. Thank you especially to Angela Asor for being my partner in high performance (pain) liquid chromatography. And similarly, to Kate Rodgers and her fiancé Colin Brown for their friendship, gingerbread party hosting skills, and help with my dog on long lab nights.

Thank you to Dr. Neil Robertson for his chemistry lectures, discussions, and for being my on-call editor.

My deepest, warmest, and most humbling thank you is saved for my mentor, Dr. Kurt Zinn. I don't have the words to express my gratitude. Perhaps I'll find them by the time you've finished reading this dissertation.

To Dr. Zinn, to my loved ones, to my lab mates, and to all those named here – thank you. I could not be more grateful.

TABLE OF CONTENTS

CHAPTER 1: INTRODUCTION

1.1 The Burden of Alzheimer's Disease

Alzheimer's Disease (AD) is the most common neurological disorder in the United States[1]. AD is behaviorally characterized by deficits in language, memory, and thinking that make it difficult to care for oneself in late-stage disease. AD is physiologically characterized by atrophy of the medial-temporal lobe, reduced cerebral glucose metabolism, and abnormally high accumulation of amyloid-beta and tau throughout the brain[2,3]. Positron emission tomography (PET), cerebrospinal fluid (CSF) sampling, and magnetic resonance imaging (MRI) are capable of detecting the hallmark protein accumulations and atrophied tissue that define AD. Currently, only the latter two are used in the diagnostic process[3,4], supplemented by cognitive testing and examination of medical history[5]. According to the 2023 Alzheimer's Facts and Figures report, 1 in 9 (8-11%) Americans 65 years or older find themselves in this patient group[2].

Unfortunately, diagnostic methods that rely on the presence of cognitive decline or cortical atrophy can only identify patients with irreversible neurodegeneration. There are currently no cures, preventatives, or early detection methods to halt or slow the progression of AD. This is alarming due to the intense burden that AD poses on the diagnosed, the healthcare system, and care providers. In 2022, caregiving resources provided to individuals with Alzheimer's and other dementias was valued at $339.5 billion dollars and 18 billion hours in the United States[2]. The situation is expected to worsen as the largest at-risk population (65+ years of age) grows from 58 million in 2021 to 88 million in 2050[2]. In light of these projections, the urgency of preventing or slowing AD pathology in at-risk individuals is clear.

Brain changes suspected to drive AD development begin years before the onset of clinical symptoms, providing a window of opportunity for intervention. An intervention that delays progression from preclinical to clinical AD by 5 years would be expected to reduce the incidence rate by 57%, and therefore associated costs and burdens[6]. Several studies have shown that abnormal amyloid-beta accumulation can be detected by PET as early as 10-15 years in advance of an AD diagnosis[7-9]. However, lack of regulatory approval, limited familiarity with PET imaging by physicians, and limited access to PET scanners limit use of this technique despite demonstrated diagnostic superiority over existing methods[4,5,10].

1.2 Positron Emission Tomography as a Critical but Limited Tool in the Fight Against Neurodegenerative Disease

1.2.1 A Primer on Positron Emission Tomography (PET)

Positron emission tomography (PET) is one of several clinical techniques used to detect radioactive materials. Radioactive isotopes (termed radioisotopes) have unstable nuclei that become more stable by releasing energy through a spontaneous process called radioactive decay. Energy is released from the atomic nucleus of the radionuclide as radiation in the form of high-energy gamma photons ($< 10^{-11}$ m wavelength) or subatomic particles, such as an electron, positron, or alpha particle (two protons and two neutrons)[11]. Interactions between the radiation and surrounding material will depend on their respective properties, which can be exploited for therapy and imaging. For example, the size of alpha particles makes alpha-emitters effective radiotherapeutics by damaging nearby DNA but limit tissue penetration to 0.03 mm in human tissues. Alternatively, the photons generated through decay by positron and gamma emission are massless, chargeless, and capable of traveling through the body to reach surrounding imaging detectors[12]. PET and single photon emission computed tomography (SPECT) detect these forms of decay following patient injection of a radiopharmaceutical – a molecule with an incorporated or attached radionuclide – to answer questions about patient physiology.

PET images describe the distribution of a positron-emitting radionuclide in space and time with high sensitivity. The collision of a positron ejected during decay and a nearby electron will result in annihilation of both, producing two gamma photons (511 keV) that travel in opposite directions from the annihilation event. Annihilation photons pass through tissue to reach a ring of scintillation detectors surrounding the patient or sample. The absorption of radiation results in light emission by the scintillator, which can be recorded and timestamped. When two photons are detected opposite one another within 4-20 nanoseconds[13], they are assumed to have originated from the same decay event. The source of decay can be estimated to exist along the path between the detectors in question, termed “line of response”. Decay events and their respective lines of response are recorded for pre-determined periods of time, which may be summed to form a single image or collected in series as dynamic data. Overlapping lines of response create contrast in an image to describe the behavior of the radioisotope over space and time. The number of radioactive atoms present can also be determined by calculating the rate of disintegrations in a region per unit time, where disintegration is defined as the decay of a single radioactive atom (1

Becquerel = 1 disintegration/second). Positron emitters can be detected by PET imaging at picomolar concentrations of radionuclide, making it possible for a subject to undergo several imaging sessions without concerns of toxicity or adverse effects[12]. Thus, PET is a powerful tool for the sensitive and quantitative detection of positron-emitting radionuclides.

PET can be used in combination with a variety of existing instrumentation for flexibility in methodology. A range of positron emitters are available with decay rates suitable to image the kinetics of small molecules, peptides, and drugs. By incorporating or attaching the radionuclide to the appropriate molecule, PET can provide physiologically relevant information about the presence and function of particular tissue types using targeted (substrates, receptor ligands, or reporter probes) or nonspecific (perfusion, metabolism) imaging probes. PET data can be strengthened through combination with anatomical imaging techniques to visualize tissues with different densities or relaxation properties via computed tomography (CT) or magnetic resonance imaging (MRI), respectively. The combination of more than one imaging technique is referred to as multi-modal or multi-modality imaging and can be achieved using scanners that perform both imaging methods simultaneously, in sequence, or through the manual co-registration of separately acquired anatomical and PET scans. Anatomical images enable motion and attenuation corrects to PET data, as well as providing regional and/or anatomical context. Instrument operators set the image size, resolution, and field of view for CT, MRI, and PET, enabling increasing flexibility in spatial resolution with large field of view PET scanners becoming increasingly available (e.g., 8 x 15 cm in Bruker's small animal scanner[14], whole body for humans[15]). Additionally, the instrument operator to determines the quantity and duration of PET acquisition frames, providing flexibility in imaging timepoints and temporal resolution. Thus, multi-modal PET/CT or PET/MRI imaging contrasts with other imaging techniques by providing both functional and anatomical information with high sensitivity. Additionally, the sensitivity and accuracy of quantitative measurements by PET can be validated by gamma counters and dose calibrators, which are common to nuclear medicine labs. This quantitative toolset supports robust, objective comparisons across time points, treatment groups, experiments, and models. These qualities make PET a unique and competitive tool for use in disease detection and management.

PET is a relatively new technique, with the first human scanner built only 50 years ago in 1973[16]. PET hardware and methodologies are being continuously improved, resulting in better image quality, sensitivity[17], and larger fields of view (FOV)[15,18]. Today, PET imaging is used for several clinical applications, including neuroimaging[10,16,19,20], the detection of cancer metastases[21-24],

identification of regions with altered metabolism (cancer, inflammation)[25,26] or osteogenesis[27-31], and assessment of myocardial perfusion[27,32].

1.2.2 PET as a Rising Star for Differential Diagnosis and Treatment

Data-driven approaches to integrate and synthesize neuroimaging results have uncovered new knowledge of AD subtypes that will likely inform future care. Currently only MRI is approved for reimbursement as part of the diagnostic process for AD, but research is showing that PET imaging methods aid in clarifying disease pathology and improving diagnostic accuracy[5,24,33-37]. Recent PET findings have shifted the spotlight from amyloid-beta to tau as the primary predictor of cognitive decline[34,38]. Notably, the most accurate predictions of future cognitive decline were made using combined tau and amyloid imaging results[38]. Other multi-modal biomarker studies have revealed MR-detected patterns of cortical atrophy through clustering[39], which were then further subdivided according to regional hypometabolism patterns as determined by F18-FDG[40]. Similarly, patient groups that vary in behavioral deficits and patterns of cortical tau distribution determined by PET have been identified[10]. Together, these results demonstrate the power of integrating multi-modal imaging data with existing clinical methods for AD diagnosis.

The most striking example of the utility of PET in AD management comes from the Imaging Dementia-Evidence for Amyloid Scanning (IDEAS) study, which enrolled 16,008 subjects to investigate whether amyloid PET (PET imaging using amyloid-targeting imaging probes) altered the course of treatment for mild cognitive impairment (MCI) and dementia patients of unknown etiology. At the time of enrollment, patients had already undergone a standard clinical assessment for diagnosis (e.g., cognitive testing, head scan via computed tomography or MRI, lab testing, review of medical history). Within 90 days, dementia specialists made an initial diagnostic assessment, patients underwent amyloid PET scanning, and an updated assessment was given after reviewing the results of the scan. The inclusion of an amyloid PET scan changed the course of disease management for 60.2% of MCI patients and 63.5% of dementia patients. Further, 25.1% of patients that would have received an AD diagnosis were shifted to a non-AD dementia determination following a negative amyloid PET scan, and 10.1% of patients received an updated diagnosis in the opposite direction[5]. These results provide evidence of the critical role of PET imaging in identifying the underlying pathology of disease, which can be otherwise difficult to differentiate from similar clinical presentations.

PET imaging enables scientists to develop a disease profile that is specific to the patient, enabling the selection of a tailored treatment plan that targets the underlying dysfunction. However, PET imaging biomarkers face limitations to use by clinicians due to inconsistent reimbursement policies, high costs, and limited availability and technical understanding[4]. These limitations must be addressed given the need to correctly prioritize the best suited management plan, as failure to do so can result in irreversible disease progression and patient loss as a result.

1.2.3 Barriers Limiting PET Use

Widespread adoption of PET as a clinical and research tool faces several challenges, including the prohibitively high costs of acquiring and operating a PET scanner. PET scanners are among the most expensive imaging instruments on the market[41], with clinical standalone instruments ranging $1-1.5 million[12,42], PET/CT scanners ranging $1.7-2.5 million[4,5], and total-body PET/CTs priced near $10 million per unit[4]. Small animal PET scanners, which are used to develop novel radiopharmaceuticals and imaging methods for use in research or clinical translation (termed "pre-clinical imaging"), can be acquired for $400,000-1.2 million[43]. Unless radioisotopes are purchased and transported to the site of use, resulting in sample decay and a smaller imaging window[44], institutions need the means to produce positron-emitters and chemically incorporate them into imaging agents on site. Some hospitals and laboratories have a cyclotron (or generator) and radiopharmacy for production of radiopharmaceuticals, which also require substantial investments in infrastructure and personnel to install, use, and maintain. Additional costs comprising facility construction, regulatory compliance, and ancillary equipment can range from $1-6.2 million depending on the services provided at the facility[42]. Together, costs to build and launch a PET imaging center can reach an estimated $3.5-15 million[15,42,45].

Operational costs and risk in cost recovery pose additional hurdles to PET utilization beyond initial acquisition and installation investments. The technical complexity of PET requires trained research and medical professionals to operate the scanner, acquire and process data, and appropriately interpret the results. The cost of a single procedure, including man-hours, consumables, and other operational costs, is estimated to range from $1,000-3,000 depending on procedure type. Over a year, operational costs can amount to $1 million or more for well-equipped facilities[42]. Maintenance of revenue streams capable of offsetting operational expenses is challenged by limited throughput[42] and inconsistent reimbursement by insurance providers[4,5]. For example, a 2016 survey of 39 PET/MRI scanning sites reported procedure lengths up to 2

hours, limiting their average throughput to 8-12 patients/day[46]. Fewer imaging procedures conducted per day yields fewer opportunities for revenue through reimbursement. Pre-clinical PET imaging faces similar constraints related to high costs and low throughput. Animal subjects are traditionally imaged one at a time, although some solutions to improve efficiency have been proposed[47-49]. Depending on the duration of the imaging procedure(s) and sample size, pre-clinical PET users may require more scanning time than clinical users to complete a study. Increased scanning time increases study costs by way of hourly charges for scanner use and man-hours to complete the study. Finally, researchers must pay to purchase and house their subjects, as well as train personnel to use the scanner. However, unlike in the clinical setting, funding for pre-clinical PET studies comes from grants and awards, which are competitive and limited in duration. The substantial time and monetary investments required to conduct a PET study may limit use of the technique by researchers even when a facility is available for use. Thus, risk of insufficient reimbursement for PET operational costs ($1-2 million anually[12,42]) may preclude institutions from utilizing or establishing a PET center. Efforts to mitigate the substantial time and monetary costs of PET scanner acquisition and use are needed before PET can be utilized to its potential.

1.3 Focus of Work

The discussion above illustrates a critical need for continued development and validation of PET tracers, methodology, and applications. More data is needed to persuade stakeholders to adopt new PET imaging approaches with demonstrated value. AD is no exception, with a commitment from the U.S. Center for Medicare and Medicaid Services to begin routine coverage of amyloid PET for AD management if provided evidence that its use improves health outcomes[50]. Inspired by these needs, this body of work aims to provide researchers with new tools and methods to validate promising interventions for neurodegenerative diseases.

Opportunities to reduce risk of failure and improve the efficiency of PET research are of high priority, given the high costs associated with conducting a PET study (infrastructure, consumables, personnel time) and the urgent need for improved imaging techniques and interventions. This dissertation describes the design, development, and implementation of custom research tools to improve efficiency for pre-clinical PET imaging. Improved throughput for pre-clinical imaging will hopefully reduce the time from bench to bedside for the testing of novel therapies, imaging agents, and imaging methods. Several de-risking and troubleshooting

workflows are outlined that can be used when developing novel neuroimaging approaches, from needs identification to pre-clinical testing. Ultimately, the goal of this work was to provide researchers with tools that are accessible, adaptable, and reduce barriers to advancements in biomedical imaging.

Chapter 2 describes the design, construction, and evaluation of custom imaging tools to enable high throughput PET/MR in rodent research models. The high demand for improved clinical imaging techniques necessitates preclinical research to validate new methods. However, preclinical scanners are not widely available, and can be complex and costly to use and maintain. Further, translation of a promising treatment, imaging agent, or imaging method to humans may require toxicology studies with a large sample size. Researchers may not have funding or qualified personnel capable of executing large studies, slowing or halting candidate therapies from reaching the clinic. A modular and accessible high-throughput imaging system was designed to reduce the time and cost limitations associated with preclinical PET imaging. We compared our custom bed to existing beds on the market and evaluated the image quality, sensitivity, and ease of use of our imaging system for longitudinal PET using the 7T Bruker BioSpin MR with PET Insert (Bruker Corporation, Billerica, Massachusetts, United States). This work is intended to outline an imaging approach that researchers can replicate to get started or get farther with the resources they have available.

Chapter 3 describes approaches to de-risk the high-throughput imaging tools described in Chapter 2 for commercialization. Commercializing a technology enables it to be widely implemented, which is a focus of this dissertation. End user needs, prospective construction materials, and technical characteristics that impact performance and safety were investigated. This chapter presents the results from testing 15 materials used in 3D printing in terms of radiodensity, optical properties, and resistance to degradation following repeated use and cleaning. Finally, a value-in-use study was conducted to demonstrate the value of our imaging tools and approach based on example use cases. It is anticipated that the information outlined in this chapter will guide researchers towards selecting the most appropriate materials for their custom, perhaps 3D-printed, research tools in addition to providing a framework to de-risk similar innovations for commercialization.

Chapter 4 describes methods to develop and troubleshoot a strategy to deliver PET imaging agents nose-to-brain (N2B) in nonhuman primates. N2B delivery has gained attention as a

treatment route for neurodegenerative disease due to its avoidance of the restrictive blood-brain barrier for vascular routes. Anatomically informed 3D-printed models of a Rhesus Macaque nasal cavity were applied to identify potential obstacles to successful delivery prior to live primate studies, improving the likelihood of success and efficiency of the research. Commercially available nebulizers for aerosol delivery were modified in response to the high costs of devices marketed specifically for nose-to-brain delivery. Aerosol delivery by the modified devices was tested in increasingly complex models, including a 3D printed two-chambered cavity, a 3D printed Rhesus Macaque nasal cavity model, and a live Rhesus Macaque. Deposition levels and patterns were assessed both qualitatively and quantitively using fluorescent- and radionuclide-labeled molecules. This chapter demonstrates the utility of 3D printed tools to pilot and optimize novel imaging applications in advance of potentially expensive experiments.

Chapter 5 describes the use of PET imaging to detect F18-FB-insulin in the brains of nonhuman primates following N2B delivery, which was critically needed to fully elucidate[51] the therapeutic potential of intranasal insulin for AD and other neurodegenerative disorders[52]. Approaches outlined in Chapter 4 were used to optimize three intranasal delivery techniques prior to application in living subjects. Clinically established tools were prioritized in the development of each delivery approach to reduce the time from bench to bedside if successful. The efficiency of each delivery method is described with regard to deposition in the subject and dose lost to dosing accessories. Further, a brain atlas was applied to quantify F18-FB-insulin localization in the primate brain following N2B transfer using the prevailing delivery method. Based on our results it is expected that our methods can be used to sensitively and quantitatively assess delivery devices, methods, drug formulations, or treatment regimens towards improved clinical outcomes for diseases of the central nervous system.

This work is intended to arm researchers and clinicians with the tools to de-risk novel neuroimaging applications. Solutions that are widely accessible to scientific professionals aim to mitigate access as a continued challenge and make the most of opportunities for use through informed preparation, troubleshooting, and efficiency.

REFERENCES

1. Thorpe, K.E., A.I. Levey, and J. Thomas, *U.S. Burden of Neurodegenerative Disease*. 2021. p. 1-13.

2. *2023 Alzheimer's disease facts and figures.* Alzheimers Dement, 2023. **19**(4): p. 1598-1695.

3. Zetterberg, H. and B.B. Bendlin, *Biomarkers for Alzheimer's disease-preparing for a new era of disease-modifying therapies.* Mol Psychiatry, 2021. **26**(1): p. 296-308.

4. Frisoni, G.B., M. Boccardi, F. Barkhof, K. Blennow, S. Cappa, K. Chiotis, J.F. Demonet, V. Garibotto, P. Giannakopoulos, A. Gietl, O. Hansson, K. Herholz, C.R. Jack, Jr., F. Nobili, A. Nordberg, H.M. Snyder, M. Ten Kate, A. Varrone, E. Albanese, S. Becker, P. Bossuyt, M.C. Carrillo, C. Cerami, B. Dubois, V. Gallo, E. Giacobini, G. Gold, S. Hurst, A. Lonneborg, K.O. Lovblad, N. Mattsson, J.L. Molinuevo, A.U. Monsch, U. Mosimann, A. Padovani, A. Picco, C. Porteri, O. Ratib, L. Saint-Aubert, C. Scerri, P. Scheltens, J.M. Schott, I. Sonni, S. Teipel, P. Vineis, P.J. Visser, Y. Yasui, and B. Winblad, *Strategic roadmap for an early diagnosis of Alzheimer's disease based on biomarkers.* Lancet Neurol, 2017. **16**(8): p. 661-676.

5. Rabinovici, G.D., C. Gatsonis, C. Apgar, K. Chaudhary, I. Gareen, L. Hanna, J. Hendrix, B.E. Hillner, C. Olson, O.H. Lesman-Segev, J. Romanoff, B.A. Siegel, R.A. Whitmer, and M.C. Carrillo, *Association of Amyloid Positron Emission Tomography With Subsequent Change in Clinical Management Among Medicare Beneficiaries With Mild Cognitive Impairment or Dementia.* JAMA, 2019. **321**(13): p. 1286-1294.

6. Sperling, R.A., P.S. Aisen, L.A. Beckett, D.A. Bennett, S. Craft, A.M. Fagan, T. Iwatsubo, C.R. Jack, Jr., J. Kaye, T.J. Montine, D.C. Park, E.M. Reiman, C.C. Rowe, E. Siemers, Y. Stern, K. Yaffe, M.C. Carrillo, B. Thies, M. Morrison-Bogorad, M.V. Wagster, and C.H. Phelps, *Toward defining the preclinical stages of Alzheimer's disease: recommendations from the National Institute on Aging-Alzheimer's Association workgroups on diagnostic guidelines for Alzheimer's disease.* Alzheimers Dement, 2011. **7**(3): p. 280-292.

7. Dubois, B., H. Hampel, H.H. Feldman, P. Scheltens, P. Aisen, S. Andrieu, H. Bakardjian, H. Benali, L. Bertram, K. Blennow, K. Broich, E. Cavedo, S. Crutch, J.F. Dartigues, C. Duyckaerts, S. Epelbaum, G.B. Frisoni, S. Gauthier, R. Genthon, A.A. Gouw, M.O. Habert, D.M. Holtzman, M. Kivipelto, S. Lista, J.L. Molinuevo, S.E. O'Bryant, G.D. Rabinovici, C. Rowe, S. Salloway, L.S. Schneider, R. Sperling, M. Teichmann, M.C. Carrillo, J. Cummings, C.R. Jack, Jr., G. Proceedings of the Meeting of the International Working, A.D. the American Alzheimer's Association on "The Preclinical State of, July, and U.S.A. Washington Dc, *Preclinical Alzheimer's disease: Definition, natural history, and diagnostic criteria.* Alzheimers Dement, 2016. **12**(3): p. 292-323.

8. Fagan, A.M., C. Xiong, M.S. Jasielec, R.J. Bateman, A.M. Goate, T.L. Benzinger, B. Ghetti, R.N. Martins, C.L. Masters, R. Mayeux, J.M. Ringman, M.N. Rossor, S. Salloway, P.R. Schofield, R.A. Sperling, D. Marcus, N.J. Cairns, V.D. Buckles, J.H. Ladenson, J.C. Morris, D.M. Holtzman, and D.I.A. Network, *Longitudinal change in CSF biomarkers in autosomal-dominant Alzheimer's disease.* Sci Transl Med, 2014. **6**(226): p. 226ra230.

9. Bateman, R.J., C. Xiong, T.L. Benzinger, A.M. Fagan, A. Goate, N.C. Fox, D.S. Marcus, N.J. Cairns, X. Xie, T.M. Blazey, D.M. Holtzman, A. Santacruz, V. Buckles, A. Oliver, K. Moulder, P.S. Aisen, B. Ghetti, W.E. Klunk, E. McDade, R.N. Martins, C.L. Masters, R. Mayeux, J.M. Ringman, M.N. Rossor, P.R. Schofield, R.A. Sperling, S. Salloway, J.C. Morris, and D.I.A. Network, *Clinical and biomarker changes in dominantly inherited Alzheimer's disease.* N Engl J Med, 2012. **367**(9): p. 795-804.

10. Habes, M., M.J. Grothe, B. Tunc, C. McMillan, D.A. Wolk, and C. Davatzikos, *Disentangling Heterogeneity in Alzheimer's Disease and Related Dementias Using Data-Driven Methods.* Biol Psychiatry, 2020. **88**(1): p. 70-82.

11. Hosny, T., E. Al-Anezi, and M.M. Khalil, *Basic Science of PET Imaging*, M.M. Khalil, Editor. 2017, Springer Nature. p. 5.

12. Saha, G.B., *Basics of PET Imaging*. Physics, Chemistry, and Regulations. 2005, New York, New York: Springer.

13. Cherry, S.R., M. Dahlbom, and M.E. Phelps, *PET: Physics, Instrumentation, and Scanners*, in *PET: Molecular Imaging and Its Biological Applications*. 2006, Springer: Springer New York, NY. p. 1-117.

14. Gsell, W., C. Molinos, C. Correcher, S. Belderbos, J. Wouters, S. Junge, M. Heidenreich, G. Vande Velde, A. Rezaei, J. Nuyts, C. Cawthorne, F. Cleeren, L. Nannan, C.M. Deroose, U. Himmelreich, and A.J. Gonzalez Martinez, *Characterization of a preclinical PET insert in a 7 Tesla MRI scanner: beyond NEMA testing.* Phys Med Biol, 2020.

15. Cherry, S.R., T. Jones, J.S. Karp, J. Qi, W.W. Moses, and R.D. Badawi, *Total-Body PET: Maximizing Sensitivity to Create New Opportunities for Clinical Research and Patient Care.* J Nucl Med, 2018. **59**(1): p. 3-12.

16. *PET-CT and PET-MRI in Neurology: SWOT Analysis Applied to Hybrid Imaging*. 2016: Springer Nature.

17. Gu, Z., D.L. Proute, R.W. Silverman, H. Herman, A. Dooraghi, and A.F. Chatziioannou, *A DOI Detector With Crystal Scatter Identification Capability for High Sensitivity and High Spatial Resolution PET Imaging.* IEEE Trans Nucl Sci., 2015. **62**(3): p. 740-747.

18. Rahmim, A., M.A. Lodge, N.A. Karakatsanis, V.Y. Panin, Y. Zhou, A. McMillan, S. Cho, H. Zaidi, M.E. Casey, and R.L. Wahl, *Dynamic whole-body PET imaging: principles, potentials and applications.* Eur J Nucl Med Mol Imaging, 2019. **46**(2): p. 501-518.

19. Morrisa, E.D., M.V. Lucas, J.R. Petrullib, and K.P. Cosgrove, *How to Design PET Experiments to Study Neurochemistry: Application to Alcoholism.* Yale Journal of Biology and Medicine, 2014. **87**: p. 33-54.

20. Hansson, O., *Biomarkers for neurodegenerative diseases.* Nat Med, 2021. **27**(6): p. 954-963.

21. Dijkers, E.C., T.H. Oude Munnink, J.G. Kosterink, A.H. Brouwers, P.L. Jager, J.R. de Jong, G.A. van Dongen, C.P. Schroder, M.N. Lub-de Hooge, and E.G. de Vries, *Biodistribution of 89Zr-trastuzumab and PET imaging of HER2-positive lesions in patients with metastatic breast cancer.* Clin Pharmacol Ther, 2010. **87**(5): p. 586-592.

22. Pfeifer, A., U. Knigge, J. Mortensen, P. Oturai, A.K. Berthelsen, A. Loft, T. Binderup, P. Rasmussen, D. Elema, T.L. Klausen, S. Holm, E. von Benzon, L. Hojgaard, and A. Kjaer, *Clinical PET of neuroendocrine tumors using 64Cu-DOTATATE: first-in-humans study.* J Nucl Med, 2012. **53**(8): p. 1207-1215.

23. Weissleder, R., *Molecular Imaging in Cancer.* Science, 2006. **213**(5777): p. 1168-1171.

24. Tempany, C.M., J. Jayender, T. Kapur, R. Bueno, A. Golby, N. Agar, and F.A. Jolesz, *Multimodal imaging for improved diagnosis and treatment of cancers.* Cancer, 2015. **121**(6): p. 817-827.

25. Wu, C., F. Li, G. Niu, and X. Chen, *PET imaging of inflammation biomarkers.* Theranostics, 2013. **3**(7): p. 448-466.

26. Oyen, W.J. and L. Mansi, *FDG-PET in infectious and inflammatory disease.* Eur J Nucl Med Mol Imaging, 2003. **30**(11): p. 1568-1570.

27. Health, C., *FDA-approved Radiopharmaceuticals*. 2023: cardinalhealth.com. p. 1-6.

28. Kulshrestha, R.K., S. Vinjamuri, A. England, J. Nightingale, and P. Hogg, *The Role of 18F-Sodium Fluoride PET/CT Bone Scans in the Diagnosis of Metastatic Bone Disease from Breast and Prostate Cancer.* J Nucl Med Technol, 2016. **44**(4): p. 217-222.

29. Czernin, J., N. Satyamurthy, and C. Schiepers, *Molecular mechanisms of bone 18F-NaF deposition.* J Nucl Med, 2010. **51**(12): p. 1826-1829.

30. Jadvar, H., B. Desai, and P.S. Conti, *Sodium 18F-fluoride PET/CT of bone, joint, and other disorders.* Semin Nucl Med, 2015. **45**(1): p. 58-65.

31. Wong, K.K. and M. Piert, *Dynamic bone imaging with 99mTc-labeled diphosphonates and 18F-NaF: mechanisms and applications.* J Nucl Med, 2013. **54**(4): p. 590-599.

32. Maaniitty, T., J. Knuuti, and A. Saraste, *15O-Water PET MPI: Current Status and Future Perspectives.* Semin Nucl Med, 2020. **50**(3): p. 238-247.

33. Shaffer, J.L., J.R. Petrella, F.C. Sheldon, K.R. Choudhury, V.D. Calhoun, R.E. Coleman, and P.M. Doraiswamy, *Predicting Cognitive Decline in Subjects at Risk for Alzheimer Disease by Using Combined Cerebrospinal Fluid, MR Imaging, and PET Biomarkers.* Radiology, 2013. **226**: p. 583-591.

34. Lagarde, J., P. Olivieri, M. Tonietto, P. Gervais, C. Comtat, F. Caille, M. Bottlaender, and M. Sarazin, *Distinct amyloid and tau PET signatures are associated with diverging clinical and imaging trajectories in patients with amnestic syndrome of the hippocampal type.* Transl Psychiatry, 2021. **11**(1): p. 498.

35. Andrade, R.S., D.E. Heron, B. Degirmenci, P.A. Filho, B.F. Branstetter, R.R. Seethala, R.L. Ferris, and N. Avril, *Posttreatment assessment of response using FDG-PET/CT for patients treated with definitive radiation therapy for head and neck cancers.* Int J Radiat Oncol Biol Phys, 2006. **65**(5): p. 1315-1322.

36. Branstetter, B.F., T.M. Blodgett, L.A. Zimmer, C.H. Snyderman, J.T. Johnson, S. Raman, and C.C. Meltzer, *Head and Neck Malignancy: Is PET/CT More Accurate than PET or CT Alone?* Radiology, 2005. **235**: p. 580-586.

37. Schwarz, C.G., *Uses of Human MR and PET Imaging in Research of Neurodegenerative Brain Diseases.* Neurotherapeutics, 2021. **18**(2): p. 661-672.

38. Bucci, M., K. Chiotis, A. Nordberg, and I. Alzheimer's Disease Neuroimaging, *Alzheimer's disease profiled by fluid and imaging markers: tau PET best predicts cognitive decline.* Mol Psychiatry, 2021. **26**(10): p. 5888-5898.

39. Noh, Y., S. Jeon, J.M. Lee, S.W. Seo, G.H. Kim, H. Cho, B.S. Ye, C.W. Yoon, H.J. Kim, J. Chin, K.H. Park, K.M. Heilman, and D.L. Duk L. Na, *Anatomical heterogeneity of Alzheimer disease.* Neurology, 2014. **83**: p. 1936-1944.

40. Levin, F., D. Ferreira, C. Lange, M. Dyrba, E. Westman, R. Buchert, S.J. Teipel, M.J. Grothe, and I. Alzheimer's Disease Neuroimaging, *Data-driven FDG-PET subtypes of Alzheimer's disease-related neurodegeneration.* Alzheimers Res Ther, 2021. **13**(1): p. 49.

41. Joshi, B., *Medical Imaging Instrumentation: Global Markets and Technologies Through 2022*.

42. Keppler, J.S., *A Cost Analysis of Positron Emission Tomography.* Am. J. Roentgenol., 2000. **177**: p. 1771-1731.

43. Yao, R., R. Lecomte, and E.S. Crawford, *Small-animal PET: what is it, and why do we need it?* J Nucl Med Technol, 2012. **40**(3): p. 157-165.

44. Pan, S., P.H. Yang, D. DeFreitas, S. Ramagiri, P.O. Bayguinov, C.D. Hacker, A.Z. Snyder, J. Wilborn, H. Huang, G.M. Koller, D.K. Raval, G.L. Halupnik, S. Sviben, S. Achilefu, R. Tang, G. Haller, J.D. Quirk, J.A.J. Fitzpatrick, P. Esakky, and J.M. Strahle, *Gold nanoparticle-enhanced X-ray microtomography of the rodent reveals region-specific cerebrospinal fluid circulation in the brain.* Nat Commun, 2023. **14**(1): p. 453.

45. Gajuryal, S.H., A. Daga, V. Siddharth, C.S. Bal, and S. Satpathy, *Unit Cost Analysis of PET-CT at an Apex Public Sector Health Care Institute in India.* Indian J Nucl Med, 2017. **32**(1): p. 1-6.

46. Fendler, W.P., J. Czernin, K. Herrmann, and T. Beyer, *Variations in PET/MRI Operations: Results from an International Survey Among 39 Active Sites.* J Nucl Med, 2016. **57**(12): p. 2016-2021.

47. Zhou, I.Y., C.T. Farrar, J. Mandeville, M.S. Placzek, N.J. Rotile, C. Molinos Solsona, T. Sasser, S.A. Esfahani, M. Heidenreich, and P. Caravan, *Multi-Animal Simultaneous PET/MR Imaging*. Bruker BioSpin.

48. Kersemans, V., S. Gilchrist, P.D. Allen, S. Wallington, P. Kinchesh, J. Prentice, M. Tweedie, J.H. Warner, and S.C. Smart, *A System-Agnostic, Adaptable and Extensible Animal Support Cradle System for Cardio-Respiratory-Synchronised, and Other, Multi-Modal Imaging of Small Animals.* Tomography, 2021. **7**: p. 39-54.

49. Kim, H., G.H. Im, Y. Yoon, H.S. Kim, C.H. Yoo, and B.Y. Choe, *Development of a new advanced animal cradle for small animal multiple imaging modalities: acquisition and evaluation of high-throughput multiple-mouse imaging.* Phys Eng Sci Med, 2021. **44**(4): p. 1367-1376.

50. Rabinowicz, A.L., E. Carrazana, and E.T. Maggio, *Improvement of Intranasal Drug Delivery with Intravail((R)) Alkylsaccharide Excipient as a Mucosal Absorption Enhancer Aiding in the Treatment of Conditions of the Central Nervous System.* Drugs R D, 2021. **21**(4): p. 361-369.

51. Craft, S., R. Raman, T.W. Chow, M.S. Rafii, C.K. Sun, R.A. Rissman, M.C. Donohue, J.B. Brewer, C. Jenkins, K. Harless, D. Gessert, and P.S. Aisen, *Safety, Efficacy, and Feasibility of Intranasal Insulin for the Treatment of Mild Cognitive Impairment and Alzheimer Disease Dementia: A Randomized Clinical Trial.* JAMA Neurol, 2020. **77**(9): p. 1099-1109.

52. Freiherr, J., M. Hallschmid, W.H. Frey, 2nd, Y.F. Brunner, C.D. Chapman, C. Holscher, S. Craft, F.G. De Felice, and C. Benedict, *Intranasal insulin as a treatment for Alzheimer's disease: a review of basic research and clinical evidence.* CNS Drugs, 2013. **27**(7): p. 505-514.

CHAPTER 2: HIGH THROUGHPUT IMAGING TOOLS FOR PRE-CLINICAL NEUROIMAGING

2.1 Background

Biomedical imaging is critical for detecting, monitoring, and investigating diseases in living subjects. These techniques are used clinically to provide information about anatomy and/or physiology at the molecular, cellular, or organ level depending on the technique used. For example, computed tomography (CT) is routinely used for bone fractures[41], magnetic resonance imaging (MRI) for neurodegenerative diseases[53], and positron emission tomography (PET) for cancers[41]. Increasingly often, imaging techniques are combined to supplement single-modality limitations, enable image corrections that improve data quality, or increase diagnostic value[35,36,54-56]. Improved diagnostic and treatment methods are in high demand given the growing elderly population and associated incidence rates of injury and chronic diseases, prompting investments in imaging methods and instrumentation[41,57-60].

Despite growing interest in multi-modal imaging methods, access to such scanners is limited partly due to high purchasing and maintenance costs. MRI, CT, and nuclear imaging instruments (single or multi-modality) are among the most expensive in the imaging market with low to no expectation to change according to market reports[57,59,61]. For example, costs to establish and operate a PET imaging center are estimated to start at $3.5 million[15,42,45] and $1 million[42] depending on equipment quality. Traditionally, a single subject is imaged per scan, which may require significant time to prepare and execute. These practices contribute to low imaging throughput, which has been identified as the main limitation to cost-effective PET imaging[42]. Both the high costs and low throughput of PET/MRI are current barriers to the acceleration of hybrid PET/MRI system use[41]. Demands on time and funding limit where, what, and how often this critical PET research can be conducted.

There is a need to improve throughput for multi-modal PET, CT, and MR imaging. Thus, we have developed a 2-pronged high-throughput accessory system that enables multi-subject PET/MRI in mice and rats. This system addresses the need for improved efficiency by augmenting existing scanning beds to accept custom bed units made for rapid exchange of subjects between imaging timepoints, providing a convenient way to gather data from a large cohort of animals. We assessed the performance of the accessory system and demonstrated use cases that highlight each prong of the high throughput approach. Image quality and signal recovery were compared

for the custom bed unit and manufacturer scanning bed for the 7T Bruker BioSpin 70/30 MRI with PET insert.

2.2 Materials and Methods

2.2.1 Bed Design and Production

2.2.1.1 Design Criteria for High Throughput Imaging System Components

Constraints and desirable features were determined for the custom bed prior to design. Regarding constraints, the custom bed had to fit within the PET insert (11.2 cm internal diameter) and maintain appropriate anesthetic depth and warmth for more than one rodent at a time. Construction materials must be MR-safe and low-density to maintain appropriate sensitivity for PET imaging. The ability to monitor subjects during scanning, ease of access to subjects (in case of adverse event), and compatibility with existing instrument beds were identified as desirable features. Additionally, it would be desirable to use materials that could be replaced quickly and cost-effectively.

2.2.1.2 Design of High Throughput Imaging System Components

The system involves three main components – (1) the custom bed and accessories, (2) the MRI extension and end cap, and (3) the staging area (Figure 1).

2.2.1.2.1 Custom Bed Unit

A custom bed unit built from polyvinyl chloride (PVC) pipes and 3D printed parts was designed to facilitate efficient exchange of animal sets for neuroimaging. The PVC was cut to 40 cm longitudinally to act as a 2-rodent cradle that could be easily exchanged into and out of the scanner. A platform was designed to rest inside of the PVC and secure two removable nose cones via placement in a deep recess (6 mm). Nose cones were designed with a wide mouth to stabilize the subject’s head in the absence of ear bars, which are otherwise used to f. The scanner's anesthesia supply line was split to direct anesthetic to two subjects via tubing that enters at the back of the nose cone. The bite bar design was generously shared by the Plazcek Lab (Athinoula A. Martinos Center for Biomedical Imaging, The Institute for Innovation in Imaging, Massachusetts

General Hospital and Harvard Medical School)[47]. The PVC insert, nose cones, and bite bars were designed in Autodesk Fusion 360 and printed from VeroClear resin on a J750 PolyJet 3D printer (Stratasys). Nylon thumb screws were used to tighten the bite bar in place.

2.2.1.2.2 MRI Extension and End Cap

To accommodate simultaneous imaging of 2 rats, a 3D printed extension (12.7 cm) to lengthen the Bruker BioSpin 70/30 rat bed was designed in Autodesk Fusion 360. To do this, a μCT scan (Perkin Elmer QuantumX μCT) of the manufacturer rat bed was acquired at the midsection (90 kV exposure peak, 2 min exposure time, 88 mA X-ray tube current, 512 x 512 x 268 image size, 0.144 mm^3 voxels). The resulting DICOM was converted to an STL file using -30 Hounsfield Units (HU) as the segmentation threshold in Embodi 3D (www.embodi3d.com). The resulting STL was re-meshed and refined before elongating one face to 120 mm total length. An end cap was designed to connect the bed extension to the existing manufacturer rat bed using their shared geometry. The internal compartment in the manufacturer's bed that houses circulating warm water to support subject body temperature was maintained in the extension piece so that subjects would be equally warmed during scanning. Stop-flow connectors directed water from the manufacturer bed, through the MRI extension, and back to the heating pump that supplies the scanner. The extension and end cap were printed from VeroClear resin on a J750 PolyJet 3D printer.

2.2.1.2.3 Staging Area

A staging area was designed to organize and maintain subjects between imaging timepoints. The unit was composed of the 8 3"-diameter PVC pipes cut in half longitudinally and assigned as staging lanes or lane supports. After 6 divots were cut along the longitudinal midline, lane supports (n=2) were placed on their lengthwise cuts, parallel, with 1.5' separation. The staging lanes (n=6) rest in the divots, rounded side down, between the support lanes. The transferrable bed unit can be placed into a staging lane, attached to anesthesia, and removed for further imaging with minimal barriers.

2.2.2 Characterization of Image Sensitivity Using Custom Bed

2.2.2.1 Construction Material Radiodensity Assessed by μCT Imaging

A μCT image of the custom bed unit was acquired on the Perkin Elmer QuantumX μCT scanner to determine the radiodensity of each material used (90 kV exposure peak, 24 sec exposure time, 88 mA X-ray tube current, 256 x 256 x 399 image size, 0.288 mm^3 voxels). Radiodensity was quantified by averaging 3 mm diameter spheres (n=3) per component and normalizing to water in PMOD 4.2 (PMOD Technologies LLC).

2.2.2.2 PET Imaging to Characterize *Sensitivity*

A 7T Bruker BioSpec 70/30 MRI with PET insert was used to evaluate the impact of our custom bed on PET image quality. Brain-sized and sub-resolution phantoms were filled with [F-18]-2-deoxy-fluoroglucose (F-18-FDG, Cardinal Health, East Lansing, MI) and imaged via PET to quantify recovery and spatial resolution. Rodents were injected with F-18-FDG intravenously and intraperitoneally and followed with dynamic and longitudinal PET/MR imaging, respectively.

2.2.2.3 Saline Vial Phantoms

F-18-FDG-filled saline vials (2738 or 11,285 kBq/74 or 305 μCi) were positioned opposite an untreated saline vial in a custom bed to mimic the brain geometry of a treated and untreated rat pair. The vials were imaged simultaneously by MR (T2 TurboRARE T_E 53.9 ms, T_R 2000 ms, scan time 4 min 24 s, echo spacing 6.741ms, rare factor 16, FOV 60 x 32 x 32 mm via 32 1 mm-thick slices, flip angle 180) and PET (scan time 5 min, FOV 90 x 90 x 150 mm). The PET scan was reconstructed with 0.25 mm^3 voxel size via MLEM algorithm (18 iterations) with scatter, randoms, and decay correction. Iso-contouring was used to generate a saline vial volume of interest (VOI) based on the MR image in PMOD 4.2 (PMOD Technologies, LLC). Detection efficiency was calculated as ((detected signal/true signal)*100), while spillover to the naïve vial was calculated as ((detected signal in naïve vial/true signal in hot vial)*100). True signal was determined by dose calibrator (Capintec, Inc.).

2.2.2.4 Vessel Experiments with PE Tubing

Polyethylene tubing with internal diameters 0.28 – 0.76 mm (PE sizes 10-60, Braintree Scientific) were used to test the impact of the custom bed unit on detection efficiency and spatial resolution for sub-resolution structures. PE tubing was filled with F-18-FDG and sealed with hematocrit putty (Fisher Scientific) on each end prior to activity measurement by dose calibrator. The 5 cm tubes were positioned with 1 cm separation transaxially and imaged on our custom imaging bed, then the manufacturer's rat bed (scan start times within same 10 minutes). PET images (scan time 5 min, FOV 90x90x150 mm) were reconstructed with 0.25 mm^3 voxel size via MLEM algorithm (18 iterations) with scatter, randoms, and decay correction.

Recovery coefficients (RC) were calculated according to NEMA standards[62]. Iso-contouring was used to generate VOIs that contained the hottest 5% of voxels within a restricted volume for each PE tube. RC was calculated as (measured phantom activity – measured background activity)/(known phantom activity – known background activity). Background VOI were not intersecting nor adjacent to any radionuclide-filled tube. Full-width half maximum (FWHM) and full width tenth maximum (FWTM) values were calculated to assess spatial resolution in the custom bed to 2 significant digits. VOI size, activity level relative to background, and distance from the center of the PET detectors (termed radial offset) are known to influence image quality and quantification. Relationships between recovery coefficient, spatial resolution, and the metrics mentioned were characterized via linear regression in GraphPad PRISM.

2.2.3 Characterization of Bed Safety and Efficacy for Subject Use

2.2.3.1 Use of Staging Area

Performance of anesthesia delivery and warm water circulation at the staging area were evaluated. The staging area was assembled on a plastic cart equipped with a water circulation pump, water blanket (HTP-1500, Kent Scientific), and direct anesthesia lines from the vaporizer. The 7T BioSpec 70/30 has a shielded magnet, so the cart could be placed in the corner of the MRI room beneath the operator window for a short transfer distance between the MRI and staging area.

Sprague Dawley rats (n=3, F) were anesthetized with isoflurane (3% for induction) and loaded one per custom bed unit. Subjects were maintained in the staging area for 2 hours, covered by a towel and water circulation blanket to maintain body temperature. A veterinary pulse oximeter (2500A, NONIN) and noninvasive temperature probe (Kent Scientific) were used to measure heart rate, blood oxygen saturation, and skin temperature every ten minutes for each subject. All procedures involving animals were reviewed and approved by the Michigan State University Institutional Animal Care and Use Committee (IACUC protocol number: 201800197).

2.2.3.2 Use of MRI Extension

Performance of the heating component of the scanning bed extension was compared to the manufacturer bed. Surface measurements were taken from the surface of the manufacturer MRI bed and the MRI extension piece using the noninvasive thermometer. Both components are supplied from the same water circulation bath (SAHARA PPO S5P Heated Bath Circulator, Thermo Scientific), which was set to 50°C.

2.2.3.3 Use of Custom Bed Unit for Dynamic Imaging

The custom bed unit was evaluated for 2-rat neuroimaging by dynamic PET/MR following an intravenous injection of F-18-FDG. Following simultaneous induction of anesthesia by isoflurane (2-3%), fasted Sprague Dawley rats (12-hour fast, n=2) were loaded into the custom bed units and placed on the MR scanning bed. F-18-FDG (272 μCi, 10 MBq) was injected as a bolus via tail-vein catheter following the start of a 60-minute dynamic PET acquisition (2 min delay, 10s bins 2 min-5 min, 5 min bins 5-60 min, FOV 90 x 90 x 150 mm). A high-resolution T2 TurboRARE (T_E 60.67 ms, T_R 2000 ms, scan time 15 min 38 s, echo spacing 6.741, rare factor 16, FOV 80 x 60 x 32 mm via 32 1 mm-thick slices, excitation angle 90, refocusing angle 180, flip back and fat suppression enabled, 0.5 mm^3 cubed voxel size) was acquired during the PET scan using an 86 mm-diameter RF coil (Bruker). A rectal thermometer and respiration pad were used to monitor body temperature and breathing rate in one subject per set during scanning. An attenuation map was generated based on the T2 TurboRARE and used to attenuation-correct the PET image during reconstruction, in addition to randoms, dead time, and decay correction by the MLEM algorithm (18 iterations, 0.5 mm^3 voxel size). The reconstructed PET scan was geometrically co-registered to the MR image in ParaVision V3.2. No manual adjustments were made to the registration during image analysis or figure generation, which were both done in PMOD 4.2. Brain

VOIs were outlined manually, while heart VOIs were generated by iso-contouring within a bounded box centered on the tissue of interest.

2.2.3.4 Use of High Throughput Imaging System for Longitudinal Scanning

Efficacy of the high-throughput imaging system was tested in both mice and rats by following intraperitoneal (IP) injections of F-18-FDG for static longitudinal imaging. Fasted BALB/c mice (14-hour fast, n=2 females) were simultaneously induced by isoflurane anesthesia and loaded into the custom bed units without bite bars following IP injection or F-18-FDG (175 μCi, 6.48 MBq). Subjects were imaged by PET/MR from 15-20, 40-45-, and 65-70-minutes post-dose. The PET (scan time 5 min, FOV 90 x 90 x 150 mm) and MR (T2 TurboRARE with T_E 53.93 ms, T_R 2000 ms, scan time 6 min 8 s, echo spacing 6.741 ms, rare factor 16, FOV 60 x 50 x 32 mm, image size 80 x 66 x 43, excitation angle 90, refocusing angle 180, flip back and fat suppression enabled, nearly isotropic at 0.75 mm^3 voxel size) scans were acquired simultaneously with the 86 mm-diameter RF coil and PET insert (Bruker). The same subject monitoring, image reconstruction, and analysis procedures described for dynamic imaging were used. Translations were made to favor brain viewing for figure generation.

Similarly, fasted F344 rats (4-hour fast pre-dose, n=2 females) were simultaneously induced with isoflurane anesthesia and loaded into the custom bed units with bite bars following intraperitoneal injection of F-18-FDG (275 μCi, 10.18 MBq). Rats followed the same imaging protocol as the mice, but at 20-30, 55-60-, and 80-minutes post-dose. The same reconstruction and image analysis methods were used.

2.3 Results

2.3.1 Design of High Throughput Imaging System

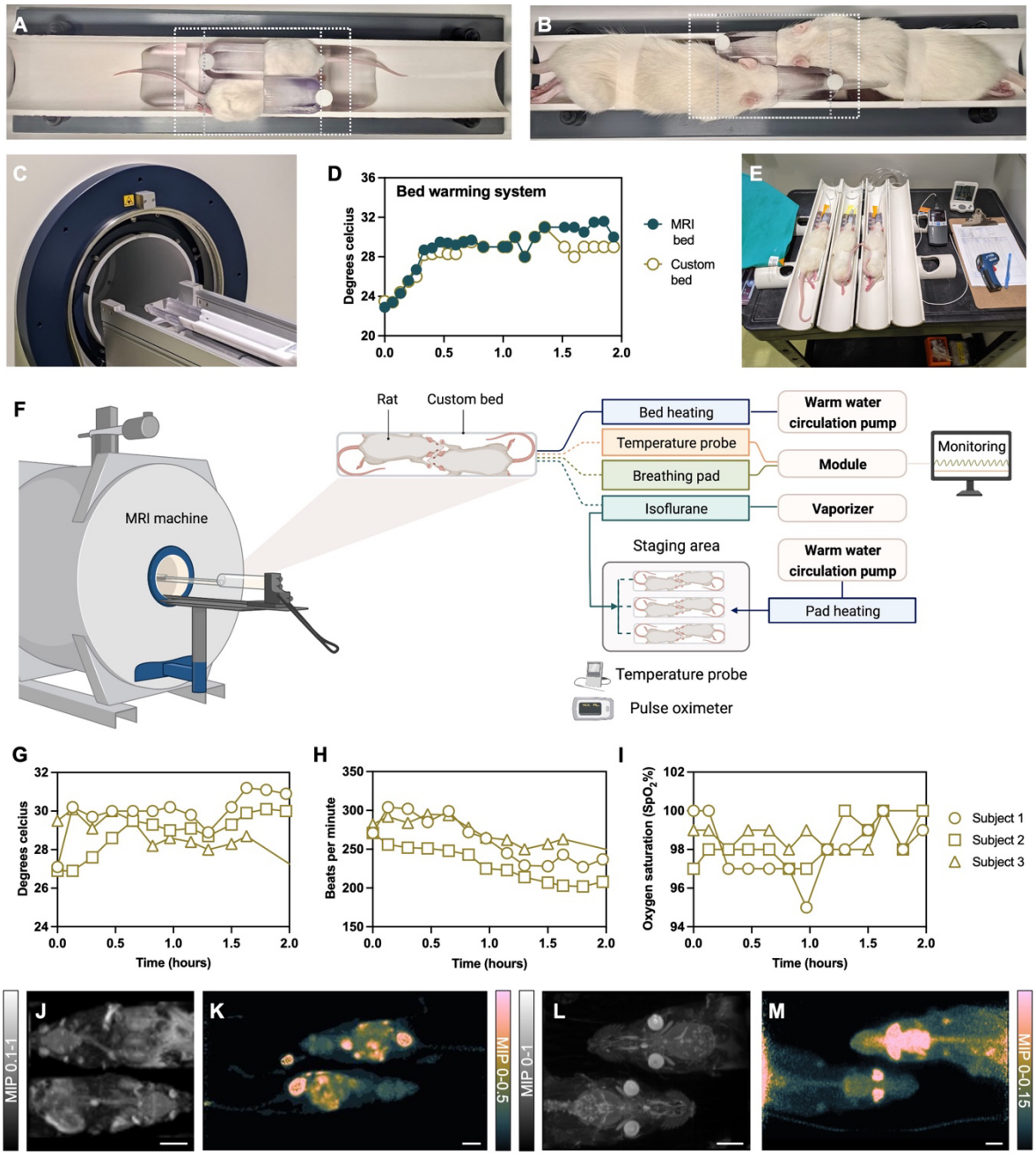

Figure 2.1. Overview of high-throughput imaging system components and performance. A,B. Custom bed unit loaded with mice (A) and rats (B). C. 7T Bruker BioSpec 70/30 MRI outfitted with rat scanning bed and 3D-printed extension (clear). D. Extension heating system performs analogously to manufacturer bed. E. Staging area with rats loaded into custom bed units individually. F. Experiment set-up using high-throughput imaging system. G-I. Rat skin temperature (G), heart rate (H), and oxygen saturation (I) while resting in staging area for two hours. Symbols indicate measurements from individual subjects. J-M. Maximum intensity projections displaying the limits of the field of view when mice are imaged by MRI (J) or PET (K), compared to rats imaged by MRI (L) or PET (M). Scale bar = 1 cm.

The system enabled multi-rodent PET/MR neuroimaging in mice and rats using low-cost construction materials and techniques. The high-throughput imaging system consisted of a custom bed unit (Figure 2.1A,B), MRI bed extension (Figure 2.1C), and staging area (Figure 2.1E) that worked in combination (Figure 2.1F).

The custom bed unit situated the brains of 2 mice or rats in the Bruker BioSpec 70/30 FOV to allow simultaneous neuroimaging by PET and MR. Two mice were imaged full-bodied in both PET (Figure 2.1A, white dotted line) and MR (gray dotted line), while two rat heads were visible by MR and head-heart by PET (Figure 2.1J-M). The low barrier to nose cone replacement and removal supported ease and flexibility when loading rodents. The depth of the platform cut-out securely maintained the position of the nose cones without additional hardware. The anti-parallel orientation of the nose cones positioned both rodent brains in the MR sensitive region for imaging. Finally, unneeded material removed from the back of the nose cone and slope of the platform component reduced restrictions to the subjects' shoulders and rib cage, reducing risk of breathing complications while under anesthesia.

The only instrument modification needed to use our high-throughput system was replacement of the manufacturer's scanning bed nose cone with the extension piece, which increased bed capacity in the Z direction. Warm water directed to the MR scanning bed was split using plastic stop-flow connectors and passed through the hollow interior of the 3D printed accessory, providing heating analogous to that built into the manufacturer's imaging bed in design and function. Installation and removal of the extension and water lines was completed quickly and without mess, as no leaks were observed in the system. When switching between subject sets, replacing the anesthesia line for the custom bed unit to be imaged next was the only required change. At the staging area, a valve was opened after the custom bed unit tubing was connected to provide anesthesia, and closed when the unit was removed for imaging or recovery.

Access to subjects was not restricted in our custom bed unit, so various styles of MR-safe monitoring equipment can be readily employed for at least one subject during imaging. These tools work in tandem with monitoring equipment at the staging area to support the maintenance of subject health throughout experiments of varied length. We found this approach to be sufficient to maintain the health of independently-staged subjects for two continuous hours (Figure 2.1G-H).

2.3.2 Characterization of Image Sensitivity Using Custom Bed

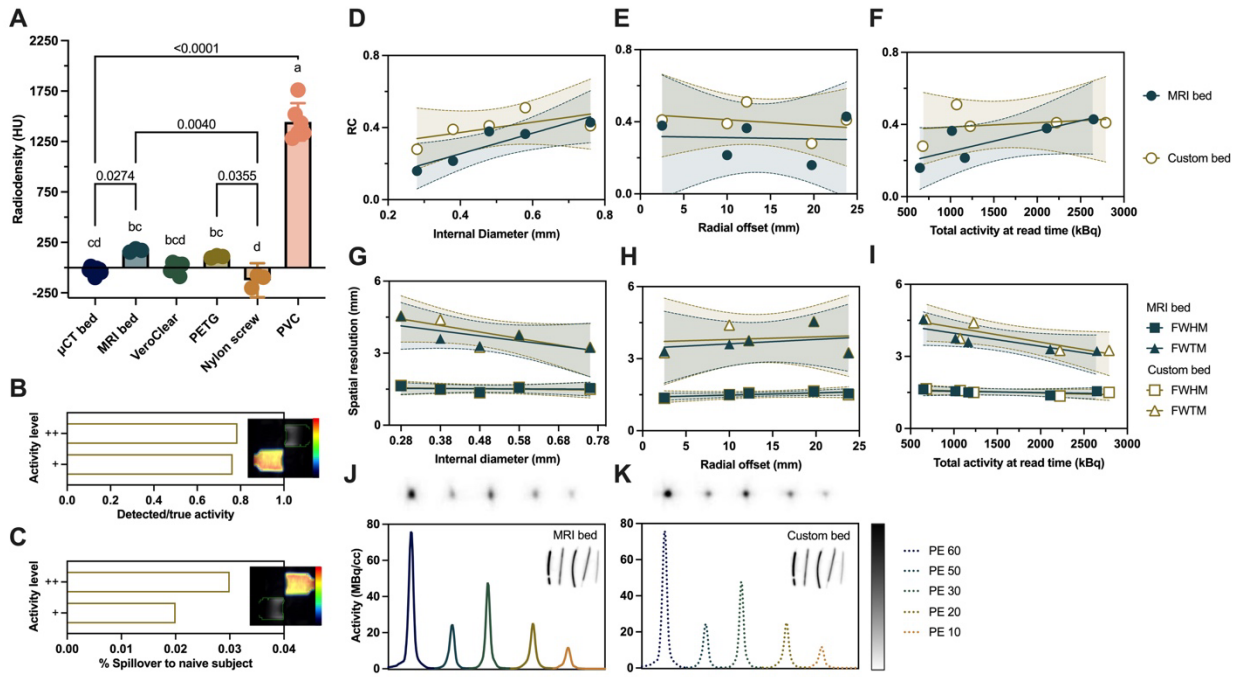

Figure 2.2. Impact of signal attenuation on image quality and detection for manufacturer and custom beds. A. Radiodensity of construction materials compared to μCT and MRI scanning beds. B,C. Brain-sized phantom recovery is 77% on average (B), with 0.025% spillover (C) for medium (+) and high (++) activity vials. Rainbow color bar range is 0-5000 kBq/cc. D-F. Recovery coefficients for sub-resolution tubing under both imaging conditions. G-I. Spatial resolution given for sub-resolution tubing under both imaging conditions. J,K. Line-profiles for sub-resolution tubing filled with F-18-FDG at trans-axial cross sections (images given above graph) when imaged on the manufacturer MRI bed (J) or the custom bed unit (K). Shaded bands on graphs D-G give 95% confidence intervals.

2.3.2.1 Construction Material Radiodensity Assessed by μCT Imaging

On average, radiodensity of our construction materials were very similar to the imaging beds provided by small-instrument μCT and MR manufacturers, with the exception of PVC. PVC had a water-corrected signal intensity of 1295 HU ± 33 SEM, placing it in the same density range as bone[63]. PETG is a low-cost, commercially available filament and was found to be comparable to VeroClear and the MRI manufacturer bed (Figure 2.2A), offering a cheaper alternative to 3D printed resins.

2.3.2.2 Detection Efficiency

Detection efficiency for the custom bed unit was comparable to the manufacturer bed for brain-sized phantoms (15 cm^3), achieving 77% signal detection with negligible spillover (< 0.03%) between them (Figure 2.2B-C). Recovery coefficients for sub-resolution structures were similar or higher using the custom bed unit compared to the manufacturer's scanning bed. As expected, samples larger in size or activity relative to background had higher signal recovery. Recovery coefficients were closest between imaging beds for sub-resolution phantoms with activity > 1850 kBq (50 μCi, Figure 2.2K). Error was similar in both conditions.

2.3.2.3 Image Quality

Signal intensity (kBq/cc) was greater in the custom bed unit at the trans-axial cross sections of the polyethylene tubes (Figure 2.2B-C), visible quantitatively in the sharper, darker tube cross sections and quantitatively in the line profile peak values (Figure 2.2J-K). Spatial resolution for sub-resolution structures was nearly identical between the custom bed unit and the manufacturer bed, with the best resolution achieved at the center of the FOV (Figure 2.2G-H). An inverse relationship was observed between spatial resolution and tube diameter, and spatial resolution and total activity for FWTM. Given that the PE tubes are all below manufacturer-reported resolution and were filled from a radionuclide stock, the observed effect is likely due to lower activity relative to background in smaller tube sizes.

2.3.3 Characterization of Bed Safety and Efficacy for Subject Use

2.3.3.1 Use of Custom Bed Unit for Dynamic Imaging

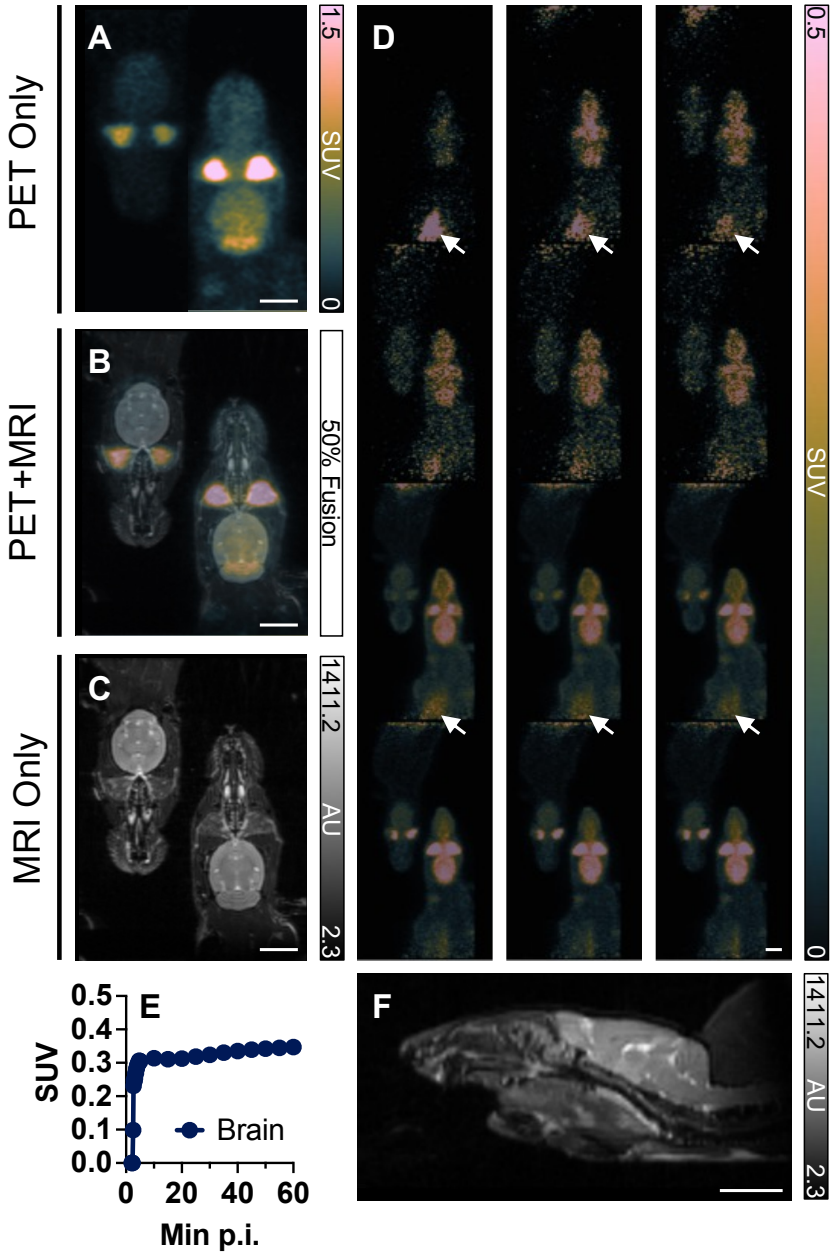

Figure 2.3. Two-rat dynamic imaging results following an intravenous injection of F-18-FDG. A-C. Axial PET, MR, and co-registered PET+MR images of rat brains 60-minutes-post injection. D. Average brain time-activity curve for both rats. E. Time series of PET images showing accumulation of F-18-FDG heart (arrows) and brain. SUV data is loaded for the leftmost subject (SUV data must be loaded separately). The time bins shown are as follows: 0-0:30 in 10 second bins in top row; 3:50-4:10 in 10 second bins sec in 2nd row; 10, 15, 20 minutes post-injection in 3rd row; 50, 55, 60 minutes in 4th row. F. Sagittal slice of rightmost subject head showing structures of interest with high resolution. Scale bar = 1 cm.

The low throughput typically associated with dynamic PET imaging, due to longer scan durations, was improved by use of our custom 2-rodent bed unit. The MR FOV for both subjects (Figure 2.3C) included the head to the cervical spinal cord (C1-2)[64]. In the PET FOV, radiotracer was visible from head to heart in both animals, enabling multi-rat cardiac imaging by PET (Figure 2.3E). F-18-FDG brain uptake was lower than expected, which may indicate a poor IV injection (Figure 2.3D). In this configuration, both subjects are visible in the FOV in the axial and coronal viewing planes only. Additionally, the imaging duration needed for dynamic PET scans provided ample time for high-resolution MR scans of the brain. Structures such as the third, fourth, and lateral ventricles, hippocampus, corpus callosum, and arbor vitae of the cerebellum were resolvable by eye (Figure 2.3C, F).

2.3.3.2 Use of High Throughput Imaging System for Longitudinal Scanning

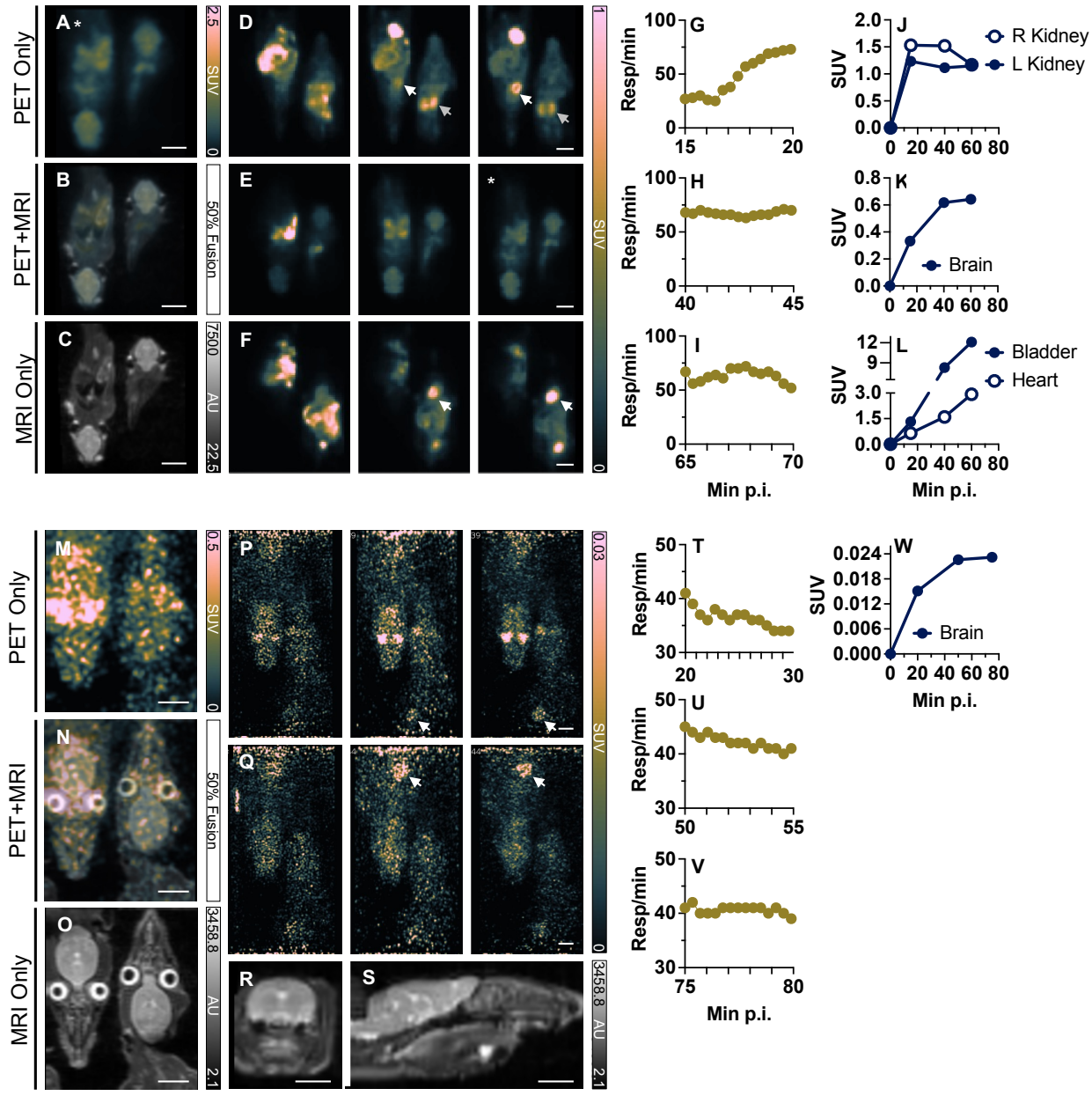

Figure 2.1. Two-rodent longitudinal imaging results following an intraperitoneal injection of F-18-FDG. A-C. Axial PET, MR, and co-registered PET+MR images of mouse brains 70-minutes-post injection. D-F. Heart (white arrows in D,F), kidneys (gray arrow in D), and brain (E), shown for mice at 20 (left), 45 (middle), and 70 minutes (right) post-injection. The white asterisk in A and E (right) indicates that the same images are shown. G-I. Mouse respiration rates during scanning. J-L. Time-activity curves for the organs highlighted in panels D-F. M-O. Axial PET, MR, and co-registered PET+MR images of rat brains 80-minutes post-injection. P-Q. Hearts (white arrows) and brains shown for rats 30 (left), 55 (middle), and 80 minutes (right) post-injection. R-S. Coronal and sagittal slices of rightmost subject's head showing structures of interest visible in the short acquisition duration MR images. T-V. Rat respiration rates during scanning. W. Averaged time-activity curves for the brains of these subjects. All scale bars = 1 cm.

Rapid exchange of the 2-rodent holders enabled PET/MR neuroimaging of 4 rodents to be completed within 80 minutes. In mice, the MR sensitive region nearly encapsulated an entire mouse body, enabling image-based biodistribution and whole-body clearance studies of PET and MR contrast agents. The kidneys (Figure 2.4B), brain (Figure 2.4C), and heart (Figure 2.4D) were easily identifiable in the PET images and showed F-18-FDG accumulation in the pattern expected from the literature[65]. The bladder, brain, and myocardium continued to accumulate tracer over time, while the kidney time-to-peak occurred earlier, followed by a reduction in signal after 60 minutes. Accumulation of F-18-FDG in rat brains followed the expected pattern, although uptake was lower than anticipated likely due to a shorter fasting time. Both species maintained an appropriate respiration rate throughout the imaging experiment.

Even with image acquisition times of 5 minutes or less, we acquired T2-weighted images with sufficient resolution for anatomical reference and attenuation correction in both species. Brain structures such as ventricles and white matter tracts are readily resolved in rats (Figure 2.4G-H). Although image translations were not required for image analyses, they may be desired when showing images if the animals are rotated around the Z axis.

2.4 Discussion

Our high-throughput imaging approach offers improvements over existing methods. The low-barrier-removal nose cones made subject set-up easier than in a scanning bed with a fixed nose cone and made it possible to quickly access subjects in the event of complication. To our knowledge, no other scanning bed has accommodated both mice and rats in a single design. Our system maintained use of the bed that was native to the imaging instrument (e.g. Bruker BioSpec), which allowed the continued use of all bed features, including automatic positioning. Our custom bed unit was not instrument specific. It was designed to be quickly swapped into an instrument for a scan, then swapped out for another set of subjects or to a different instrument for combined modality or comparison studies. Specific scanner hardware was not required for use of our accessory system. Thus, our design will be compatible with other scanners. An extension may be made as outlined here for instruments that are compatible aside from scanning bed length.

Our design was constructed and expanded using low-cost construction materials and methods. This modular design utilized a limited number of interchangeable components to facilitate easy part replacement or expansion of the system. The system was easy to build, utilize for imaging,

and subsequently break down for compact storage. Complete disassembly provided an opportunity to effectively clean and disinfect components to maintain the health of animal colonies and imaging spaces. Finally, PVC and 3D printed components were MR-safe, easily modified, and cost-effective. This system can be set-up directly inside of the MRI space, and/or made mobile by storing on a cart equipped with anesthesia and water circulation accessories (Figure 2.1), enabling transport to scanning or procedure rooms. Modifications to 3D printed or PVC components, such as in length, diameter, material, etc., can be rapidly implemented. 3D printers are becoming ubiquitous at major research institutions, as the printers and the materials they require are becoming increasingly affordable. Future iterations may consider replacing the PVC component of the custom bed unit with a less dense material to improve imaging sensitivity.

Our tool could increase the value of the scanning instrument by helping researchers get more use out of it, in expanded applications or reduced scan time. Pre-clinical imaging experiments can become costly quickly, especially when higher sample sizes are needed. Our system used a 2-prong approach to increase throughput. Image quality and sensitivity were comparable to results acquired using the manufacturer bed Imaging time was reduced by half or more due to simultaneous acquisition in 2 subjects (rats or mice), which reduces total scan time, costs, and experimental error for experiments. The design of the custom bed unit allows for rapid exchange of animals, thus higher throughput of imaging (more animals per day). Additionally, swapping pre-staged subjects reduced time delays between scans due to subject set-up. We expect these tools to be of greatest use for dynamic studies eligible for replacement by a longitudinal few-timepoint design. The greater the gap duration between timepoints, the more animal sets that can be imaged, the greater the reduction of overall instrument use costs.

Our product was specifically designed for small animal PET/MRI neuroimaging but could be applied to other applications. This approach could be used to maintain a cohort of animals for monitoring experiments, sample collection, or pre-clinical imaging in other modalities. Exposure to environmental factors, agricultural agents, or prospective therapeutics (toxicity, target binding, and/or pharmacokinetics) can be efficiently assessed by our approach. Generally, procedures that require high throughput (e.g., screening) or involve sustained anesthesia to several subjects (e.g., repeated sampling) may benefit from this accessory system.

REFERENCES

1. Joshi, B., *Medical Imaging Instrumentation: Global Markets and Technologies Through 2022*.

2. *Medical Magnetic Resonance Imaging: Technologies and Global Markets*.

3. Branstetter, B.F., T.M. Blodgett, L.A. Zimmer, C.H. Snyderman, J.T. Johnson, S. Raman, and C.C. Meltzer, *Head and Neck Malignancy: Is PET/CT More Accurate than PET or CT Alone?* Radiology, 2005. **235**: p. 580-586.

4. Andrade, R.S., D.E. Heron, B. Degirmenci, P.A. Filho, B.F. Branstetter, R.R. Seethala, R.L. Ferris, and N. Avril, *Posttreatment assessment of response using FDG-PET/CT for patients treated with definitive radiation therapy for head and neck cancers.* Int J Radiat Oncol Biol Phys, 2006. **65**(5): p. 1315-1322.

5. Wu, M. and J. Shu, *Multimodal Molecular Imaging: Current Status and Future Directions.* Contrast Media Mol Imaging, 2018. **2018**: p. 1382183.

6. Beh, A., P.V. McGraw, B.S. Webb, and D. Schluppeck, *Linking Multi-Modal MRI to Clinical Measures of Visual Field Loss After Stroke.* Front Neurosci, 2021. **15**: p. 737215.

7. Pfob, A., C. Sidey-Gibbons, R.G. Barr, V. Duda, Z. Alwafai, C. Balleyguier, D.A. Clevert, S. Fastner, C. Gomez, M. Goncalo, I. Gruber, M. Hahn, A. Hennigs, P. Kapetas, S.C. Lu, J. Nees, R. Ohlinger, F. Riedel, M. Rutten, B. Schaefgen, M. Schuessler, A. Stieber, R. Togawa, M. Tozaki, S. Wojcinski, C. Xu, G. Rauch, J. Heil, and M. Golatta, *The importance of multi-modal imaging and clinical information for humans and AI-based algorithms to classify breast masses (INSPiRED 003): an international, multicenter analysis.* Eur Radiol, 2022. **32**(6): p. 4101-4115.

8. *Small Animal Imaging (In-vivo) Market Size, Share & Trends Analysis Report By Technology (Optical Imaging, Micro-Magnetic Resonance Imaging, Nuclear Imaging), By Application, And Segment Forecasts, 2012 - 2022*. Available from: https://www.grandviewresearch.com/industry-analysis/small-animal-imaging-in-vivo-market.

9. *Global Small Animal (In-Vivo) Imaging Market – Industry Trends and Forecast to 2029*. Available from: https://www.databridgemarketresearch.com/reports/global-small-animal-vivo-imaging-market.

10. *Global Small Animal Imaging (In-Vivo) Market Size, Share, Trends, COVID-19 Impact & Growth Analysis Report – Segmented By Modality, Reagent & Region (North America, Europe, APAC, Latin America, Middle East & Africa) - Industry Forecast (2022 to 2027)*. Available from: https://www.marketdataforecast.com/market-reports/small-animal-imaging-market.

11. *Small Animal Imaging (In-Vivo) Market by Modality (Optical Imaging, PET, SPECT, CT, MRI, ultrasound, Photoacoustic Imaging, Magnetic Particle Imaging), Reagent (Optical Imaging Reagents, Contrast Agents, PET Tracers, SPECT Probes) - Global forecast to 2021*. Available from: https://www.marketsandmarkets.com/Market-Reports/small-animal-imaging-market-957.html.

12. *Global Small Animal Imaging Market $2.9 Billion by 2027*. Available from: https://www.ihealthcareanalyst.com/growing-demand-adoption-preclinical-multimodal-devices-small-animal-imaging-market/.

13. Keppler, J.S., *A Cost Analysis of Positron Emission Tomography.* Am. J. Roentgenol., 2000. **177**: p. 1771-1731.

14. Gajuryal, S.H., A. Daga, V. Siddharth, C.S. Bal, and S. Satpathy, *Unit Cost Analysis of PET-CT at an Apex Public Sector Health Care Institute in India.* Indian J Nucl Med, 2017. **32**(1): p. 1-6.

15. Cherry, S.R., T. Jones, J.S. Karp, J. Qi, W.W. Moses, and R.D. Badawi, *Total-Body PET: Maximizing Sensitivity to Create New Opportunities for Clinical Research and Patient Care.* J Nucl Med, 2018. **59**(1): p. 3-12.

16. Zhou, I.Y., C.T. Farrar, J. Mandeville, M.S. Placzek, N.J. Rotile, C. Molinos Solsona, T. Sasser, S.A. Esfahani, M. Heidenreich, and P. Caravan, *Multi-Animal Simultaneous PET/MR Imaging*. Bruker BioSpin.

17. Soret, M., S.L. Bacharach, and I. Buvat, *Partial-volume effect in PET tumor imaging.* J Nucl Med, 2007. **48**(6): p. 932-945.

18. Bibb, R., D. Eggbeer, and A. Paterson, *Medical Imaging*, in *Medical Modelling: The Application of Advanced Design and Rapid Prototyping Techniques in Medicine*. 2014, Elsevier: Woodhead Publishing Series in Biomaterials. p. 8-34.

19. Wang, F.B., P.M. Cheng, H.C. Chi, C.K. Kao, and Y.H. Liao, *Axons of Passage and Inputs to Superior Cervical Ganglion in Rat.* Anat Rec (Hoboken), 2018. **301**(11): p. 1906-1916.

20. Wong, K.P., W. Sha, X. Zhang, and S.C. Huang, *Effects of administration route, dietary condition, and blood glucose level on kinetics and uptake of 18F-FDG in mice.* J Nucl Med, 2011. **52**(5): p. 800-807.

CHAPTER 3: DE-RISKING CUSTOM TOOLS TOWARDS COMMERCIALIZATION

3.1 Background

3D (3-dimensional) printing enables the rapid production of custom tools and is being increasingly utilized for fabrication in the life sciences[1-7]. A range of 3D printers employing different techniques (e.g. fused deposition modeling, stereolithography, selective laser sintering) are commercially available at varied price points, contributing to the growing ubiquity of 3D printers in research and educational spaces. The library of 3D-printable substrates now includes materials that are favorable for a range of applications in healthcare, including those with structural, electrical[1,8], biocompatible[9-11], or bioresorbable[5,13] properties of importance[14]. From 3D-printed organ on a chip designs[15], to 3D-printed bioimplants[16], to 3D-printed tissue scaffolds[17-18], 3D printing has become a critical tool in biomedical research.

Preclinical imaging is a rapidly growing research area, accelerating in recent years with the rise of modular and multi-modal imaging instruments. Multi-modality imaging combines the use of two or more biomedical imaging modalities to detect, treat, or monitor disease in living subjects. The use of multiple imaging techniques may offset the limitations of a particular technique, as is frequently done when computed tomography (CT) data is used to correct for positron emission tomography (PET) signal lost to attenuation. Alternatively, the combined information provided by multi-modal imaging approaches may improve diagnostic power as was seen for the detection of head and neck malignancies via PET/CT versus PET or CT alone[19]. As researchers pioneer new research spaces, they may find a need for a tool that is not commercially available and thus seek to make it themselves. To this end, 3D printing is frequently used to make these custom tools. Tools 3D-printed in-house have been used to manage research subjects during an experiment (for anesthesia[20], maintaining body temperature[21], or monitoring[22]), position samples for imaging (standards[23], phantoms[24], subjects[23, 25-26]), and reduce motion artifacts[27]. For example, a 3D-printed holder enabled neuroimaging of an awake rat in a clinical MR scanner[25]. Demands on imaging tools are greater in multi-modal imaging applications, necessitating a greater understanding for the properties of the materials used. Thus, it is critical to select the correct polymer for the application and limit interference in the study by introducing artifacts, attenuating signal, or eliciting an undesired signal from a responsive polymer.

Desirable characteristics for 3D printed materials for imaging applications include i. minimal interference with the imaging collection or analyses, ii. lack of toxicity to experimenter and research subjects, iii. rigid and not easily broken, iv. inexpensive to produce, and v. stable for cleaning using laboratory disinfection protocols. Practical considerations regarding the use of 3D-printable polymers in imaging applications, such as the decontamination of an accessory exposed to radioactive material, are often overlooked. Studies have characterized signal intensity (photoacoustic, magnetic resonance imaging), radiodensity (for PET, SPECT, CT)[29-35], and the impact of ionizing radiation[36] on 3D-printed phantoms, but for a limited selection of materials. Less is known about the optical properties of 3D-printed materials, with most fluorescence research focused on sorting select plastics and nano-plastics[37,38] for recycling and toxicology purposes. At this time, no resource that guides the selection of 3D printing material for manufacturing of custom tools in a preclinical molecular imaging lab is known.

This gap was addressed in the current study by characterizing the utility and limitations of 15 3D-printed materials within the context of biomedical imaging. To this end, the needs and expectations of preclinical imaging researchers were investigated to identify desirable material qualities and other features that would contribute to widespread application of custom tools. Customer discovery was conducted through informational interviews and assessment of the Managers of Molecular Imaging Laboratories instrument database. Select materials were printed from resins and filaments using a range of 3D printers and characterized for luminescence, fluorescence, radiodensity, and capacity for repeated cleaning. Radioactive contamination is a standing risk in radiology. Thus, a 3D-printed material's capacity for decontamination following radiotracer exposure was evaluated. This report compares the performance of desirable and common materials in different imaging practices to de-risk future custom imaging tools, providing the information necessary for manufacturers and researchers alike to choose the best material for their application.

3.2 Materials and Methods

3.2.1 Customer Discovery

Two approaches were used to identify customer needs that our high-throughput imaging approach may address. First, a list of interview questions was made for potential end users in collaboration with the Technology Transfer Office at Michigan State University. End user interview

questions were designed to identify the needs and wants of preclinical molecular imaging researchers. Questions focused on imaging volume, costs, challenges, needs, desirables, and familiarity with potential competing products. Interest group pages from the Society for Nuclear Medicine and Molecular Imaging Society's website were screened for committee member contact information. The flyer in Appendix A (Figure 3.8) was sent with a request to meet for an informational interview. The contact list consisted of PET, CT, MR, and SPECT users (alone and in combination) with a range of specializations.

The second approach utilized the instrument database provided by the Managers of Molecular Imaging Laboratories (MOMIL) Interest Group, which is available to members of the World Molecular Imaging Society. The database is a repository for molecular imaging lab managers to list the instrumentation available at their institution. The database was used to identify the most popular preclinical imaging instruments, where they are located, and engage with their managers to gain end user insights and develop relationships that may lead to future sales or collaborations. The same materials described previously were used for accepted informational interview requests.

3.2.2 Value-in-use Estimate

The high-throughput imaging tools described in Chapter 2 (referred to as "TEC2022-0027" in this section) could improve the cost effectiveness of preclinical PET/MR by helping researchers gather more data for the time invested. A value-in-use study was conducted in collaboration with the

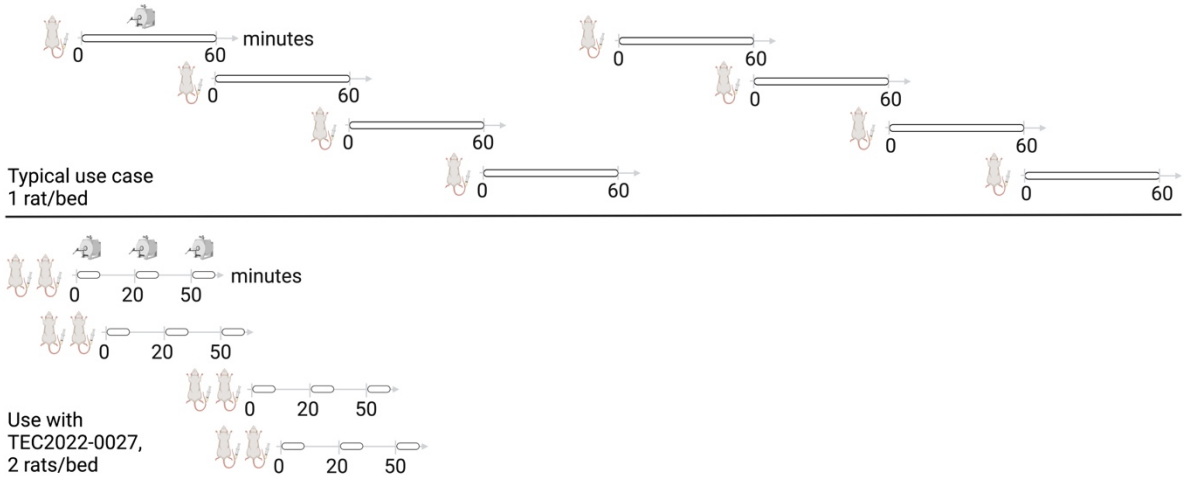

Figure 3.1. Typical use case to build a 1-hour time activity curve in rats versus use with the Chapter 2 longitudinal rat imaging approach. This schedule assumes 5-minute PET bins.

Technology Transfer Office at Michigan State University to estimate a reasonable price point for the high throughput accessory system. The study was designed to compare the longitudinal imaging experiment described in section 2.3.4 to typical methods used to generate a 1-hour time-activity curve in rats (1 full hour of scanning). The 2.3.4 approach can be used to gather longitudinal data if the desired imaging timepoints are known (may require a pilot study) and spaced such that other subjects can be scanned between them. A visual comparison of the two approaches can be seen in Figure 3.1.

The assumptions given in Table 3.1 were used to calculate product value in high and occasional users of MRI alone or combined PET/MRI. For these purposes, occasional use was defined as scanning 8 animals/day once weekly for a year. High use was defined as scanning 8 animals/day daily for 50 weeks. Time estimates were doubled from a real experiment of half the sample size for values in the “Use with TEC2022-0027” column.

Metric	**Typical use case**	**Use with TEC2022-0027**
Number of beds used	1	4
Samples/bed	1	2
Samples/day	8	8
PET/MR use rate ($/per hour)	$ 307	$ 307
MR use rate ($/per hour)	$ 185	$ 185
Set-up time (hours)	1	1
MRI scan time (hours)	8	2
Animal exchanges (hours)	2	0.5
Cleanup (hours)	1	1
Total time (hours)	12	4.5

Table 3.1. Assumptions for value-in-use calculations.

Annual value generated was defined as the difference between annual instrument use costs for the typical use case subtracted by the TEC2022-0027 annual costs. The value of each bed unit was determined by dividing the annual cost savings by the number of beds used. Split of value to the customer was set to 20% multiplied by the value per bed unit to determine the final value captured price.

3.2.3 Design of Template Print and Selection of Materials

Materials with the following characteristics were prioritized: low density, water resistant, water resistant, and capacity of withstanding high temperatures. Heat deflection temperature (HDT), tensile strength, and water absorbance values were collected from the literature. Reports that utilized standard industry procedures were sought and supplemented with manufacturer reports or the literature as needed[39-55]. Not all materials had published data for metrics of interest. Selected materials were printed with 100% infill with two exceptions (see Figure 3.3 for explanation).

A template was designed using Autodesk Fusion 360 that included components that are common to imaging accessories or were highlighted as desirable in end-user interviews (Figure 3.2). The template print (5 x 5 x 1.5 cm, L x W x H) included raised and recessed features such as a ruler and standardized air connectors for the former, and a circular breathing pad, valleys for embedded tubing lines, and two threaded screw holes for the latter. Numbers varying in size (2-7 mm) were also included in raised and recessed formats.

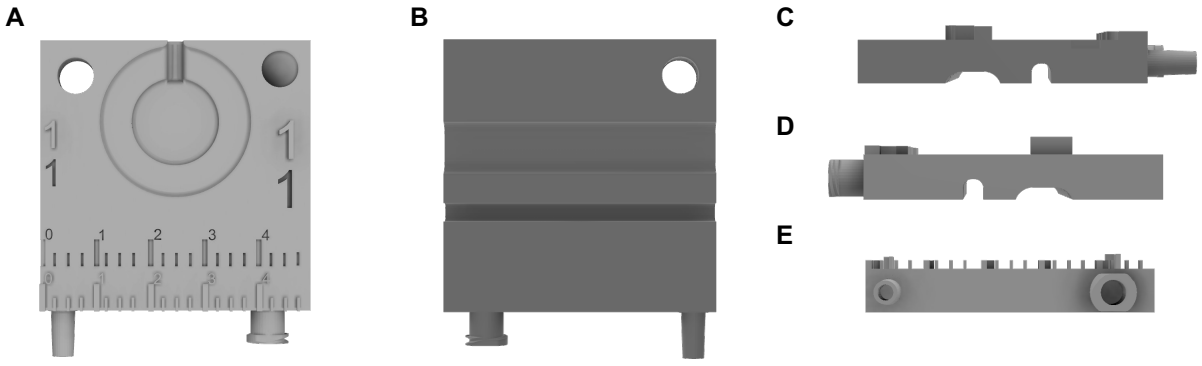

Figure 3.2. Evaluated materials were printed using the same template file. A. Front face of template file. High and low relief of numbering in various sizes, rulers, and various connectors are visible. B. Back face of template file. Grooves for tubing are visible. C-E. Profile of template print. High reliefs and connectors are visible.

3.2.4 Optical Emission Testing

Optical emission properties were evaluated for 3D-printed materials using the IVIS Spectrum System (Perkin Elmer). Phosphorescence was quantified by capturing photons emitted following a photograph camera flash with an open emission filter. Fluorescent properties were tested following excitation at 500, 575, 675, and 750 nm (30 nm bandwidth), corresponding to GFP, mCherry, Cy5.5, and Alexa Fluor 750 fluorophores. Emission filters (20 nm bandwidth) were used at 540, 620, 720, and 800 nm, respectively. For all images, a high lamp level was used to capture a 6.6 x 6.6 cm image (field of view setting B, subject height 1 cm) with medium binning. Exposure time was automatically determined by the instrument. Living Image software was used for data analysis using standardized ROIs. Net epifluorescence ((photons/s)/(μW/cm^2)) and total flux (photons/s) were determined by subtracting the background ROI from the material ROI by the using the adaptive background subtraction tool, per the gold standard in luminescence imaging by IVIS.

3.2.5 Radiodensity Assessment by μCT Imaging

A μCT scan was acquired for each material before and after the decontamination procedure using a Perkin Elmer QuantumGX microCT scanner (72 mm; 288 μm reconstruction resolution FOV; 8 second scan gantry rotation time x3 overlap stitched; 90kVe/88uA power setting; Al+Cu x-ray filter; 399 slices). Image analysis was conducted using PMOD 4.2. Radiodensity was quantified by averaging 3 spheres of 3 mm radius and normalizing to the signal of water. Materials that were not printed with 100% infill were excluded. Mean material radiodensity was compared using a one-way ANOVA followed by post-hoc Tukey's Test in GraphPad PRISM software.

3.2.6 Decontamination of Radionuclide

A radioactive spill test was conducted to assess each material's resistance to contamination and liquid absorption. F-18-FDG was acquired from Cardinal Health. 30 μL droplets of F-18-FDG (n=4/material) were placed on each template print (activity per dose 38.8 μCi). Printed templates were then disinfected with 70% ethanol and dried clean with a Kime wipes after 5 minutes. The radioactivity of each template print was assessed before and after decontamination using a Ludlum Model 3 pancake probe (model 44-9, Serial no. PR059981) and a Capintec Inc. CRC-25R dose calibrator (Serial no. 113464). The activity on the template print was measured in the

bottom of the dose calibrator well for the CRC-25R and recorded as μCi. For the Ludlum pancake probe, template print activity was measured from the same distance and location each time. Activity was recorded as average counts per minute. Residual activity was calculated as the difference between the pre- and post-contamination measurements after decay-correction to the same timepoint. Mean residual activity was compared for different materials using a one-way ANOVA followed by post-hoc Tukey's test in GraphPad (Prism). One datapoint was determined an outlier and removed by Dixon's test[56].

3.2.7 Capacity for Repeated Cleaning

Two months of moderate use was simulated for the 3D printed part, assuming disinfection before and after use 3 times per week. This was done to determine which materials swelled or shrank after being exposed to water and solvent cleaners. The disinfection protocol was selected according to the CDC standards for the disinfection of smooth, hard surfaces (non-critical items) at healthcare facilities[57,58]. Each round of disinfection included saturation of the surface with a Phenolic germicidal detergent solution (Sporicidin, Contec) for 5-10 minutes, scrubbing with a soft bristle brush and water, and saturation of the surface with 70% ethanol. After the decontamination protocol, template prints were imaged by the same methods used previously. Degradation following repeated decontamination was assessed by comparing the volume of automatically segmented ROIs in pre- and post-decontamination μCT scans, respectively.

3.2.8 Heatmap

Heat maps were created to make comparisons easier and allow selection of the best suited material for particular needs. Color values were assigned by normalizing mean values reported in Figures 3.2-3.4 to the largest value in that dataset using the batlow color map (40-80% range used, centered on 60%). The batlow scientific color map avoids visual distortion of data and is accessible to readers with color vision deficiencies[59]. White cells indicate a lack of data for that metric and material (see Figure 3.3 for explanations).

3.3 Results

3.3.1 End User Desirables Identified Through Customer Discovery

The concerns of end users (n=6 interviewed) were sorted into 3 categories: subject welfare, material properties, and ease of use (Table 3.2. The bed design described in Chapter 2 included 5 of the 13 features in Table 3.2 at the time of the interviews. The remaining properties were included in prospective material evaluations (*), incorporated into the updated bed design (**), or will be explored in the future (***).

Subject welfare	**Material properties**	**Ease of use**
Animal heating component	Autoclavable***	Flexibility in species and set-up
Respiration pad	Water repellant*	Stackable***
Temperature probe	Low attenuation material*	Click and go**
Organizational guides for accessories**	Minimal material to reduce attenuation**	Docking station
		No system modifications needed

Figure 3.2. Desirable features for a high throughput rodent imaging bed as given during informational interviews with potential end users. Users highlighted the need to be able to monitor subject wellness while scanning using existing monitoring tools. Additionally, organizational guides were requested to keep tubing, wires, and other accessories secure and safe from interfering with subject access. One asterisk indicates that the property was evaluated during material screening, two asterisks indicate that the element was incorporated into the updated design, and three asterisks indicate where future efforts will be directed.

Per the Managers of Molecular Imaging Laboratories (MOMIL) instrument lists, the most reported preclinical imaging instruments included the 7T Bruker BioSpec 70/30 MRI (Bruker, Billerica, Massachusetts, United States), Perkin Elmer IVIS Spectrum (Perkin Elmer, Waltham, Massachusetts, United States), Seimens PET/CT and SPECT/CT (Siemens, Munich, Germany), and Mediso nanoScan SPECT/CT/PET (Mediso, Budapest, Hungary). The ultrasound imaging instrument made by Visual Sonics was also among the most reported but was not identified as a

target due incompatibility with our high-throughput imaging approach. Field of view and scanning bed dimensions were collected from manufacturer materials (print materials gathered at the 2022 Society for Nuclear Medicine and Molecular Imaging Conference and World Molecular Imaging Conference) and used to refine the geometry of the updated design for the custom bed unit.

3.3.2 Value-in-use Estimate

The value captured price ranged from $3,753 to $29,052 for a 4-unit custom bed set (Table 3.3). Given that MRI use is forecasted to grow in coming years[60], the product value may continue to grow.

Modality	Use level	Annual value generated	Value per bed unit	Split of value to customer	Value captured price (per unit)
PET/MR	High	$ 581,043	$ 145,260	0.8	$ 29,052
PET/MR	Occasional	$ 120,768	$ 30,192	0.8	$ 6,038
MR	High	$ 352,556	$ 88,139	0.8	$ 17,627
MR	Occasional	$ 75,071	$ 18,767	0.8	$ 3,753

Table 3.3. The value captured price per unit for 4 use cases.

This study concludes that the savings from the new bed system are so significant that pricing can be set at a high level. Potential end users indicated that they would be willing to pay $3,000 on average for the 4-bed system and staging area as shown in Chapter 2. Given the variability in use rates, a pricing scheme that allows users to purchase the number of beds needed for their imaging volume would provide flexibility that parallels the imaging approach. Thus, a base cost of $1,200 for the staging area and an additional $1,200 per bed unit would cost occasional users $3,600 for 2 beds and high-volume users $6,000 for 4 beds. A price point between the lowest value captured price and user estimates would maintain a competitive position and speed market penetration.

3.3.3 Design of Template and Printing of Materials

A total of 15 materials were selected for printing and further testing per the workflow given in Figure 3.3 (see Figure 3.4 legend below for full list and their acronyms). Their physical properties of interest are summarized in Figure 3.4. The selected materials were printed via both stereolithography (SLA) and fused deposition modeling (FDM) 3D-printing methods. Templates were printed from 5 printers: LulzBot (FDM), Ultimaker S5 (FDM), Polymaker: Polysher (FDM), Formlabs 3B (SLA), and Stratasys J750 (SLA). SLA printers outperformed FDM in print quality due to their ability to print with higher resolution, even down to 2 mm numbers. The 2 mm length numbers were only visible in one FDM print, PC-ABS. The SLA prints also had a smoother surface that lacked print lines inherent to FDM printing. Many FDM prints had frayed edges and lingering

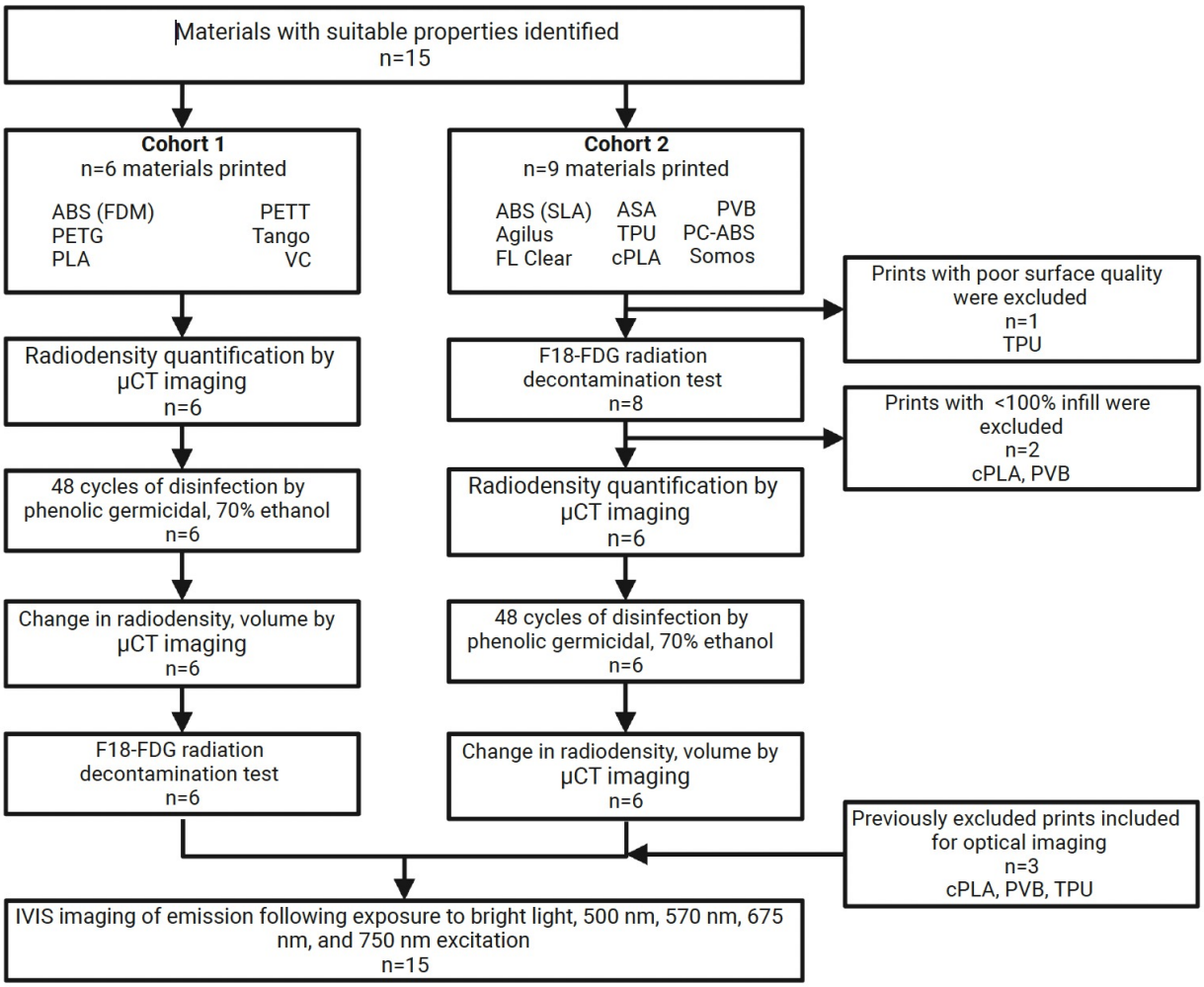

Figure 3.3. Workflow for material evaluation. Materials in cohort 1 were acquired before cohort 2. Cohort 1 and cohort 2 performance was analyzed simultaneously.

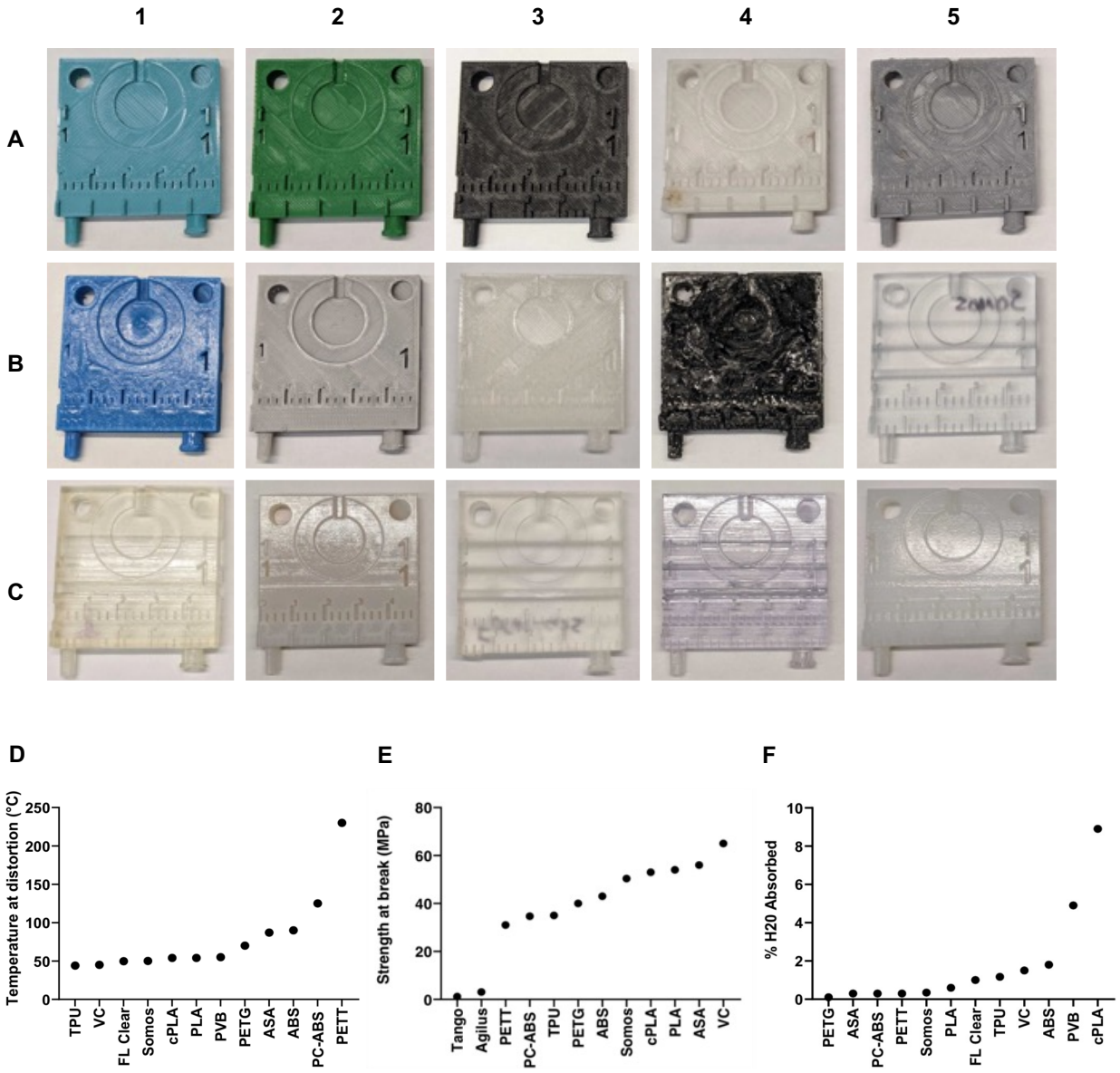

Figure 3.4. Overview of prints and characteristics for selected materials. A1-C5. Front face image of template, 3D printed from A1. Polyethylene terephthalate glycol (PETG). A2. Polylactic acid (PLA). A3. Polycarbonate-acrylonitrile butadiene styrene (PC-ABS). A4. PETT taulman t-glase (PETT). A5. Acrylonitrile butadiene styrene (ABS) printed via FDM. B1. Polyvinyl butyral (PVB). B2. Acrylonitrile styrene acrylate (ASA). B3. Crystalized polylactic acid (cPLA). B4. Thermoplastic polyurethane (TPU). B5. Somos watershed XC 11122 (Somos). C1. Tango. C2. ABS printed via SLA. C3. Clear Formlabs Resin (FL Clear). C4. VeroClear (VC). C5. Vero + Agilus 30 (Agilus). D-F. Corresponding heat deflection temperatures (HDT, D), tensile strength (F), water absorbance (F) for selected materials.

support material, which limited fine detailing. Regarding material properties, PETT, PC-ABS, and ABS have the highest temperature threshold at distortion (Figure 3.4D), whereas TPU, VC, and FL Clear distort at the lowest temperatures. PETG, PETT and PC-ABS ranked lowest in percentage of water absorbed (Figure 3.4E), whereas cPLA, PVB and ABS ranked the highest.

VC, ASA, and PLA are the materials with the highest tensile strength (Figure 3.4F). Tango and Agilus, being pliable materials, have the lowest strength at break values.

3.3.4 Optical Emission Testing

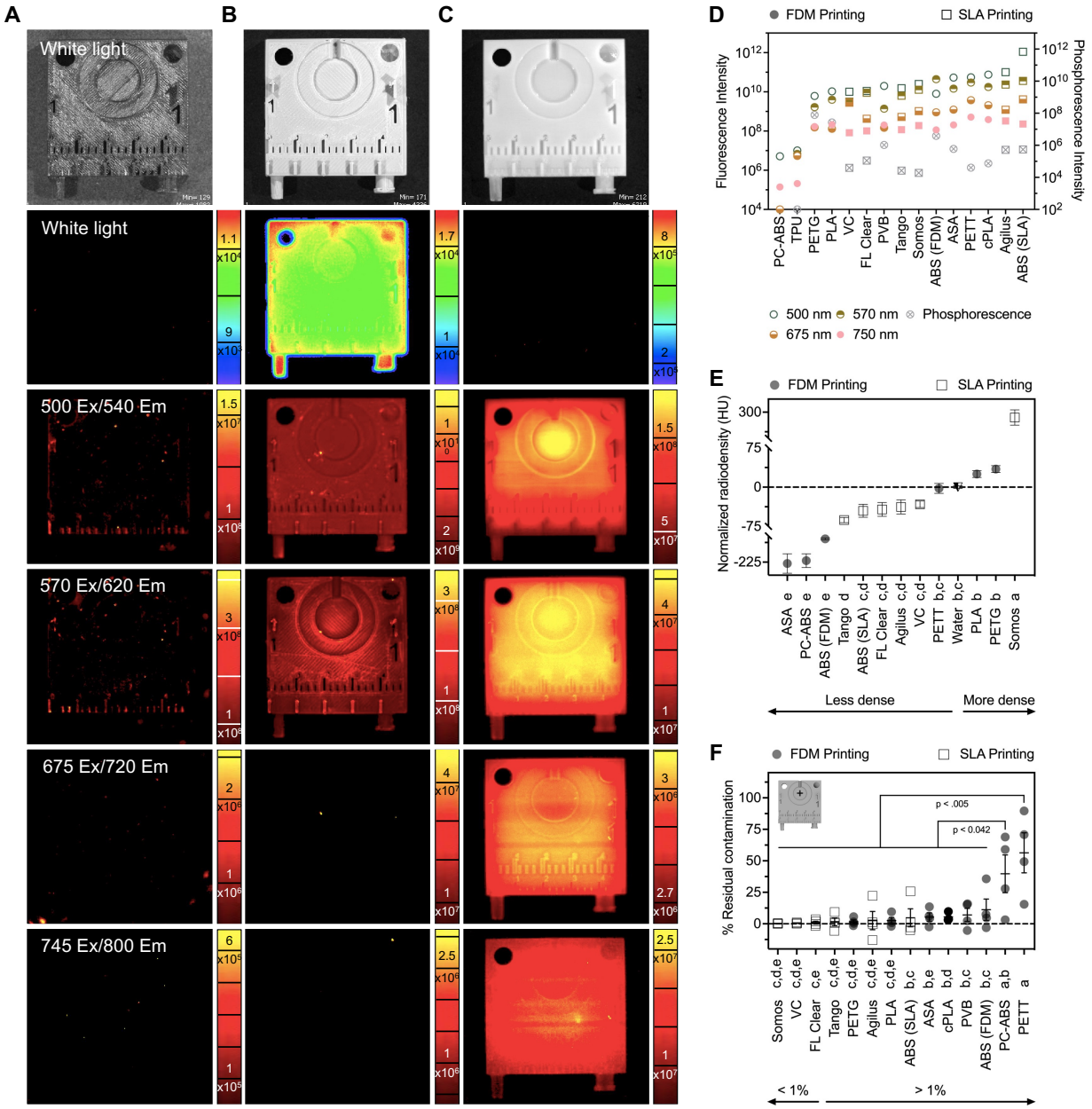

Figure 3.5. Applications of 3D printed materials in biomedical imaging. A-C. Representative images of a 3D printed material with low emission overall (A: PC-ABS), high phosphorescence intensity (B: PETG, photons/s), and high fluorescence intensity (C: SLA ABS, (photons/s)/(μW/cm2)). D. Normalized fluorescence and phosphorescence signal for 3D printed materials. E. Radiodensity for 3D printed materials normalized to water (dotted line) prior to repeated cleaning. F. Decontamination efficacy for F-18-FDG-exposed prints (exposure at crosshairs on inlay image), given as a percentage of residual activity. Materials with statistically different means are indicated by a shared letter beneath the x-axis. Data given as mean ± SEM. Em = Emission, Ex = Excitation.

Materials that emit light following excitation by wavelengths in the visible and near infrared spectrum may interfere with optical imaging techniques (e.g., fluorescence, bioluminescence). Tested materials demonstrated a range of optical emission properties, including low optical emission overall (PC-ABS, Figure 3.5A), high phosphorescence (PETG, Figure 3.5B), and high fluorescence (SLA ABS, Figure 3.5C). Most materials had little to no phosphorescence. FDM ABS, PLA, PETG, and PVB were the only 4 materials that had phosphorescence intensity over 10^6 flux (photons/sec). SLA ABS, Agilus, cPLA, PETT, and ASA were each in the top 5 for highest fluorescence intensity for each excitation wavelength tested (Figure 3.5D). PLA, FDM ABS, and VC also showed appreciable fluorescence following excitation with 500, 570, and 675 nm wavelengths, respectively. Interestingly, PC-ABS and TPU both had corrected signal intensity values of zero for phosphorescence, as well as fluorescence at 570 and 675 nm. All other materials demonstrated some fluorescence in response to excitation by all wavelengths tested, albeit less above 650 nm.

3.3.5 Radiodensity Assessment by μCT Imaging

Materials with high radiodensity are less desirable for nuclear imaging applications (e.g., PET, SPECT) due to expected loss of signal due to attenuation. Materials fell into 1 of 5 groups of statistically non-different means, grouped in the following sets: (a) Somos, (b) PETG, PLA, PETT (equivalent to radiodensity of water), (c) PETT, VC, Agilus, FL Clear, and SLA ABS (equivalent to radiodensity of water), (d) VC, Agilus, FL Clear, and SLA ABS, and (e) comprising FDM ABS, PC-ABS, and ASA. PLA, PETG, and Somos watershed XC 11122 were the only materials with higher radiodensity than water (Figure 3.3E). ASA, PC-ABS, and FDM ABS were the least radiodense, with all remaining materials falling between fat and water (-50 to 0 HU on CT).

3.3.6 Decontamination of Radionuclide

Materials with low residual radioactivity were considered easier to clean and more resistant to contamination. PC-ABS and PETT absorbed over 25% the original radiation dose, setting this pair apart from the rest of the panel for risk of contamination. SLA ABS, ASA, cPLA, PVB, and FDM ABS performed similarly to one another, each retaining > 4.75% of activity (**Figure 3f**). No statistical differences were observed for the remaining materials (Somos, VC, FL Clear, Tango, PETG, Agilus, PLA), which ranged from 0.19% residual contamination for Somos to 2.6% for PLA. Somos and VC stood apart as having high repeatability relative to other materials. Interestingly,

the prints which retained the greatest fraction of radioactivity were overwhelmingly printed via FDM.

3.3.7 Capacity for Repeated Cleaning

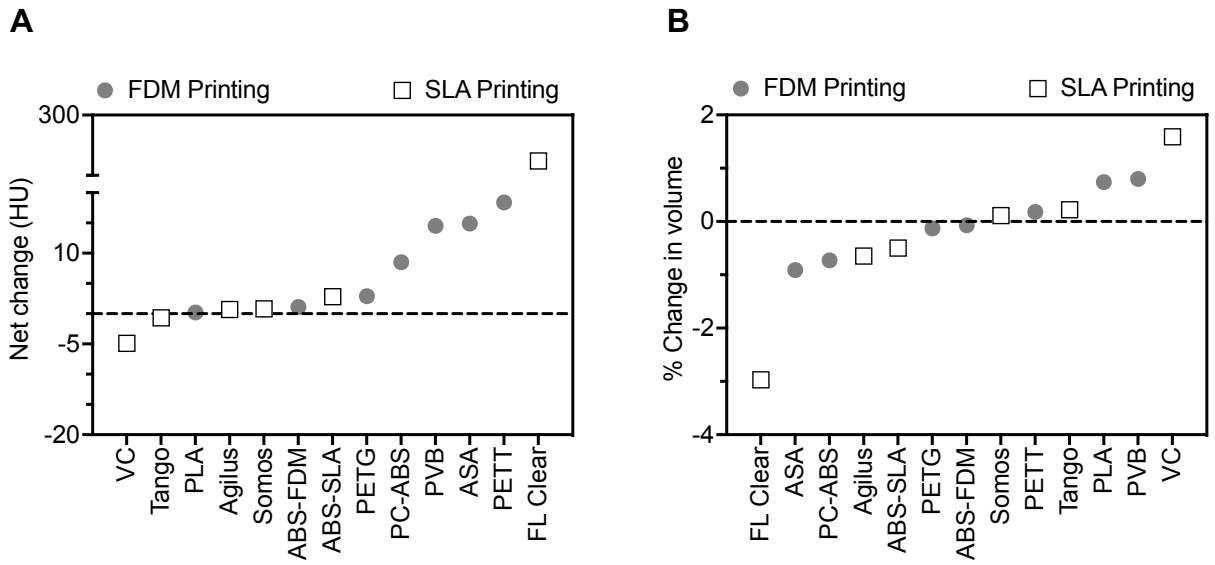

Figure 3.6. Net change in radiodensity (A) and volume (B) following 2 months of simulated use.

Following 2 months of simulated use, materials were assessed for change in radiodensity and volume. The greatest change in radiodensity was observed in FL Clear, followed by PETT, ASA and PVB (Figure 3.6A). The remaining materials showed negligible changes in radiodensity. Increase in volume for VC, PLA, and PVB may indicate swelling from water absorption (Figure 3.6B). FL Clear, ASA, and PC-ABS likely experienced degradation as indicated by a reduction in volume, although at low levels (0.16-0.5 cm^3 difference). Negligible changes to volume were seen in remaining materials following the decontamination protocol.

3.3.8 Heatmap

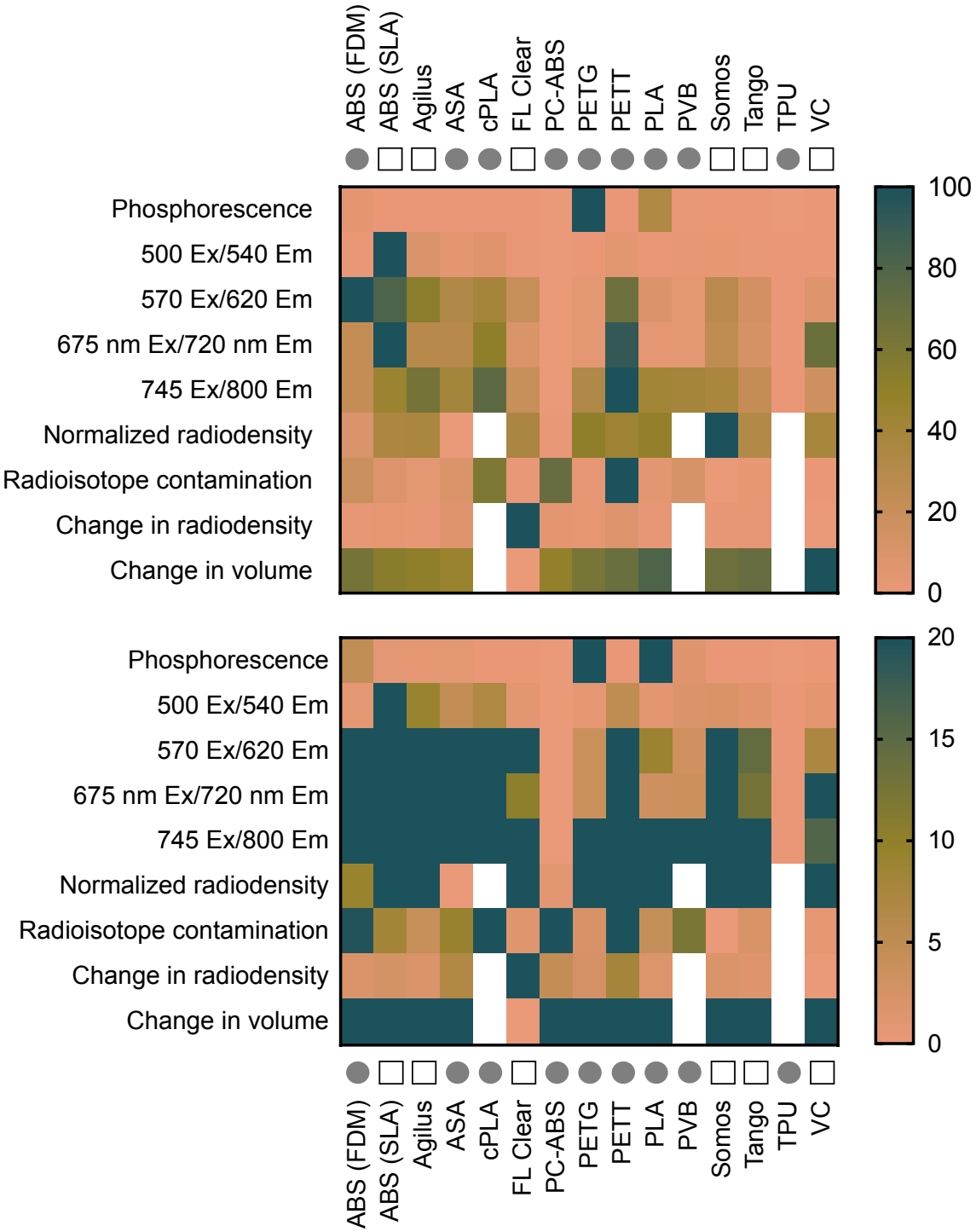

Figure 3.7. Performance summary for each 3D printed material given in alphabetical order as a percentage of the largest value in each row. The range of values is given in 0-100% (top) and 0-20% (bottom) maximum ranges. Circles denote printing by FDM, squares denote printing by SLA.

The heatmap presented in Figure 3.7 highlights the range of material performance for our selected metrics, which was wide for some tests and narrow for others. The heatmap also helps to quickly identify materials stand apart from on particular tests. For example, most materials are not of concern for phosphorescence, aside from PETG, PLA, and FDM ABS. Similarly, most materials did not experience major changes in radiodensity values aside from FL Clear. Overall, PC-ABS demonstrated the lowest concern for interference from competing light emission across excitation wavelengths. Materials which quickly absorbed radionuclide are also highlighted (e.g., PETT, PC-ABS, and FDM ABS), and may be avoided for applications where contamination is a concern. With a quick glance, this plot highlights the categories in which the tested materials perform similarly (e.g., phosphorescence, change in volume, radiodensity following decontamination cycles), and those where materials are quite different from each other (e.g., radiodensity, capacity for contamination).

3.4 Discussion

Custom tools are commonly 3D printed by molecular imaging scientists to aid in their research[20-22,25]. However, they are frequently built for specific use. We've outlined a framework to seek user needs that were incorporated into the next iteration of the high throughput imaging accessory system. Value-based determinations were made for a potential future pricing scheme that will accelerate penetration of this product into the market. Additionally, regulatory concerns were addressed by demonstrating that materials withstand cycles of cleaning via CDC-recommended methods. Commercialized technologies have the potential for greater impact. Thus, a similar approach should be considered for custom research tools built for widely practiced, or widely desired, techniques.

Until now there has been no central resource that compared polymer properties relevant to common molecular imaging techniques. The current study addressed this gap by reporting a variety of metrics that included radiodensity, durability, and optical emission profiles for a panel of 15 3D printable substrates. The polymer panel included materials ubiquitous to laboratory spaces, including PETG, PETT, ABS, TPU, and PC-ABS. Typical routine disinfection methods were applied that included disinfection with 70% ethanol and a germicidal agent. Imaging methods included μCT, phosphorescence, and fluorescence imaging. These studies can serve

as a resource for biomedical engineers to efficiently select materials that suit their needs from a range of filaments, including many that are commonly used and affordable.

Each material demonstrated trade-offs for molecular imaging applications. Thus, materials should be selected for each specific application. For example, Tango performed desirably in all tests but has the lowest reported tensile strength of the evaluated materials. Thus, Tango will not interfere with imaging, but was not well suited for applications requiring strength or structure. Similarly, PC-ABS had a low radiodensity and optical emission profile but demonstrated changes following repeated cleaning and rapidly absorbed 40% of applied F-18-FDG. Materials may degrade under some conditions but not others. For example, ASA and PETG both had high deflection temperatures, useful for tools needing to withstand high heat (and/or high pressure such as autoclaving) yet prints from both materials experienced radiodensity and/or volume changes with repeated use, jeopardizing the long-term use of the material.

Several materials were identified for their performance in different imaging domains. Materials in the vertical center of the heatmap (Figure 3.7) may be preferred by optical imaging scientists due to their low response to light excitation, particularly PC-ABS and TPU. Alternatively, researchers interested in making fluorescence imaging makers may benefit from a light-emitting polymer on the heatmap's vertical left. ABS, Agilus, cPLA, PETT, ASA, PLA, and VC were not recommended for luminescence-focused applications. Regarding nuclear imaging, VC, FL Clear, Tango, PETG, and Agilus demonstrated the lowest level of residual contamination following cleaning and were similarly or less radiodense than water. Of this group, Tango, Agilus, and PETG also experienced little change to volume or radiodensity following repeated cleaning cycles. Thus, these three would make good construction materials for custom tools in nuclear imaging. For μCT applications where contamination is not of concern, ASA, PC-ABS, or FDM ABS may be desirable due to their low radiodensity and thus, low expected signal attenuation. Even Somos (the most radiodense material) was not a significant concern, given that its Hounsfield Units (HU) was equivalent to soft tissue values[61]. Regarding mechanical function, tools which will be frequently exposed to liquid but need to retain shape for form and function should be built from PETG, since it has demonstrated low water (Figure 3.4F) and F-18-FDG absorbance (Figure 3.5F). ASA or VeroClear would be well suited for tools needed to withstand high mechanical stress. Overall, FDM printing was a low-cost relative to SLA for printers, materials, and repair. However, this study highlighted risks associated with residual contamination that may inform decision making for applications involving hazardous materials. This tradeoff may be acceptable due to the low cost

of FDM printing filaments, where a contaminated part could be replaced for $0.25/g of material. The SLA resins tested are recommended for applications that require fine details, low risk for contamination, or low radiodensity. No polymer tested performed ideally in every category.

This work could be expanded in several ways. First, one could conduct in vivo imaging with animals using these materials to see how much signal would be attenuated for the various imaging modalities. Second, these 3D-printed materials could be further characterized for other applications such as cell culture and capacity to withstand autoclaving. Lastly, branching this work into other fields such as tissue engineering (fluorescent scaffolds) and drug delivery (fluorescent nanoparticles) may be of future interest. Furthermore, the results presented may have utility in the manufacturing of biomedical imaging tools, driving development towards materials with improved performance in the domains that were highlighted.

REFERENCES

1. Rosario, M., H.S. Heil, A. Mendes, V. Saggiomo and R. Henriques, *The Field Guide to 3D Printing in Optical Microscopy for Life Sciences*. Adv Biol, 2021. **6**(4).

2. Fullerton, J.N., G.C.M. Frodsham and R.M. Day, *3D Printing for the Many, Not the Few*. Nat Biotechnol, 2014. **32**(11): p. 1086-1087.

3. Willson, K. and A. Atala, *Medical 3D Printing: Tools and Techniques, Today and Tomorrow*. Annu Rev Chem Biomol Eng, 2022. **13**: p. 481-499.

4. Sulkin, M.S., E. Widder, C. Shao, K.M. Holzem, C. Gloschat, S.R. Gutbrod and I.R. Efimov, *Three-dimensional Printing Physiology Laboratory Technology*. Am J Physiol, 2013. **305**: H1569-H1573.

5. Masud, S., *A 3D Printed Quick Response Encoded Orodispersible Film for Personalized Medicine*. Brac University, 2021.

6. Hong, C.X., S. Zhang, A. Eltahawi, A. Borazjani, H. Kalami, A.N. San, D. Sham, G. Ameri and C.D. McDermott, *Patient-specific Pessaries for Pelvic Organ Prolapse Using Three-dimensional Printing: A Pilot Study*. Urogynecology, 2023.

7. Tartaglia, G.M., A. Mapelli, C. Maspero, T. Santaniello, M. Serafin, M. Farronato and A. Caprioglio, *Direct 3D Printing of Clear Orthodontic Aligners: Current State and Future Possibilities*. Materials, 2021. **14**(7): p. 1799.

8. Ghoshal, S., *Polymer/carbon Nanotubes (CNT) Nanocomposites Processing Using Additive Manufacturing (Three-Dimensional Printing) Technique: An Overview*. Fibers, 2017. **5**(4): p. 40.

9. DraftWhite™. Stratasys, 2021. Available at: https://www.stratasys.com/en/materials/materials-catalog/polyjet-materials/draftwhite/. (Accessed: 8th March 2023)

10. Biocompatible 3D Printing Materials. Stratasys, 2018. Available at: https://www.stratasys.com/en/materials/materials-catalog/polyjet-materials/biocompatible/. (Accessed: 8th March 2023)

11. Tissuematrix. Stratasys, 2022. Available at: https://www.stratasys.com/en/materials/materials-catalog/polyjet-materials/tissuematrix/. (Accessed: 8th March 2023)

12. 3D Printing Materials for Healthcare. Formlabs, 2023. Available at: https://formlabs.com/materials/medical/. (Accessed: 8th March 2023)

13. Karanth, D., K. Song, M.L. Martin, D.R. Meyer, C. Dolce, Y. Huang and L.S. Holliday, *Towards Resorbable 3D-printed Scaffolds for Craniofacial Bone Regeneration*. Orthod Craniofac Res, 2023.

14. Ligon, S.C., R. Liska, J. Sampfl, M. Gurr and R. Mülhaupt, *Polymers for 3D Printing and Customized Additive Manufacturing*. Chem Rev, 2017. **117**(15): p. 10212-10290.

15. Barbaresco, F., M. Cocuzza, C.F. Pirri and S.L. Marasso, *Application of a Micro Free-flow Electrophoresis 3D Printed Lab-on-a-chip for Micro-nanoparticles Analysis*. Nanomaterials, 2020. **10**(7): p. 1277.

16. Bachtiar, E.O., O. Erol, M. Millrod, R. Tao, D.H. Gracias, L.H. Romer and S.H. Kang, *3D Printing and Characterization of a Soft and Biostable Elastomer with High Flexibility and Strength for Biomedical Applications*. J Mech Behav Biomed Mater, 2020. **104**: Article 103649

17. Babilotte, J., B. Martin, V. Guduric, R. Bareille, R. Agniel, S. Roques, V. Heroguez, M. Dussauze, M. Gaudon, D. Le Nihouannen and S. Catros, *Development and Characterization of a PLGA-HA Composite Material to Fabricate 3D-printed Scaffolds for Bone Tissue Engineering*. Mat Sci and Engineering C, 2021. **118**: Article 111334.

18. Alam, F., V.R. Shukla, K.M. Varadarajan and S. Kumar, *Microarchitected 3D Printed Polylactic Acid (PLA) Nanocomposite Scaffolds for Biomedical Applications*. J Mech Behav Biomed Mat, 2020. **103**: Article 103576.

19. Branstetter 4th, B.F., T.M. Blodgett, L.A. Zimmer, C.H. Snyderman, J.T. Johnson, S. Raman and C.C. Meltzer, *Head and Neck Malignancy: Is PET/CT More Accurate than PET or CT Alone?* Radiology, 2005. **235**(2): p. 580-586.

20. Kiehl, E.L., S. Stojadinovic, K.T. Malinowski, D. Limbrick, S.C. Jost, J.R. Garbow, J.B. Rubin, J.O. Deasy, D. Khullar, E.W. Izaguirre, P.J. Parikh, D.A. Low and A.J. Hope, *Feasibility of Small Animal Cranial Irradiation with the microRT System*. Med Phys, 2008. **35**(10): p. 4735-4743.

21. Gutruf, P., R.T. Yin, K.B. Lee, J. Ausra, J.A. Bennan, Y. Qiao, Z. Xie, R. Peralta, O. Talarico, A. Murillo, S.W. Chen, J.P. Leshock, C.R. Haney, E.A. Waters, C. Zhang, H. Luan, Y. Huang, G. Trachiotis, I.R. Efimov and J.A. Rogers, *Wireless, Battery-Free, Fully Implantable Multimodal and Multisite Pacemakers for Applications in Small Animal Models*. Nat Commun, 2019. **10**(1): p. 5742.

22. Bing, C., J. Nofiele, R. Staruch, M. Ladouceur-Wodzak, Y. Chatzinoff, A. Ranjan and R. Chopra, *Localised Hyperthermia in Rodent Models Using an MRI-Compatible High-intensity Focused Ultrasound System*. Int J Hyperthermia, 2015. **31**(8): p. 813-822.

23. Mollet, P., K. Braeckman, K. Deprez, J. Courtyn and S. Neyt, *Quantitative Performance Evaluation of a High-resolution High Sensitivity PET System: Single vs. Multi-mouse Imaging*. J Nucl Med, 2021. **62**(supplement 1): Abstract 1438.

24. Lennie, E., C. Tsoumpas and S. Sourbron, *Multimodal Phantoms for Clinical PET/MRI* EJNMMI Phys, 2021. **8**(1): p. 62

25. Greenwood, H.E., Z. Nyitrai, G. Mocsai, S. Hobor and T.H. Witney, *High-throughput PET/CT Imaging Using a Multiple-mouse Imaging System*. J Nucl Med, 2020. **61**(2): p.292-297.

26. Zhou, I., C. Farrar, J. Mandeville, M.S. Placzek, N. Rotile, C. Molinos-Solsana, T. Sasser, S. Esfahani, M. Heidenreich and P. Caravan, *Multi-animal Simultaneous PET/MR Imaging*. Biology, 2020.

27. Donohoe, D.L., K. Dennert, R. Kumar, B.P. Freudinger and A.J. Sherman, *Design and 3D-printing of MRI-compatible Cradle for Imaging Mouse Tumors*. 3D Print Med, 2021. **7**(1): p. 33

28. Stenroos, P., J. Paasonen, R.A. Salo, K. Jokivarsi, A. Shatillo, H. Tanila and O. Gröhn, *Awake Rat Brain Functional Magnetic Resonance Imaging Using Standard Radio Frequency Coils and a 3D Printed Restraint Kit*. Front Neurosci, 2018. **12**: p. 548

29. Bieniosek, M.F., B.J. Lee and C.S. Levin, *Technical Note: Characterization of Custom 3D Printed Multimodality Imaging Phantoms*. Med Phys, 2015. **42**(10): p. 5913-5918.

30. Solc, J., T. Vrba and L. Burianova, *Tissue-equivalence of 3D-printed Plastics for Medical Phantoms in Radiology*. J Instrumentation, 2018. **13**: P09018

31. Tino, R., A. Yeo, M. Leary, M. Brandt and T. Kron, *A Systematic Review on 3D-Printed Imaging and Dosimetry Phantoms in Radiation Therapy*. Technol Cancer Res Treat, 2019. **18**: 1533033819870208

32. Dancewicz, O.L., S.R. Sylvander, T.S. Markwell, S.B. Crowe and J.V. Trapp, *Radiological Properties of 3D Printed Materials on Kilovoltage and Megavoltage Photon Beams*. Phys Med, 2017. **38**: p. 111-118.

33. Arconada-Alvarez, S.J., J.E. Lemaster, J. Wang and J.V. Jokerst, *The Development and Characterization of a Novel Yet Simple 3D Printed Tool to Facilitate Phantom Imaging of Photoacoustic Contrast Agents*. Photoacoustics, 2017. **5**: p. 17-24.

34. Negus, I.S., R.B. Holmes, K.C. Jordan, D.A. Nash, G.C. Thorne and M. Saunders, *Technical Note: Development of a 3D Printed Subresolution Sandwich Phantom for Validation of Brain SPECT Analysis*. Med Phys, 2016. **43**(9): p. 5020-5027.

35. Bohndiek, S., S. Bodapati, D. Van de Sompel, S.R. Kothapalli and S. Gambhir, *Development and Application of Stable Phantoms for the Evaluation of Photoacoustic Imaging Instruments*. PLoS One, 2013. **8**(9): e75533

36. Wady, P., A. Wasilewski, L. Brock, R. Edge, A. Baidak, C. Mcbride, L. Leay, A. Griffiths and C. Valles, *Effect of Ionizing Radiation on the Mechanical and Structural Properties of 3D Printed Plastics.* Additive Manufacturing, 2020. **31**: Article 100907

37. Caldwell, J., R. Lehner, S. Balog, C. Rheme, X. Gao, D. Septiadi, C. Weder, A. Petri-Fink and B. Rothen-Rutishauser, *Fluorescent Plastic Nanoparticles to Track Their Interaction and Fate in Physiological Environments.* Envir Sci: Nano, 2021. **8**: p. 502-513.

38. Langhals, H., D. Zgela and T. Schlücker, *Improved High Performance Recycling of Polymers by Means of Bi-Exponential Analysis of Their Fluorescence Lifetimes.* Green and Sustainable Chemistry, 2015. **5**: p. 92-100.

39. PVB 1,75mm Natural 0,5kg. Rosa Filaments, 6 Oct. 2022, sklep.rosa3d.pl/product/pvb-175mm-natural-05kg/?lang=en.

40. *Heat Deflection Temperature of Plastics – Plastics and Elastomers from Omnexus*. Available from omnexus.specialchem.com/polymer-properties/properties/hdt-0-46-mpa-67-psi.

41. T-Glase Spec. TAULMAN3D, taulman3d.com/t-glase-spec.html.

42. Standard - Formlabs. Formlabs Material Data Sheet, Apr. 2017, formlabs-media.formlabs.com/datasheets/Standard-DataSheet.pdf.

43. Engineered Materials - Jabil. Jabil TPU Overview, www.jabil.com/dam/jcr:3523dbd7-fb6a-46af-8959-d57a2fca3f22/jabil-tpu-90a-one-sheet.pdf.

44. Somos Watershed 11122. Proto3000, 21 July 2022, proto3000.com/materials/somos-watershed-11122/.

45. Vero for Stratasys J55. Stratasys, 2020, www.stratasys.com/siteassets/materials/materials-catalog/polyjet-materials/verovivid/mds_pj_vero_for_j55_0320a.pdf.

46. Knight, J.T., A.A. El-Sisi, A.H. Elbelbisi, M. Newberry and H.A. Salim, *Mechanical Behavior of Laminated Glass Polymer Interlayer Subjected to Environmental Effects*. Polymers, 2022. **14**(23): p. 5113

47. *Water Absorption 24 hours – Plastics and Elastomers from Omnexus*. Available from omnexus.specialchem.com/polymer-properties/properties/water-absorption-24-hours.

48. Atiqah, A., M. Jawaid, M.R. Ishak and S.M. Sapuan, *Moisture Absorption and Thickness Swelling Behaviour of Sugar Palm Fibre Reinforced Thermoplastic Polyurethane*. Procedia Engineering, 2017. **184**: p. 581-586.

49. Khalili, P., X. Liu, Z. Zhao and B. Blinzler, *Fully Biodegradable Composites: Thermal, Flammability, Moisture Absorption and Mechanical Properties of Natural Fibre-Reinforced Composites with Nano-Hydroxyapatite*. Materials, 2019. **12**(7): p. 1145.

50. Somos Watershed XC 11122. Javelin 3D Solutions, 13 Apr. 2023, www.javelin-tech.com/3d/stratasys-materials/somos-watershed-xc-11122/.

51. Stratasys: 3D Printing & Additive Manufacturing | Stratasys. PolyJet Systems and Materials, www.stratasys.com/siteassets/polyjet-systems/brpjsystemsmaterialsoverviewa41121a.pdf?v=48f2de

52. *Strength at Break (Tensile) – Plastics and Elastomers from Omnexus*. Available at omnexus.specialchem.com/polymer-properties/properties/strength-at-break-tensile.

53. Tango. A Soft Flexible 3D Printing Material, www.stratasys.com/en/materials/materials-catalog/polyjet-materials/tango/.

54. Agilus30 - Forerunner 3D Printing. Stratasys - Spec Sheet, forerunner3d.com/wp-content/uploads/2020/01/Agilus-30-Spec-Sheet.pdf.

55. Behniafar, H. and S. Azadeh, *Transparent And Flexible Films of Thermoplastic Polyurethanes Incorporated By Nano-SiO_2 Modified With 4,4'-Methylene Diphenyl Diisocyanate.* International Journal of Polymeric Materials and Polymeric Biomaterials, 2015. **64**(1): p. 1-6.

56. Dean, R.B. and W. Dixon, *Simplified Statistics for Small Numbers of Observations*. Anal Chem, 1951. **23**(4): p. 636-638.

57. Garner, J.S. and M.S. Favero, *CDC Guideline for Handwashing and Hospital Environmental Control, 1985*. Infect Control, 1986. **7**(4): p. 231-243.

58. Zaidi, M., M. Angulo and J. Sifuentes-Osornio, *Disinfection and Sterilization Practices in Mexico*. J Hosp Infect, 1995. **31**(1): p. 25-32.

59. Crameri, F., G.E. Shepard and P.J. Heron, *The Misuse of Colour in Science Communication.* Nat Commun, 2020. **11**: p. 5444.

60. *Preclinical Imaging Market Size, Share & Trends Analysis Report by Product (CT, MRI, PET/SPECT, Multi-Modal, Optical, Ultrasound, Photoacoustic (PAT), Reagents, Services), by Application, by End-Use, by Region, and Segment Forecasts*. 2022 - 2030. Available from: https://www.grandviewresearch.com/industry-analysis/preclinical-imaging-market.

61. Lev, M.H. and S.J. Nichols, *CT Angiography and CT Perfusion Imaging*. Brain Mapping: The Methods, 2002. p. 427-484.

Interchangeable multi-rodent holders

For high-throughput imaging

From the lab of Kurt Zinn
Professor Radiology, Biomedical Engineering,
and Small Animal Clinical Sciences
Michigan State University

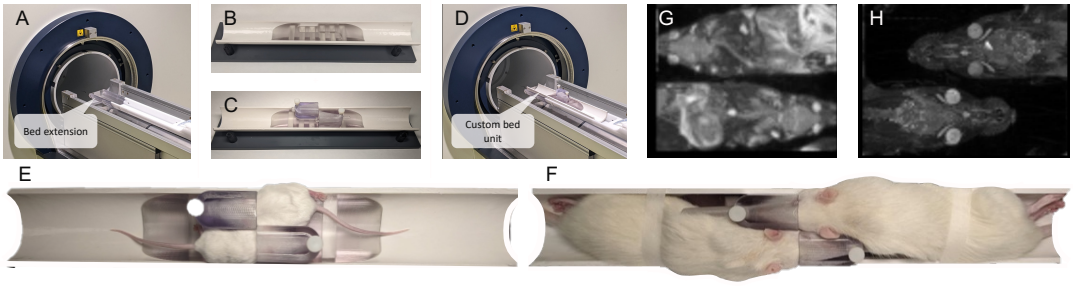

Figure 1. Interchangeable rodent holders and their use. The custom bed units and bed extension are shown installed on the Bruker BioSpin 70/30 MRI with PET insert in images A-D. A set of mice and rats are shown loaded in the custom bed unit in images E and F. Maximum intensity projections of MRI scans are given for each species in G and H as acquired by the Bruker BioSpin 70/30 to illustrate field of view.

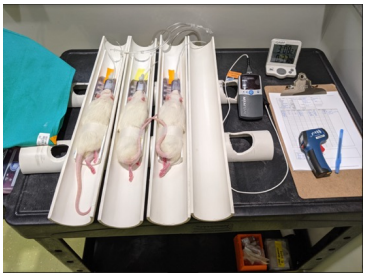

Figure 2. Staging area for custom bed units. One rat is loaded in each of 3 custom bed units as an example. The system can be scaled up as needed.

A new way to image

Our product is an imaging accessory that facilitates high-throughput rodent imaging using low-cost materials. This design is built to be compatible with various scanners and supports long-term imaging experiments. The product has 2 components: a modular set of 2-rodent custom bed units (Figure 1) and a corresponding staging area (Figure 2).

Instrument benefits

- Image a greater number of animals in a day
- Elimination of initial staging process
- Imaging time and cost cut in half or more
- Reduced variability in image analysis
- Does not require modifications to instrument

Instrument highlights

The imaging beds enable the animals to remain anesthetized and stationary while the custom bed unit is exchanged in and out of the imaging instrument for efficient data collection. Because the animals remain stationary, their positioning is reproducible between scans which greatly reduces technologist effort and opportunity for error. Animals rest in the staging area between imaging time points, where their body temperature is maintained, and their oxygen saturation and respiration rate can be monitored. Imaging beds are applicable for MR, PET, and PET/MRI instruments, with plans to expand to CT as well.

Contact Mitchell Gabalski ( ) or Kylie Smith ( ) for more information.

Figure 3.8. Flyer sent with informational interview requests.

Initial testing of the updated custom bed unit design is described here. The Technology Transfer Office at Michigan State University is currently evaluating the updated design as potential intellectual property, so it is not shown. Like the initial design, this iteration was 3D printed from VeroClear on a J750 Stratasys printer.

Detection sensitivity was screened using the same imaging methods described in section 2.2.2.2. Additionally, plastic tubes ("PCR tubes" in Figure 3.9) filled with 50 μL of 2-deoxy-2-[F-18]-fluorosorbitol (F-18-FDS, reduction product of F-18-FDG) were lined along the center of the bed with 1 inch of separation (n=6). Images were acquired on the 7T Bruker BioSpec 70/30 with PET insert and processed as previously described. Instead of recovery coefficient, detection efficiency was calculated as ((total activity in PET volume of interest)/(known activity))*100. Spillover to the subject was detected at a lower rate than in the previous design (Figure 2.2), and the spatial resolution and recovery percentage range were comparable (Figure 3.9).

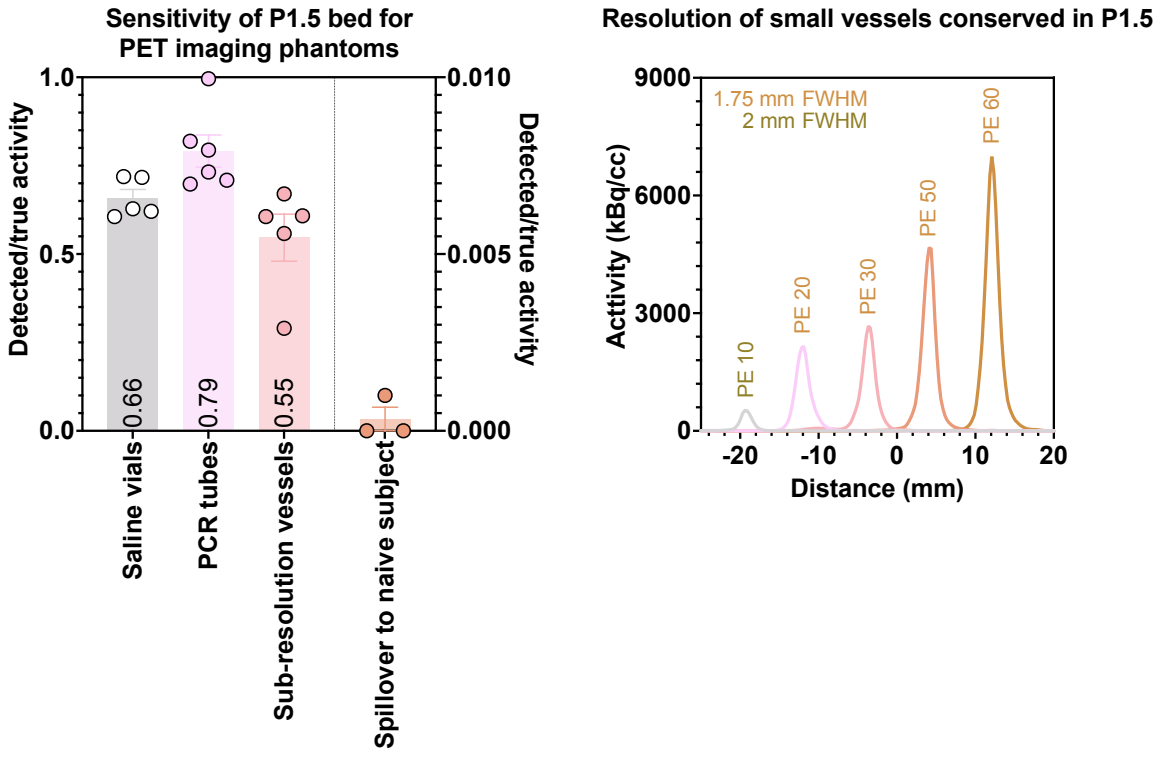

Figure 3.9. Initial evaluations for PET imaging performance using the updated bed for the high throughput imaging system (P1.5). Recovery efficiency is shown on the left and spatial resolution is described on the left.

The new bed was tested in a longitudinal imaging experiment. Two rat cohorts (Cohort 1 - Subject set 1 and 2, Cohort 2 - Subject set 3 and 4) were imaged by simultaneous PET/MR following injections. Subjects received an injection of PET agent alone or a mixed injection with both PET and MR imaging agents present. Cohort 1 was imaged from 0-3 hours post-injection and cohort 2 from 4-8 hours post-injection per the schedule shown in Figure 3.10. A rectal thermometer was used to monitor the body temperature of one rat from each subject set during imaging, while a respiration monitor was used to measure breathing rate (Figure 3.11). Opportunities to improve the anesthesia system were identified. The same vaporizer was used to supply inhalant anesthesia (isoflurane) to the MRI and staging area, which made it difficult to maintain respiration rates at the same level for male and female rats. Additionally, differences in the breathing rate between members of a subject sets were observed by eye. These concerns will be a focus for future iterations.

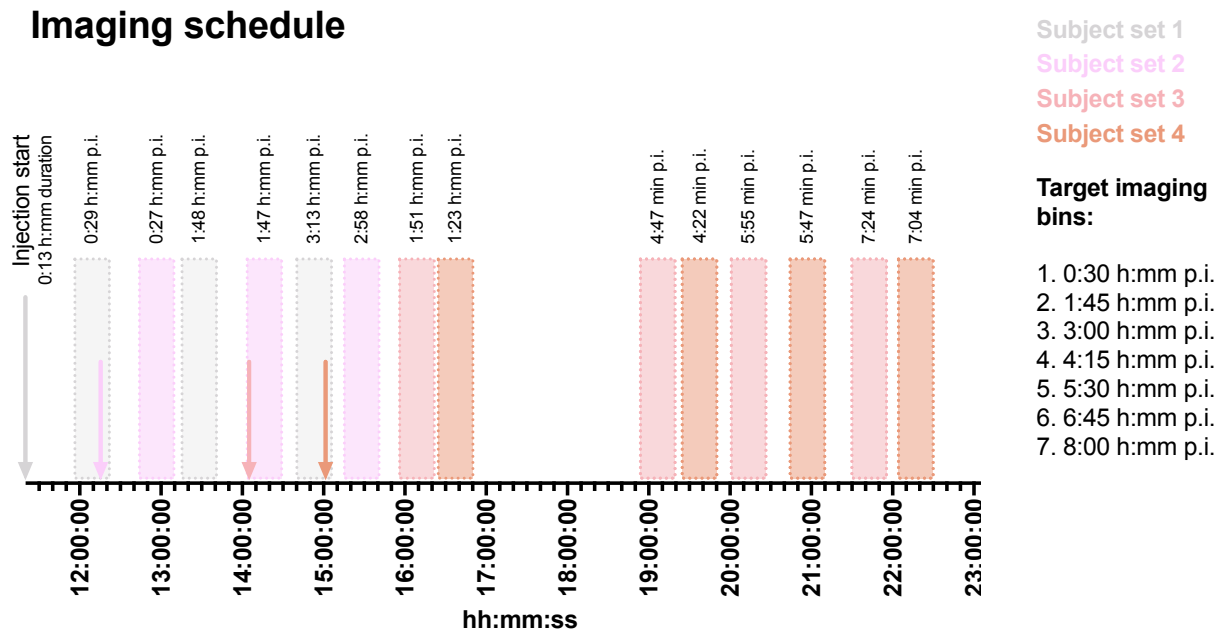

Figure 3.10. Imaging schedule used in initial evaluations of the updated bed design for longitudinal imaging. Military time is given along the x-axis. H:mm p.i. = hours:minutes post-injection.

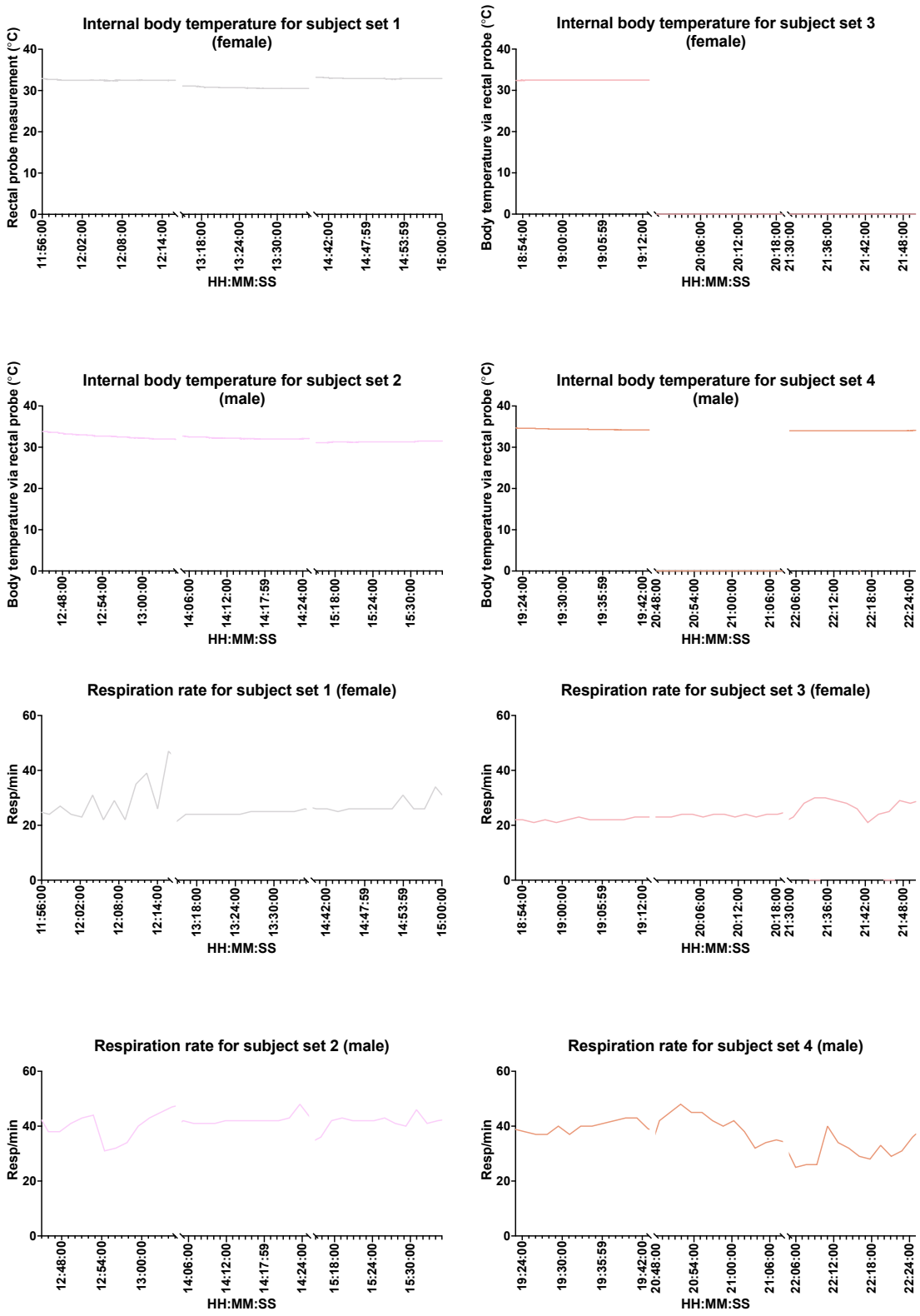

Figure 3.11. Body temperature (top) and breathing rate (bottom) for individuals during their imaging session. Military time is given along the x-axis. Gaps in the body temperature graphs are due to reading errors in the temperature probe.

CHAPTER 4: DE-RISKING NOSE TO BRAIN NEUROIMAGING BY PET

4.1 Background

Efficient specific delivery of drugs to the central nervous system (CNS) is an ongoing challenge in biomedical science. Traditionally, drugs have been delivered to the brain via oral, transdermal, or intravenous administration[66]. Although these methods are useful due to ease of dosing, their efficacy is limited due their reliance on systemic absorption for delivery to the brain. Systemic drug delivery is challenged by first-pass metabolism, limited passage through the blood-brain barrier (BBB), and off-target interactions. Invasive injections directly into the CNS such as intrathecal, intracerebral, and intracisternal injections can overcome these limitations for patients who cannot tolerate or do not see efficacy from traditionally delivered therapeutics[67]. Yet, these invasive protocols are not ideal for routine practice. A non-invasive method for specific, direct delivery to the brain would be highly advantageous.

Nose to brain (N2B) delivery has been advocated as a noninvasive method for direct delivery to the brain. Direct N2B transfer is achieved when drugs or other materials are deposited at nasal epithelium innervated with trigeminal or olfactory nerves[68-72]. The primary site of interest for N2B delivery is the olfactory epithelium (OE), a mucosa densely innervated with olfactory neurons that project directly to the olfactory bulb (OB). Small, lipophilic molecules deposited on the olfactory epithelium (OE) diffuse through the mucosa into channels surrounding olfactory sensory neurons (OSNs). The fluid filling these channels is continuous with the cerebrospinal fluid (CSF) that engulfs the brain, which helps to distribute drugs to other brain regions by bulk CSF flow[69,70] or glymphatic distribution[71-73]. Since N2B does not rely on systemic distribution, nasal delivered material bypasses the BBB and avoids hepatic metabolism. This approach has been used to successfully deliver drugs[74-76], viruses[72,77], nanocarriers[78-80], and peptides[68,72,76,81] to the CNS. Plasma sampling[82-84], CSF sampling[51], or changes in cognitive[85] or behavioral[74,86,87] outcomes have been used to evaluate the efficacy of N2B treatments, leading into FDA approvals for intranasal insulin[52], esketamine[88], and naloxone[89] in recent years.

Despite the optimism of successful pre-clinical N2B delivery[78], translation to successful clinical N2B delivery faces a number of potential challenges. For example, successful delivery with one device may not translate to success in another device. This was highlighted in a recent clinical trial in which a N2B insulin protocol validated in prior studies[81,85] (using the Kurve ViaNase device)

failed to be efficacious when applied in a second device (Impel Neuropharma POD device)[51]. This can be particularly challenging in an expanding area of device development with a wide range of device costs, where a single N2B specific device (e.g. Kurve ViaNase[90], Impel NeuroPharma Precision Olfactory Delivery Device[51], OptiNose Bi-directional Delivery Device[91]) can cost tens of thousands of dollars per unit. Techniques that allow us to screen delivery devices and protocols could enable more successful N2B delivery (device performance, delivery conditions, formulation characteristics, etc.) in a timely and cost-effective manner and thus reduce the time for translation for N2B therapeutics.

The current study utilized IRDye800- or F-18-labeled molecules to follow aerosol deposition in nasal cavity models. We opted to modify and customize vibrating mesh nebulizers, which are commercially available, low cost (~$200), and can be optimized for aerosol delivery to the nasal cavity[92,93]. Nebulizers of interest were adapted with 3D-printed covers and tested in simulated N2B delivery models to prepare for in vivo imaging studies. IRdye800-insulin was used to qualitatively validate deposition in model nasal regions of interest for a cross-sectional phantom before progressing to F-18 for sensitive detection in more complex models. F-18 is a positron-emitting radionuclide that can be accurately measured in deep, attenuating structures with high resolution. For that purpose, molecules were radiolabeled with F-18 and imaged with positron emission tomography (PET) to quantify deposition and localization in a CT-derived nonhuman primate (NHP) nasal cavity phantom. The levels of F-18 in all delivery components were carefully measured. Finally, we tested the translation of the approach in a live Rhesus Macaque. Rhesus Macaque's nasal cavity is similar to a human's (large vestibule, simple, < 3 unbranched turbinates) and have a similar airflow pattern during inhalation (airflow through bottom $^2/_3$ of cavity, close to ventral floor[94]), making NHPs an appropriate model for aerosol deposition studies intended for translation.

4.2 Materials and Methods

4.2.1 Model Preparation

4.2.1.1 Custom 3D-printed Nebulizer Accessories and Delivery Apparatus

Three commercial vibrating mesh nebulizers were selected for modification, namely the Aura (Aura Medical, New York, United States), Flyp (Convexity Scientific Inc., Connecticut, United States), and Omron MicroAir (Omron, Kyoto, Japan) nebulizers. PET was intended to determine

where aerosol was deposited in the models, and therefore a safe way to deliver radioactive aerosol was required. To this end, custom fitted nebulizer covers were designed based on the original mouthpiece/cover for each device in Autodesk Inventor software (San Rafael, California, United States) to keep the aerosol completely enclosed. The covers were 3D printed on a J750 PolyJet 3D-Printer (Stratasys, Rehovot, Israel) from VeroClear material aside from the cover-device interface, at which we included a blend of VeroClear and Shore70 material to improve the seal between them. Support material was removed by hand or via Balco WaterJet (Stratasys, Rehovot, Israel).

4.2.1.2 2-Compartment Cavity

A two-compartment cavity was constructed to test the aerosol output of our 3D cover-fitted nebulizers in a semi-sealed aerosol delivery system. The box (5.5 x 5 x 5 cm) was divided into left and right chambers by a “septum”, akin to a nasal cavity. Each chamber had a circular opening. We used a Stratasys J750 to 3D print the phantom using VeroClear material. After printing, support material was manually removed before placing the phantom in an alkaline bath (2% NaOH, 1% Na_2SiO_3 in water) for 10 minutes followed by a brief rinse in de-ionized (DI) H_2O to dissolve remaining support material.

4.2.1.3 Rhesus Macaque Nasal Cavity Phantom

A non-human primate nasal cavity model was generated to investigate aerosol deposition patterns in the nasal cavity. A soft tissue mask was rendered using a head-focused CT scan (CERETOM NL3100, Neurologica, Danvers, Massachusetts, United States) of a 4.7 kg Rhesus Macaque in Materialise Mimics software (Belgium, https://www.materialise.com). The major airways were preserved by thresholding the mask according to the software’s definition of children’s skin. Holes in the mask were filled and unwanted material (e.g., intubation tube) was removed in Meshmixer (San Rafael, California, United States). The Standard Tessellation Language (STL) file was then imported into Autodesk Inventor to reduce the model to only the nares and nasal cavity (6.5 x 3.8 x 3.8 cm). Two copies of the phantom were printed – a two-part model separated at the midline and another cut into cross sections (1 cm thick cross sections, most anterior section 1.5 cm). We printed the phantom out of Shore70 material on the Stratasys J750. Support material was removed using the alkaline bath method described above. The two-part model was combined to be a single unit with a continuous cavity using superglue.

4.2.1.4 Phantom Experiments

4.2.1.4.1 Tracer Preparation

4.2.1.4.1.1 IRdye800-insulin

Insulin was labeled with IRdye800 to qualitatively evaluate aerosol output to a nasal cavity phantom in a semi-sealed aerosol delivery system. To prepare for conjugation, 8 mg human recombinant insulin (Millipore Sigma, Burlington, Massachusetts, United States) was dissolved in 0.1 M HCl and added to sodium phosphate buffer (pH 7.8, 0.15 M) in a 1:2 ratio to reach the desired volume. IRdye800-NHS (0.05 mg; LI-COR Biosciences, Lincoln, Nebraska, United States) was dissolved in a small volume of dimethylformamide (20 mL) and added to the insulin vial. The conjugation mixture incubated at room temperature for 1 hour while rocking. Free dye was removed from the mixture via dialysis purification (3500 MWCO) in phosphate buffered saline (PBS) overnight at 4°C, with a buffer change at 2 hours. The presence of dye inside the dialysis cassette the following day confirmed that remaining dye was conjugated to insulin. An ultraviolet–visible spectrophotometry measured protein concentration and the dye-protein molar ratio for the labeled product using the Bradford Protein Assay (SpectraMax M3, San Jose, California, United States) and A_{280} and A_{max} measurements as used in Beer-Lambert's Law (NanoDrop One, Thermo Fisher, Waltham, Massachusetts, United States), respectively. A_{280} and A_{max} values were 0.071 and 0.135 for the labeled delivery product, indicating that ~1 in 23 insulin molecules were labeled with a fluorophore on average.

4.2.1.4.1.2 F-18-fluoride, F-18-FDG

F-18 is a useful radionuclide due to its low cost, availability, and high spatial resolution using PET scanners. We acquired F-18-fluoride and [F-18]-2-deoxy-fluoroglucose (F-18-FDG) from Cardinal Health (East Lansing, Michigan, United States) to assess aerosol distribution in delivery in the Rhesus Macaque nasal cavity phantom and delivery components. The tracers were unmodified aside from dilution via PBS prior to use.

4.2.1.4.1.3 Deposition Testing

4.2.1.4.1.3.1 2-compartment Cavity

The rate of aerosol production was tested for each device. This an important metric for N2B delivery, as studies show that shorter nebulization times help to minimize the dose lost to mucociliary clearance to the GI tract[91]. We measured the time required to aerosolize DI H_2O by measuring changes in the weight of a filled nebulizer (0.25, 0.5, 1 mL loading volume) while it was operating. Aerosol production rate was tested over three separate days for each nebulizer to verify consistency in performance.

To confirm that 3D cover-fitted nebulizers perform to standard in our semi-sealed aerosol delivery system, we delivered aerosolized IRdye800-insulin to the two-chambered cavity and followed with fluorescence imaging to evaluate delivery. IRdye800-insulin (450 mL loading volume) aerosol was delivered via tubing directly from the nebulizer cover to the left opening of the two-compartment cavity. Medical grade compressed air was used to carry aerosol towards the box at 0.1 liters per minute (LPM). Following delivery (5 minutes), each face of the box was imaged via 800 nm laser on the Pearl Trilogy Small Animal Imaging System (LI-COR Biosciences, Lincoln, Nebraska, United States). Positioning and imaging properties were maintained for all images. Semi-quantitative analysis of deposition was performed by drawing a region of interest (ROI) around the box face closest to the camera and summing the signal for each face in LI-COR Biosciences's Image Studio Software.

4.2.1.4.1.3.2 Rhesus Macaque Nasal Cavity Phantom

After demonstrating that dye-labeled molecules could be successfully deposited as aerosol via our delivery apparatus, the next step was to predict what fraction and in what pattern aerosol would be deposited in the Rhesus Macaque nasal cavity. We used IRdye800-insulin to validate protein deposition in nasal cavity regions of interest before progressing to the use of radiotracer to sensitively quantify the levels deposition in the phantom. IRdye800-insulin (120 mg/mL, 450 mL) was loaded into the Omron nebulizer medicine cup as solution and administered to the cross-sectioned phantom as aerosol. Following 5 minutes of aerosol delivery at varying flow rates, the cross-section model was disassembled, and each component was imaged on the Pearl Trilogy Small Animal Imaging System. Positioning and imaging properties were maintained for all images.

The carrier gas flow rate which resulted in the greatest ratio of fluorescence in the upper nasal cavity/lower or anterior nasal cavity was selected for the radiotracer experiments (data not shown).

Next, we used F-18-labeled radiotracers (n=2 F-18-Fluoride, n=2 F-18-FDG) to sensitively quantify and characterize aerosol deposition from our apparatus in our Rhesus Macaque nasal cavity phantom (Figure 4.1). Physiological conditions were simulated in the phantom by coating the interior passages with silicone oil (Sigma-Aldrich, St. Louis, Missouri, United States), as is standard practice for aerosol deposition studies. Prior to dosing, a μCT (Quantum GX,

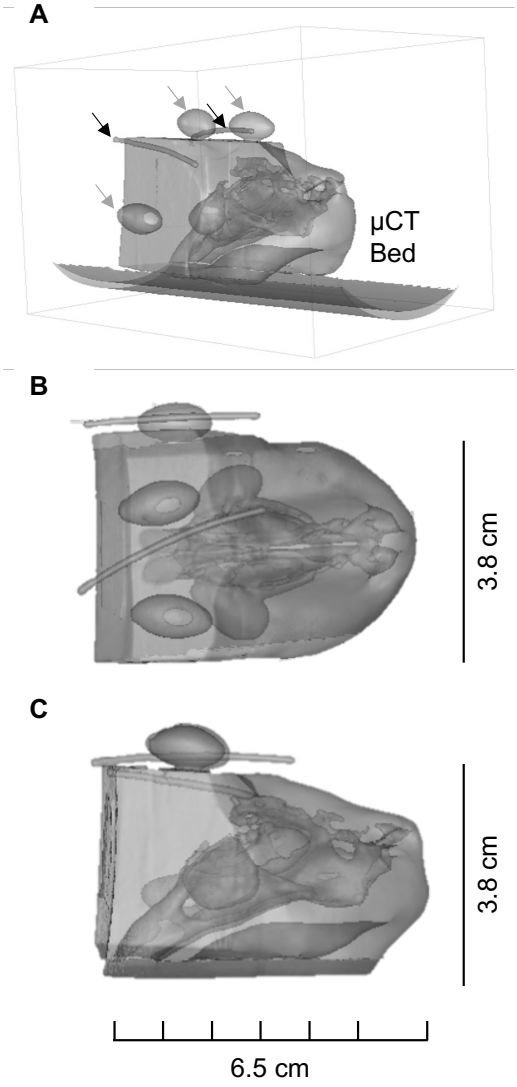

Figure 4.1. 3D-printed phantom of Rhesus Macaque nasal cavity. The phantom was designed using a CT scan of a Rhesus Macaque and printed using a Stratasys J750 PolyJet 3D-Printer. A. View of phantom on μCT bed, with fiducial markers identified with arrows (capsules in gray, point sources in black). B. Axial view of phantom. C. Sagittal view of phantom.

PerkinElmer, Waltham, Massachusetts, United States) was used to confirm that passages were open and clear of obstruction by the silicone oil. Mixed VivoTrax (Magnetic Insight, Alameda, California, United States) and tracer were loaded into PE-60 tubing, sealed with hematocrit sealant, and taped to the phantom as fiducials.

The delivery apparatus, utilizing the Omron nebulizer, delivered 408 MBq F-18-fluoride or F-18-FDG (450 mL) as aerosol inside of a glove box with 0.1 LPM airflow to the left nare of a supine-positioned nasal cavity phantom for 5 minutes (Figure 4.2). During dosing, the door to the glove box (similar to a screw-on lid) was slightly loosened and a 40 LPM vacuum was attached to the glove box gas port to direct residual aerosol to a gas drying column for capture (filled 1:3 activated charcoal to desiccant). Immediately afterwards, the dosing apparatus was disassembled, and deposited activity was measured via dose calibrator (Capintec, Inc., West Sussex, United Kingdom) for each component. For nebulizer cover quantification, activity was estimated via dose calibrator and corrected using a PET-derived calibration curve due to geometric restrictions. A 15-minute PET scan was acquired of the nasal cavity phantom using a 7T Bruker BioSpec 70/30 MRI with PET insert (Bruker, Billerica, MA, USA). After the phantom decayed, it was imaged again via CT to include the fiducials for registration and analysis.

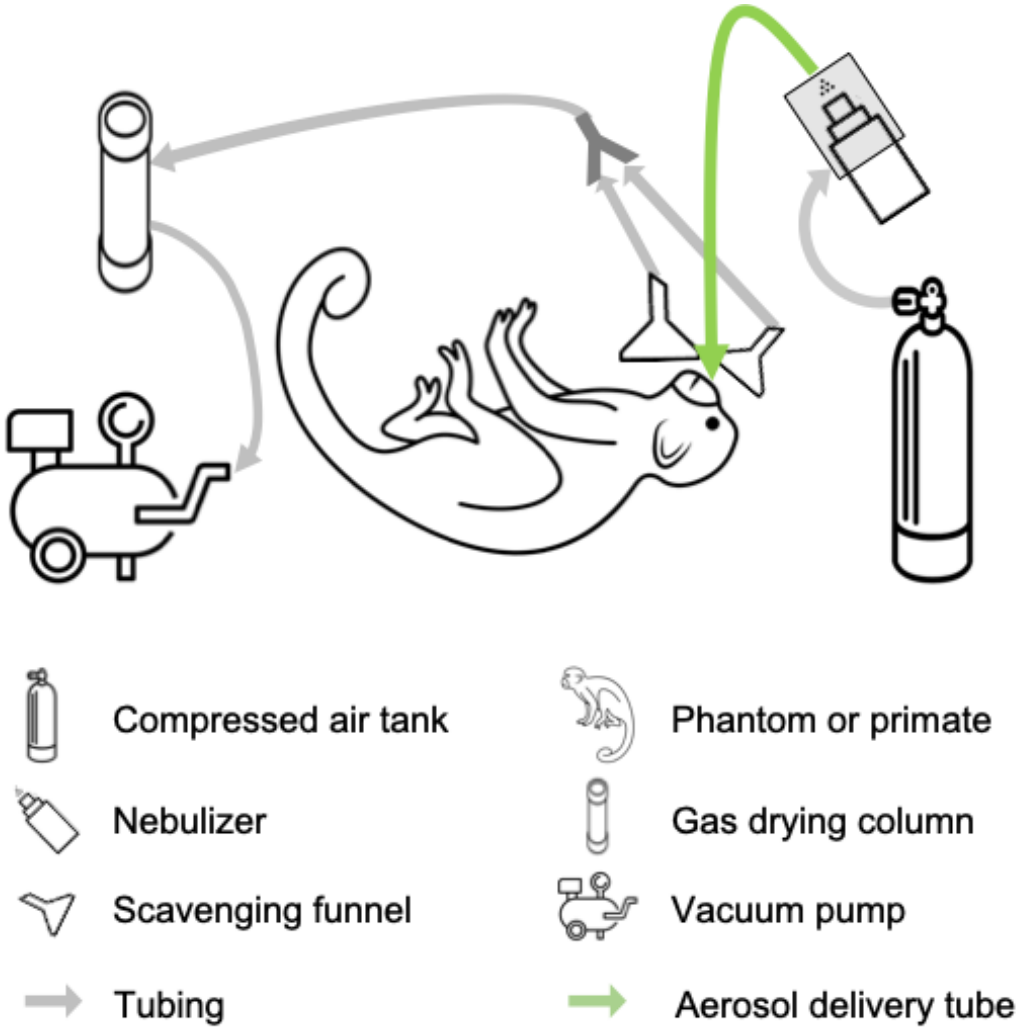

Figure 4.2. Administration set-up for nose-to-brain (N2B) aerosol delivery. For radiolabeled materials, delivery was performed inside of a glove box placed in a fume hood for an additional layer of aerosol containment. Aerosol was administered at 0.1 liters per minute airflow from a compressed air tank. Tracer which leaks from the phantom or dosing components post-dose are scavenged by a 40 liter per minute vacuum at the glove box air port and funnels.

PET data was reconstructed via Maximum-Likelihood Expectation-Maximization (MLEM) algorithm at 0.75 mm voxel size with 12 iterations. Corrections for dead-time, scatter, randoms, and decay correction were performed. Tracer deposition was analyzed in PMOD 4.2 (PMOD Technologies LLC, Zürich, Switzerland) as percent of the loaded dose for the phantom and delivery components. The boundaries of the olfactory epithelium are still debated; therefore, the upper nasal cavity was used as a surrogate for the OE as is standard in gamma scintigraphy literature[93]. The volume of interest (VOI) for OE analysis is given as percent of dose deposited in the phantom and included the dorsal meatus, lateral wall of the middle turbinate, and $^{1}/_{5}$ of the dorsal septum[95,96].

4.2.2 Primate Experiment

Primate studies, including F-18-FB-insulin synthesis, were conducted at Charles River Laboratories in Mattawan, Michigan. Volume of interest analyses were by inviCRO (Boston, Massachusetts, United States).

4.2.2.1 Tracer Preparation - F-18-FB-insulin

A^1,B^{29}-di(*tert*-butyloxycarbonyl)insulin (DBI) was prepared using human recombinant insulin (Millipore Sigma, Burlington, Massachusetts, United States) to protect nucleophilic $GlyA^1$ and $LysB^{29}$ amino groups and facilitate functional group binding to the B-chain's N-terminus phenylalanine using previously published methods[97-99]. This approach conserves binding affinity for the insulin receptor. DBI was purified using semipreparative high performance liquid chromatography (HPLC, Agilent 1260 infinity II, Agilent, Santa Clara, California, United States), desalted via size exclusion chromatography (SEC), and lyophilized for travel to Charles River Laboratories (Mattawan, Michigan, United States).

F-18-fluoride was produced on-site via the $^{18}O(p,n)^{18}F$ nuclear reaction at the Charles River Laboratory cyclotron (Mattawan, Michigan, United States). F-18-fluoride was eluted via tetrabutylammonium mesylate (1 mL, 0.03 M in anhydrous methanol) and dried (70°C and a stream of nitrogen for 5 min, followed by heating to 100°C under vacuum for 10 minutes, thencool to 50°C) before adding a mixture of 4-(ethoxycarbonyl)-*N*,*N*,*N*-trimethylbenzenaminium triflate in anhydrous dimethylsulfoxide (4.5-5.5 mg/500 µL solution) and heating for 10 minutes at 90°C. Tetrapropyl ammonium hydroxide in acetonitrile (0.52 mL, 0.04 M) was added to the cooled (40°C) solution and then heated (120°C for 6 minutes, cooled to 50°C) before adding *N*,*N*,*N'*,*N'*-Tetramethyl-*O*-(-*N*-succinimidyl)uronium tetrafluoroborate (TSTU, 9-11 mg) in anhydrous acetonitrile (0.6 mL) and heating again (70°C for 6 minutes, then 90°C for 5 minutes). The resulting reaction mixture containing F-18-Succinimidyl-fluorobenzoate (F-18-SFB) was purified using semipreparative HPLC and lyophilized prior to quality control testing. Chemical and radiochemical purities/identities were analyzed using an Agilent 1100 HPLC (Agilent, Santa Clara, California, United States) equipped with a radioactivity detector and an ultraviolet (UV) detector. Radiochemical purity for F-18-SFB was typically > 95%, and identity was confirmed by comparing the retention time of the radiolabeled product with that of the corresponding unlabeled reference standard.

F-18-SFB (8140 MBq at start of synthesis) was concentrated by heat (50°C) and a stream of argon for 20 minutes in the Pelltier Reactor. A solution of the DBI product (0.5 mg in 100 µL 0.1 M borate and 100 µL 0.1 M sodium carbonate) was added, heated to 40°C for 30 minutes, and manually agitated (at 0 and 15 minutes). Next, the reaction mixture was treated with trifluoroacetic acid (in 100 µL DI water) and stirred at 25°C for 5 minutes before use of semi-preparative HPLC for purification (Agilent Zorbax SB-CN, 5 µm, 9.4 x 250 mm, eluted with 90:10:0.1 Water:Ethanol:Formic Acid at a flow rate of 5 mL/min). The purified F-18-FB-Insulin (retention time ~13 minutes) was then trapped on a pre-conditioned (6 mL each ethanol then water) Waters tC18 Short Plus cartridge, followed by elution with ethanol (0.4 mL), then x1 PBS (pH 8.0, 1.2 mL) into the mixing vial. The F-18-FB-insulin formulation was transferred to a sterile dose vial, and an aliquot was submitted for quality control testing. Chemical and radiochemical purities/identities were analyzed using high performance liquid chromatography (HPLC) on an Agilent 1100 HPLC equipped with a radioactivity detector and an ultraviolet (UV) detector. Radiochemical purity of F-18-FB-insulin was > 99% (Table 5.2 in Appendix B), and identity was confirmed by comparing the retention time of the radiolabeled product with that of the corresponding unlabeled reference standard. For dosing, the product was diluted with saline to reach the desired volume with < 10%, w:W ethanol.

4.2.2.2 Deposition Test - Live Rhesus Macaque

Delivery to the olfactory epithelium using the Omron nebulizer with our delivery apparatus was tested in a nonhuman primate (NHP). The NHP experiment was conducted at Charles River Laboratories (Mattawan, Michigan, United States) with approval from the Institutional Animal Care and Use Committee (IACUC). The animal was given a loading dose of anesthesia (10 mg/kg intramuscular ketamine) to prepare for the procedure and maintained under isoflurane to effect. The primate was also intubated to minimize complications with ventilation and laid supine in a PET scanner bed that had been transferred to a table in the adjacent room. The apparatus described in Figure 4.3 was used to deliver 450 mL of F-18-FB-insulin at 111.74 MBq (3.02 mCi, 2.37 TBq/mmol at the end of synthesis) to the left nare (5-minute delivery duration) as aerosol at 0.1 LPM airflow. A 40 LPM vacuum was used to scavenge escaped aerosol from the primate's nares and mouth during dosing and direct it to a gas drying column for capture (filled 1:3 activated charcoal to desiccant). Immediately following dosing on the table, the primate was transferred to a MicroPET Focus220 scanner (Concorde Microsystems, Knoxville, Tennessee, United States) for a 120-minute head-focused PET and subsequent computed tomography (CT) scan

(CERETOM NL3100, Neurologica, Danvers, Massachusetts, United States). The delivery apparatus was disassembled and deposition on each component was quantified via dose calibrator (ATOMLAB 100Plus, Biodex Medical Systems, Shirley, New York, United States) or PET (MicroPET Focus120 scanner for nebulizer cover, gas drying chamber, Concorde Microsystems, Knoxville, Tennessee, United States). PET scans were reconstructed via 3D ordered subset expectation maximization algorithm (OSEM 3D/MAP) with global deadtime correction, scatter correction, and CT-based attenuation correction. Quantification of tracer deposition in the nasal cavity and brain were performed using VivoQuant Software (inviCRO) after PET and CT images were co-registered and resampled to uniform voxel size (0.6 mm^3). The nasal deposition VOI was segmented via thresholding while the brain VOI utilized a whole brain 3D monkey atlas provided by inviCRO. Percent of the loaded dose was calculated for both volumes of interest. For analyses of deposition in the OE, PET and CT images were loaded into PMOD 4.2 for co-registration and resampling to uniform voxel size (0.6 mm^3). OE boundaries were manually drawn as described previously and deposition was calculated as the percent of the deposited dose.

4.3 Results

4.3.1 Evaluation of Nebulizers

Device reliability was evaluated for three devices of interest (Aura, Flyp, and Omron MicroAir) by testing aerosol production rate over several consecutive days. Device performance was also evaluated for 3 small dosing volumes, as the nebulizers tested are intended for treatments 5-10 mL. The rate of aerosol production was highest for the Omron MicroAir, nearly double the aerosol production rate of the other nebulizers (Figure 4.3A). Loading volume did not impact Omron performance, but consistency did wane as determined by Tukey's Test for Nonadditivity ($F_{Volume, Omron}$=0.45, $F_{Day, Omron}$=54.38, $F_{0.05}$=10.13). The Aura produced aerosol at a slower rate than the Omron but was not influenced by the loading volume and saw no change in consistency over 3 days ($F_{Volume, Aura}$=3.24, $F_{Day, Aura}$=0.84). Unlike its competitors, Flyp's aerosol production rate was impacted by the loading volume and day of use ($F_{Volume, Flyp}$=5.62, $F_{Day, Flyp}$=48.23) and had the lowest output of the three. Solution pooled atop the vibrating mesh plate which suspended aerosol production for each nebulizer tested. This required manual intervention to clear the plate and resume delivery.

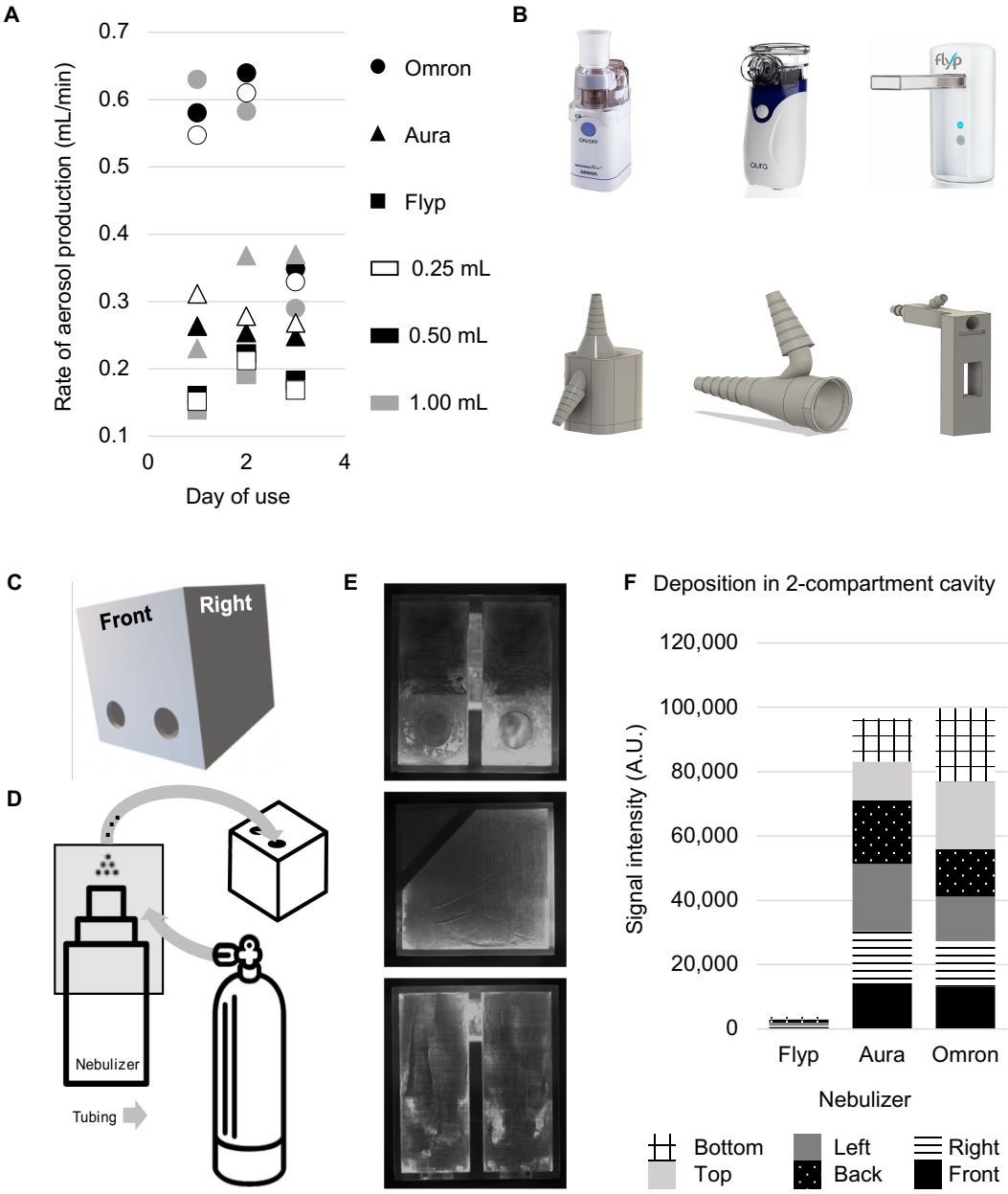

Figure 4.3. Evaluation of nebulizer performance with custom 3D-printed covers. A. Consistency of aerosol production rate was tested across three days for each device. B. Custom-fitted covers were 3D printed for each nebulizer to contain fluorophore- or radiotracer-labeled molecules within the administration system. Nebulizers are shown in the left column with the respective cover to their right. C. System efficacy was evaluated for each nebulizer-cover pair by quantifying the output of aerosolized IRdye800-insulin into a 3D-printed two-compartment cavity. D. Schematic for system testing with two-compartment cavity. E. Example of deposition imaging for IRdye800-insulin on three sides of the two-compartment cavity as output by the Omron MicroAir. F. Comparison of output in two-compartment cavity by each nebulizer shows that the Omron deposited the greatest amount of material, followed closely by the Aura nebulizer.

A custom-fitted cover was successfully made for each nebulizer based on the accessories that came with the device. Generated aerosol was dispersed and maintained in-line with the aerosol output stream to minimize impaction in small-volume radiotracer studies. The Aura and Flyp nebulizers generated aerosol from the front face of the device as opposed to the Omron, which emitted aerosol from the top. This resulted in top heavy, sometimes unstable devices which required additional support. The cover-fitted Omron nebulizer was stable on its own, although it was advantageous to tilt the device at a 50° angle from the floor to maintain a steady aerosol stream and reduce residual dose loss to back-flow in the medicine cup. Further, we faced additional challenges with forming a seal around the aerosol-generating region of the nebulizer for front-facing styles. Gravity acting on extended regions of the cover introduced gaps at the cover-nebulizer interface that contributed to aerosol leakage.

The modified nebulizers were tested using IRdye800-insulin delivered as aerosol to the two-chambered cavity (Figure 4.3C). Fluorescence imaging showed similar IRdye800-insulin deposition in the cavity for the Aura and Omron devices (0.97:1.00 of maximum deposition), but not for the Flyp (0.04). Further inspection showed that the aerosol was caught in an eddy inside of the delivery chamber of the Flyp's 3D-printed cover and was unable to leave the cover with or without supplied carrier air.

Of the three nebulizers evaluated, the Omron MicroAir performed best for aerosol production rate and aerosol output to a cavity model using our delivery approach. Additionally, challenges with aerosol leakage or clogging of the vibrating mesh plate were least prevalent for the Omron. Although the consistency in device performance waned over the days tested, the reduced rate of aerosol production approximated the other two nebulizers. Therefore, the Omron was selected for further evaluation using the nasal cavity phantom and live rhesus macaque.

4.3.2 F-18-tracer Aerosol Deposition in the Rhesus Macaque Nasal Cavity Phantom

The proportion of tracer deposited in each delivery component was calculated as a percentage of the starting dose (408 MBq). For all F-18-Fluoride and F-18-FDG trials (n=4), the amount in components were as follows: 41.01% ± 22.60 in the nebulizer's medicine reservoir, 8.26% ± 6.09 in delivery tubing, 67.03% ± 56.02 in the nebulizer cover, and 1.09% ± 0.99 in or on the nasal cavity phantom (Figure 4, ± 95% confidence interval). On average, 114.80% ± 78.33 of the starting dose was recovered. For all trials except one, total dose recovered was less than 100% (Figure

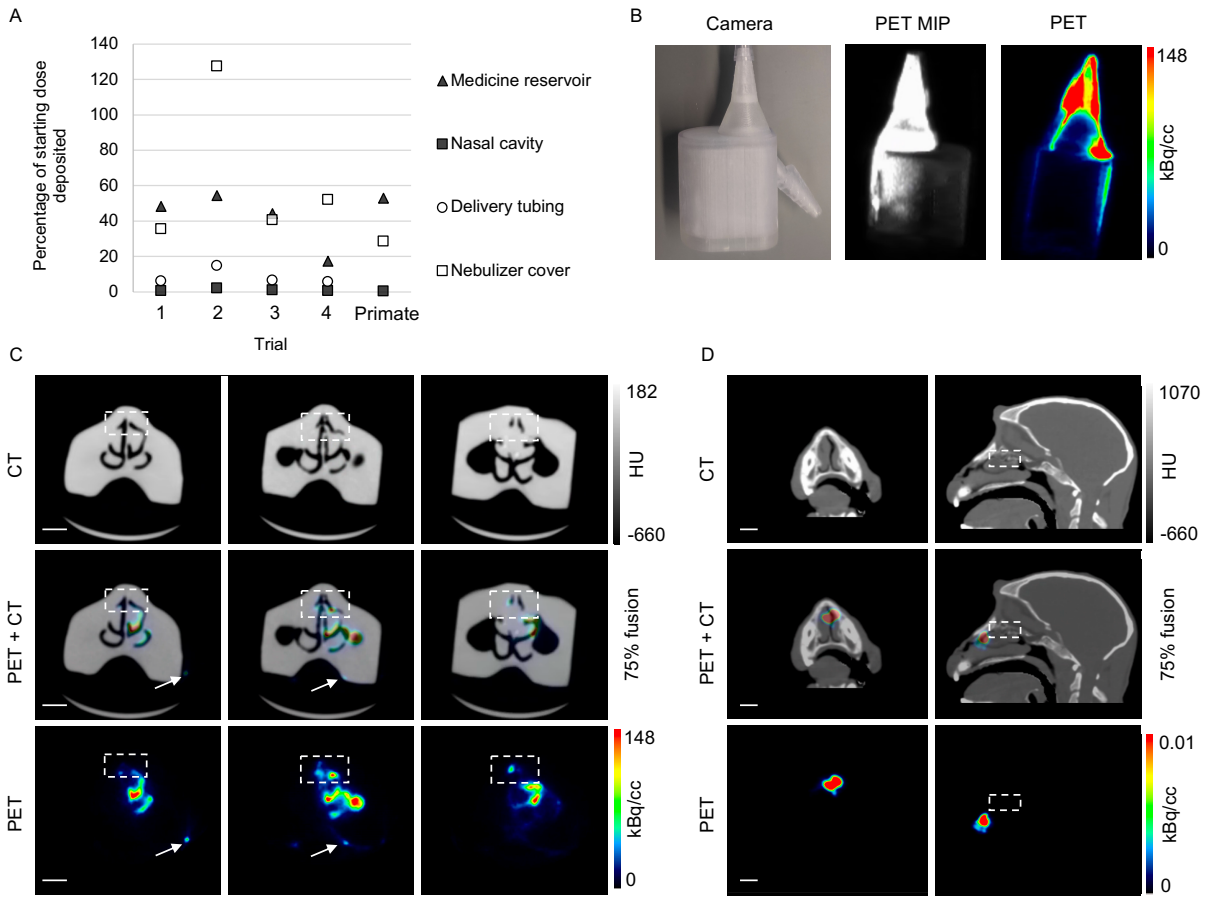

Figure 4.4. Deposition fraction results for F-18-labeled tracers delivered to phantom or primate nasal cavity as aerosol. A. Quantification of the proportion of aerosol deposited on each component of the delivery system for phantom experiments trials (1-4). Note that the sum of each component approximates 100% or less for all trials except #2. Primate results shown for comparison, where dose deposited in the delivery tubing was measured with the medicine reservoir. B. 3D printed nebulizer cover shown in camera image (right) and PET scan following aerosol delivery. Maximum intensity projection shown in middle, with sagittal cross section shown at the right. C. Co-registration of PET and CT images showing F-18-fluoride (color bar) deposited inside the nasal cavity phantom (grayscale). The dotted box highlights the region of interest for olfactory epithelium; arrows indicate contamination. The PET signal is overlaid on CT scan at 75% fusion. Scale bar = 1 cm. D. F-18-FB-insulin deposition (color bar) in live Rhesus Macaque (grayscale). Deposition primarily occurred on the rostral surface of the medial ethmoturbinate. No deposition was found in the olfactory epithelial region, which is highlighted by the dotted box. The PET signal is overlaid on µCT scan at 75% fusion. Scale bar = 1 cm.

4.4A). Contamination on the exterior of the phantom accounted for 54% ± 8 of the phantom deposited doses, primarily observed at the nasopharynx exit and corners of the phantom. Taken together, 0.59% of the starting dose was delivered to the nasal cavity on average. Region of interest analysis revealed that 5% ± 6 of the dose that reaches the phantom nasal cavity is deposited in the olfactory epithelium (representative scan shown in Figure 4.4C). Tracer was detected in the olfactory epithelium for all trials. Tracer deposited outside of the OE can be seen the maxillary sinus and on the medial ethmoturbinate, which projects obstructively into the nasal

atrium. Tracer that was not accounted for via dose calibrator or PET imaging was likely settled inside of the glovebox or became sequestered in the glove box's scavenging unit.

4.3.3 Deposition in Live Rhesus Macaque

Tracer precursor A^1,B^{29}-di(tert-butyloxycarbonyl)insulin (DBI) was prepared in advance of the study to facilitate day-of-experiment synthesis of F-18-FB-insulin, an insulin PET tracer with conserved binding affinity for the insulin receptor[99] (See Supplementary Materials and Methods for details). F-18-FB-insulin aerosol was successfully delivered to a Rhesus Macaque in the amount of 0.28% (peak at 2 minutes) of the loaded dose (111.1 MBq, 3 mCi) using our nebulizer system. Deposition at the olfactory epithelium was estimated to be 0.84×10^{-6} % of the dose deposited in the nasal cavity. Recovered amounts in various dosing components added to 82.9% of the starting dose. Amount in components were as follows: 52.9% in the nebulizer's medicine reservoir and delivery tubing, 28.6% in the nebulizer cover, and 1.1% in the gas drying column. Impaction of aerosol occurred primarily on the most rostral end of the medial ethmoturbinate (Figure 4.4D). Under these conditions, no uptake was detected in the brain over 120 minutes.

4.4 Discussion

This research provides a pathway to screen aerosol delivery devices in preparation for N2B delivery studies. We used translational molecular imaging techniques to identify primary sites of aerosol deposition following delivery with vibrating mesh nebulizers. This work was done as a first step towards establishing an imaging protocol for tracking the fate of N2B delivered molecules in the clinic that may ultimately avoid clinical anomalies and prospective method failures when applied.

Our NHP phantom predicted the primary site of aerosol impaction in the primate. Figure 4.4C shows that the highest concentration of F-18-fluoride aerosol deposited at the medial ethmoturbinate and maxillary sinus. These findings were consistent with the primate imaging results, where F-18-FB-insulin impaction occurred at the rostral end of the medial ethmoturbinate. This is not unsurprising, as this is a site of high particle deposition for both man and primate due to aerodynamics in the nasal cavity[94]. However, the phantom predicted aerosol penetration deeper into the nasal passages, including 5% of the deposited dose in the OE, which was not observed in the primate scan (0.84×10^{-6} % in the OE). Additionally, the proportion of aerosol

deposited in the nose differed between the phantom and subject (0.59% vs 0.28%). One reason for this discrepancy could be the clearance of deposited material to the nasopharynx by mucociliary clearance[95,100] prior to detection, which is reported to occur within the first 15 minutes following deposition[91]. It was not possible to dose the primate while in the scanner, introducing a delay between delivery start and scan start times. It is possible that a proportion of the deposited dose was removed and/or diluted beyond detection in the mucosa before we began collecting data. Aerosol delivery during imaging may be a goal for future studies to improve our understanding of the deposition fraction, subsequent clearance, and how to modulate these factors to work in our favor.

Our decision to use a simplified nasal cavity phantom introduced both benefits and drawbacks. Airway models are generally created using many samples to account for morphological differences between subjects, which can be quite varied for the upper respiratory tract. Our model is based on a single subject, which may limit its predictive power. We reduced the model to include the nares and airways only, which limited us to test approaches that deliver aerosol directly into the nostril as opposed to testing accessories that fit to the head or face. Further, the semi-rigid material (Shore70) used to 3D print the phantom made it difficult to insert or adhere tubes, tips, etc. into the nostril of the phantom where soft tissue would stretch. We did treat the interior of the nasal passages with silicone oil to mimic the nasal cavity mucus layer. However, this is still an oversimplification that reduces the complex physiological environment of the nasal cavity. The nasal cycle, mucociliary clearance, and the pressure differentials inherent to the respiratory tract are absent from this model and will likely impact success in vivo[77].

Reducing dose loss to deposition on the medicine cup or nebulizer cover would be an important improvement for future studies. The nebulizer cover was critical to minimizing contamination and dose loss to the environment. However, the nebulizer cover contributed significantly to dose loss as the delivery component with the largest fraction of deposition. We observed that aerosol in the enclosed space of the cover settled on the cover's interior surface or on the rim of the nebulizer's medicine cup as droplets. Minimizing dose loss is of high importance due to the time and monetary investments required to produce PET tracers, and compounds with the existing challenge of low nasal delivery fractions from nebulizers[91]. Small volume nebulizers may be the preferred route for nuclear imaging techniques to reduce dose loss and improve the amount of material we can deliver to the subject.

If commercially available vibrating mesh nebulizers are of interest, a device which draws solution from the lowest point in the medicine cup may be preferred to other styles. The Omron's vibrating pin, which helps to produce the aerosol, was elevated relative to the rest of the medicine cup. At loading volumes greater than 500 mL, liquid would flow to the back of the reservoir where it became unavailable for use. Still, with all the nebulizers tested, a small amount of the dose was left in the medicine cup and therefore omitted from delivery. This geometry is challenging for quantification of deposited fraction as well. For this study, a single device was used for all trials including the medicine cup. If backflow occurred, the residual dose from one trial could assimilate with the dose in a subsequent trial such that the sum of activity in all delivery components post-dose is larger than the starting dose. It is believed this was the case for trial 2 of 4 (Figure 4.4A), leading to an overestimation of the average recovered dose. Separate nebulizers for each trial (per day) would eliminate this challenge in the future. Options for reducing the severity of dose loss can be explored in future work and may include coating the medicine cup with a material to reduce nonspecific binding of therapeutic molecules or modifying the shape of the medicine cup through post-design modifications, including adding dental acrylic to reduce dose residence space and improve the fraction that contacts aerosol-producing mechanisms.

This work identified methods for characterizing a N2B aerosol delivery protocol and pointed to obstacles to delivery in vivo. While primary sites of deposition were predicted, the details of the deposition patterns were not effectively predicted by the model, and therefore the phantom cannot be used to replace in vivo testing. Quantification of the delivered fraction is still required to determine device efficacy for the subjects of interest and can be achieved using the translational methods outlined here. Still, this approach may be useful to identify major barriers to success prior to lengthy animal studies. We believe this approach can be used to adapt existing, accessible technologies to new purposes and reduce barriers to access in the clinic.

REFERENCES

1. Alzheimer's Association. *Medications for Memory*. 2020; Available from: https://www.alz.org/alzheimers-dementia/treatments/medications-for-memory.

2. Bottros, M.M. and P.J. Christo, *Current perspectives on intrathecal drug delivery.* J Pain Res, 2014. **7**: p. 615-626.

3. Born, J., T. Lange, W. Kern, G.P. McGregor, U. Bickel, and H.L. Fehm, *Sniffing neuropeptides: a transnasal approach to the human brain.* Nat Neurosci, 2002. **5**(6): p. 514-516.

4. Crowe, T.P., M.H.W. Greenlee, A.G. Kanthasamy, and W.H. Hsu, *Mechanism of intranasal drug delivery directly to the brain.* Life Sci, 2018. **195**: p. 44-52.

5. Dhuria, S.V., L.R. Hanson, and W.H.I. Frey, *Intranasal delivery to the central nervous system: mechanisms and experimental considerations.* J Pharm Sci, 2010. **99**(4): p. 1654-1673.

6. Lochhead, J.J., K.L. Kellohen, P.T. Ronaldson, and T.P. Davis, *Distribution of insulin in trigeminal nerve and brain after intranasal administration.* Sci Rep, 2019. **9**(1): p. 2621.

7. Lochhead, J.J. and R.G. Thorne, *Intranasal delivery of biologics to the central nervous system.* Adv Drug Deliv Rev, 2012. **64**(7): p. 614-628.

8. Lochhead, J.J., D.J. Wolak, M.E. Pizzo, and R.G. Thorne, *Rapid transport within cerebral perivascular spaces underlies widespread tracer distribution in the brain after intranasal administration.* J Cereb Blood Flow Metab, 2015. **35**(3): p. 371-381.

9. Merlin, M.A., M. Saybolt, R. Kapitanyan, S.M. Alter, J. Jeges, J. Liu, S. Calabrese, K.O. Rynn, R. Perritt, and P.W. Pryor, 2nd, *Intranasal naloxone delivery is an alternative to intravenous naloxone for opioid overdoses.* Am J Emerg Med, 2010. **28**(3): p. 296-303.

10. Wermeling, D., *Intranasal Delivery of Antiepileptic Medications for Treatment of Seizures.* The American Society for Experimental NeuroTherapeutics, 2009. **6**: p. 352-358.

11. Veronesi, M.C., M. Alhamami, S.B. Miedema, Y. Yun, M. Ruiz-Cardozo, and M.W. Vannier, *Imaging of intranasal drug delivery to the brain.* Am J Nucl Med Mol Imaging, 2020. **10**: p. 1-31.

12. Erdo, F., L.A. Bors, D. Farkas, A. Bajza, and S. Gizurarson, *Evaluation of intranasal delivery route of drug administration for brain targeting.* Brain Res Bull, 2018. **143**: p. 155-170.

13. Kozlovskaya, L., M. Abou-Kaoud, and D. Stepensky, *Quantitative analysis of drug delivery to the brain via nasal route.* J Control Release, 2014. **189**: p. 133-140.

14. Haque, S., S. Md, J.K. Sahni, J. Ali, and S. Baboota, *Development and evaluation of brain targeted intranasal alginate nanoparticles for treatment of depression.* J Psychiatr Res, 2014. **48**(1): p. 1-12.

15. Bourganis, V., O. Kammona, A. Alexopoulos, and C. Kiparissides, *Recent advances in carrier mediated nose-to-brain delivery of pharmaceutics.* Eur J Pharm Biopharm, 2018. **128**: p. 337-362.

16. Reger, M.A., G.S. Watson, P.S. Green, L.D. Baker, B. Cholerton, M.A. Fishel, S.R. Plymate, M.M. Cherrier, G.D. Schellenberg, W.H. Frey II, and S. Craft, *Intranasal Insulin Administration Dose-Dependently Modulates Verbal Memory and Plasma β-Amyloid in Memory-Impaired Older Adults.* J Alzheimers Dis., 2008. **13**(3): p. 323-331.

17. Malinovsky, J.M., F. Servin, A. Cozian, J.Y. Lepage, and M. Pinaud, *Ketamine and norketamine plasma concentrations after i.v., nasal and rectal administration in children.* Br J Anaesth, 1996. **77**(2): p. 203-207.

18. Skulberg, A.K., A. Asberg, H.Z. Khiabani, H. Rostad, I. Tylleskar, and O. Dale, *Pharmacokinetics of a novel, approved, 1.4-mg intranasal naloxone formulation for reversal of opioid overdose-a randomized controlled trial.* Addiction, 2019. **114**(5): p. 859-867.

19. Malmros Olsson, E., P.A. Lonnqvist, C.O. Stiller, S. Eksborg, and S. Lundeberg, *Rapid systemic uptake of naloxone after intranasal administration in children.* Paediatr Anaesth, 2021. **31**(6): p. 631-636.

20. Craft, S., R. Raman, T.W. Chow, M.S. Rafii, C.K. Sun, R.A. Rissman, M.C. Donohue, J.B. Brewer, C. Jenkins, K. Harless, D. Gessert, and P.S. Aisen, *Safety, Efficacy, and Feasibility of Intranasal Insulin for the Treatment of Mild Cognitive Impairment and Alzheimer Disease Dementia: A Randomized Clinical Trial.* JAMA Neurol, 2020. **77**(9): p. 1099-1109.

21. Craft, S., L.D. Baker, T.J. Montine, S. Minoshima, G.S. Watson, A. Claxton, M. Arbuckle, M. Callaghan, E. Tsai, S.R. Plymate, P.S. Green, J. Leverenz, D. Cross, and B. Gerton, *Intranasal insulin therapy for Alzheimer disease and amnestic mild cognitive impairment: a pilot clinical trial.* Arch Neurol, 2012. **69**(1): p. 29-38.

22. Saccone, P.A., A.M. Lindsey, R.A. Koeppe, K.A. Zelenock, X. Shao, P. Sherman, C.A. Quesada, J.H. Woods, and P.J. Scott, *Intranasal Opioid Administration in Rhesus Monkeys: PET Imaging and Antinociception.* J Pharmacol Exp Ther, 2016. **359**(2): p. 366-373.

23. Rando, J., D. Broering, J.E. Olson, C. Marco, and S.B. Evans, *Intranasal naloxone administration by police first responders is associated with decreased opioid overdose deaths.* Am J Emerg Med, 2015. **33**(9): p. 1201-1204.

24. Freiherr, J., M. Hallschmid, W.H. Frey, 2nd, Y.F. Brunner, C.D. Chapman, C. Holscher, S. Craft, F.G. De Felice, and C. Benedict, *Intranasal insulin as a treatment for Alzheimer's disease: a review of basic research and clinical evidence.* CNS Drugs, 2013. **27**(7): p. 505-514.

25. Walsh, S., *FDA approves new nasal spray medication for treatment-resistant depression; available only at a certified doctor's office or clinic*. 2019: U.S. Food & Drug Adminitrastion Website.

26. Ryan, S.A. and R.B. Dunne, *Pharmacokinetic properties of intranasal and injectable formulations of naloxone for community use: a systematic review.* Pain Manag., 2018. **8**: p. 231-245.

27. Giroux, M., P. Hwang, and A. Prasad, *Controlled Particle Dispersion™: Applying Vortical Flow to Optimize Nasal Drug Deposition.* Drug Delivery Technology. **5**(3): p. 44-49.

28. Djupesland, P.G., *Nasal drug delivery devices: characteristics and performance in a clinical perspective-a review.* Drug Deliv Transl Res, 2013. **3**(1): p. 42-62.

29. Xi, J., Z. Wang, D. Nevorski, T. White, and Y. Zhou, *Nasal and Olfactory Deposition with Normal and Bidirectional Intranasal Delivery Techniques: In Vitro Tests and Numerical Simulations.* J Aerosol Med Pulm Drug Deliv, 2017. **30**(2): p. 118-131.

30. Xi, J., J.E. Yuan, Y. Zhang, D. Nevorski, Z. Wang, and Y. Zhou, *Visualization and Quantification of Nasal and Olfactory Deposition in a Sectional Adult Nasal Airway Cast.* Pharm Res, 2016. **33**(6): p. 1527-1541.

31. Chamanza, R. and J.A. Wright, *A Review of the Comparative Anatomy, Histology, Physiology and Pathology of the Nasal Cavity of Rats, Mice, Dogs and Non-human Primates. Relevance to Inhalation Toxicology and Human Health Risk Assessment.* J Comp Pathol, 2015. **153**(4): p. 287-314.

32. Chamanza, R., I. Taylor, M. Gregori, C. Hill, M. Swan, J. Goodchild, K. Goodchild, J. Schofield, M. Aldous, and V. Mowat, *Normal Anatomy, Histology, and Spontaneous Pathology of the Nasal Cavity of the Cynomolgus Monkey (Macaca fascicularis).* Toxicol Pathol, 2016. **44**(5): p. 636-654.

33. Plopper, C.G. and J. Harkema, *The Respiratory System and its Use in Research*, in *The Laboratory Primate*. 2005. p. 503-526.

34. Guenther, K., S. Yoganathan, R. Garofalo, T. Kawabata, T. Strack, R. Labiris, M. Dolovich, R. Chirakal, and J. Valliant, *Synthesis and in Vitro Evaluation of 18F- and 19F-Labeled Insulin: A New Radiotracer for PET-based Molecular Imaging Studies.* J Med Chem, 2006. **49**: p. 1466-1474.

35. Shai, Y., K. Kirk, M. Channing, B. Dunn, M. Lesniak, R. Eastman, R. Finn, J. Roth, and K. Jacobson, *18F-Labeled Insulin: A Prosthetic Group Methodology for Incorporation of a Positron Emitter into Peptides and Proteins.* Biochemistry, 1989. **28**: p. 4801-4806.

36. Kim, D.H., M. Blacker, and J.F. Valliant, *Preparation and evaluation of fluorine-18-labeled insulin as a molecular imaging probe for studying insulin receptor expression in tumors.* J Med Chem, 2014. **57**(9): p. 3678-3686.

37. Harkema, J.R., S.A. Carey, and J.G. Wagner, *The nose revisited: a brief review of the comparative structure, function, and toxicologic pathology of the nasal epithelium.* Toxicol Pathol, 2006. **34**(3): p. 252-269.

CHAPTER 5: PET IMAGING OF F-18-FB-INSULIN DELIVERED NOSE-TO-BRAIN IN PRIMATES

5.1 Background

Although the brain is not dependent on insulin for glucose metabolism, insulin plays a variety of critical roles in the brain. Insulin receptors (IRs) are widely and heterogeneously distributed throughout the brain[101]. IR expression has been found in every cell type of the CNS[102], including at particularly high densities in the dentate gyrus, hippocampus, hypothalamus, and olfactory bulb[103]. Central nervous system (CNS) insulin is implicated in the regulation of mood[2,102], metabolism[104], learning and memory, and neuroprotection, among many other functions[102]. For example, loss of IR and insulin-like growth factor-1 receptors (IGF-1R) in the hippocampus and amygdala lead to anxiety-like behavior[104] in mice, in alignment with findings that supplemental nose-to-brain (N2B) insulin improved mood in depressed subjects[105]. The same knockout mice displayed impaired metabolism and performance on cognitive tasks[104]. These findings agree with a body of literature demonstrating improved performance on metabolically demanding cognitive tasks following supplemental insulin exposure for individuals with[51,103,106-109] or without[110] disease.

Some have called Alzheimer's Disease (AD) the third type of diabetes due to its shared characteristics of insulin resistance and cognitive/emotional disturbances[111]. AD patients have higher plasma insulin and lower CSF levels in a pattern that intensifies with the severity of their clinical impairment[111]. This is exacerbated by lower levels of IRs in regions responsible for higher-order cognition as shown in post-mortem brain tissue[112]. Interestingly, dysregulation of insulin activity is not restricted to the CNS in AD – whole body insulin resistance is also lower for those in preclinical AD stages[113]. A study questioning insulin dysregulation as a driver of cognitive dysfunction demonstrated that patients recently diagnosed with type 2 diabetes or prediabetes (but not mild cognitive impairment) display regional hypometabolism patterns that match those in early AD, predominantly in the frontal, temporo-parietal, precuneus, and cingulate cortical areas[114]. It is unsurprising, then, that diabetes is a major risk factor for AD[2]. Given that supplemental insulin improves performance on memory tasks, mood, and glucose utilization in key processing areas, some have recommended the restoration of CNS insulin levels to that of healthy controls as a tool to manage AD symptoms[51,103] much like peripheral insulin for diabetes.

N2B delivery of insulin has gained attention as a route to noninvasively improve CSF insulin levels without perturbing peripheral insulin homeostasis. As an AD treatment, N2B insulin improved recall performance, capacity for self-care, and preserved performance on the cognitive subscale of the Alzheimer's Disease Assessment Scale (ADAS-cog). These improvements correlated with glucose utilization and arrest of atrophy in characteristic AD hypometabolic regions as determined by F-18-FDG PET[85] and MRI[107]. Inspired by the outcomes of N2B insulin clinical trials in patients with early AD[52,81,85,115,116], the National Institutes of Health has awarded substantial funding towards the development of N2B insulin as an AD treatment[52]. N2B insulin has several qualities that make it a desirable and convenient therapeutic beyond benefits to cognition. The intranasal route for therapeutics is attractive for its ability to overcome barriers associated with standard oral medication, reportedly improving patient compliance[117]. Insulin reached the CNS quickly, peaking significantly above baseline within 30 minutes of dosing and nearly doubling endogenous insulin concentration in the CSF following a 40 IU dose[68]. Perhaps most importantly after improved cognition, insulin afforded neuroprotection from amyloid-beta and phosphorylated tau, the pathophysiological hallmarks of AD, via engagement at the IR and its downstream signaling[118,119]. Overall, N2B insulin treatment has been associated with enhanced attention, memory, and other higher-order cognitive functions in subjects without perturbing peripheral insulin or glucose levels[52,69,120-122].

Efforts to demonstrate the clinical efficacy of N2B insulin as AD treatment have yielded inconclusive results. The most notable example comes from the Phase 2/3 clinical trial published by Suzanne Craft and others in 2020[51]. This study was intended to investigate the safety and efficacy of N2B insulin treatment for patients with AD or MCI over 12 months. Although the trial methods originally mirrored earlier studies that revealed efficacy for improving recall and cognitive preservation (ADAS-cog and Activities of Daily Living scale)[81,85,107], a surprise change in delivery device was needed due to inconsistent performance. The primary outcomes of the trial were derived from the patient group receiving insulin via the newer device (n=240). The results ultimately showed no benefit from N2B insulin on cognitive tests (4 administered), CSF biomarkers (4 tested), or cortical preservation from atrophy. However, those that received insulin via the original device (n=42), which had been previously validated by the same researchers, showed modest improvements in amyloid-beta clearance, improved performance on cognitive tests, and preserved hippocampal volume[51]. It is unclear whether the lack of treatment effect was a consequence of administration device design or technique[123], lack of efficacy of intranasal insulin, or something else. This study highlights the need to "verify… devices' ability to deliver

compounds to the central nervous system directly"[51]. Without a method to validate transfer from the device to the target site, there is no way to eliminate device performance as the source of treatment failure. However, tracking the distribution of small volumes through narrow, bony structures is challenging in living subjects.

A noninvasive method to track the deposition and transfer of N2B therapeutics in living subjects is needed. Positron emission tomography (PET) can noninvasively and quantitatively evaluate the kinetics of F-18-FB-insulin in deep tissues. Thus, we evaluated dynamic PET imaging as a method to characterize N2B F-18-fluorobenzoyl-insulin (F-18-FB-insulin) delivery, deposition, and brain uptake in non-human primates (NHPs). We piloted three F-18-FB-insulin delivery approaches using clinically relevant tools – one method delivering the radiolabeled insulin as in liquid form, and two delivering the radiotracer in aerosol form. F-18-FB-insulin localization following delivery was characterized using co-registered MR images and a Cynomolgus Macaque brain atlas. These methods were expected to highlight challenges to effective N2B delivery, which may help to eliminate ambiguity in future studies.

5.2 Materials and Methods

5.2.1 Synthesis of F-18-FB-insulin

F-18-FB-insulin was synthesized at Charles River Laboratories (Mattawan, Michigan, United States) via the same methods described in section .3.1, which are known to conserves receptor binding at affinity rates comparable to human recombinant insulin[99]. A summary of the radiochemistry results can be found in the Tables section (Appendix B).

5.2.2 Subject Preparation

Rhesus Macaques (1 male, 1 female) were used for aerosol delivery experiments, while Cynomolgus Macaques (1 male, 1 female) were used in experiments that delivered F-18-FB-insulin as a solution. The change to Cynomolgus was required due to pandemic supply chain issues. Subjects were assigned to experiments as shown in Table 5.1 (Appendix B), with order alternating by sex for each experiment.

Prior to dosing, the animal was given a loading dose of anesthesia (10 mg/kg intramuscular ketamine) and maintained under isoflurane to effect. Subjects were also intubated to minimize complications with ventilation. To minimize the delay between dosing and imaging, subjects were positioned in the Siemens MicroPET Focus 220 (Concorde Microsystems, Knoxville, Tennessee, United States) scanning bed and transferred to an adjacent room for the dosing procedure. All procedures involving animal subjects were conducted at Charles River Laboratories (Mattawan, Michigan, United States) and approved by their Testing Facility Institutional Animal Care and Use Committee.

5.2.3 F-18-FB-insulin Delivery to Subjects

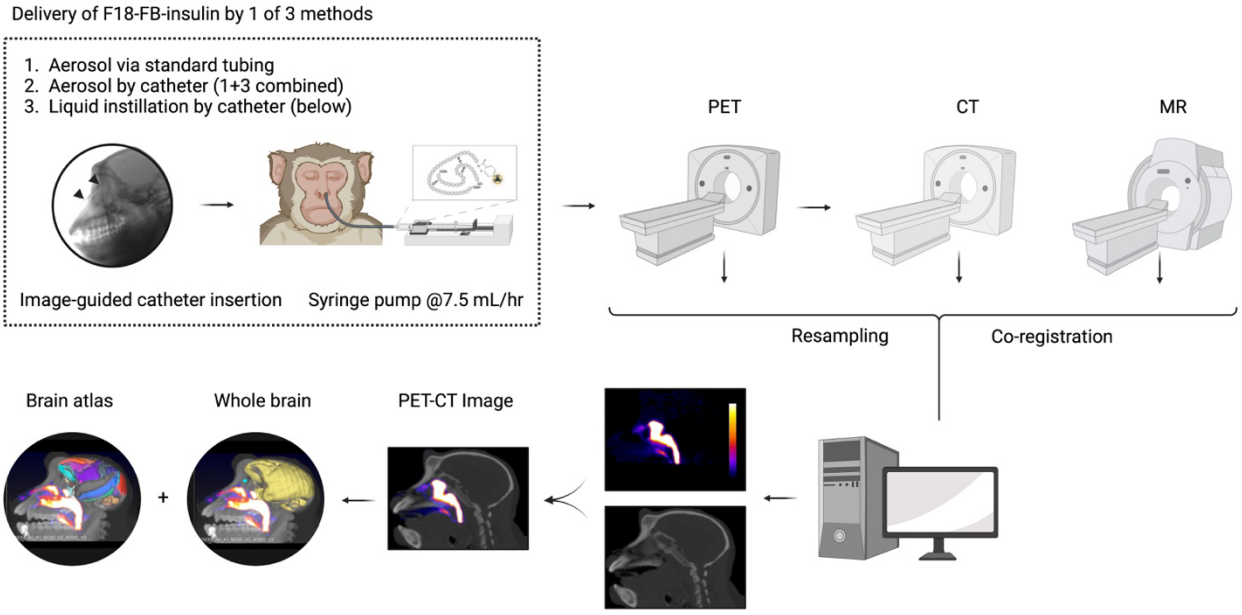

Figure 5.1. Workflow for F-18-FB-insulin dosing and imaging by dynamic PET and CT in Rhesus and Cynomolgus Macaques. Radiotracer was delivered in aerosol (Rhesus Macaques) or liquid (Cynomolgus Macaques) form prior to 120 minutes of dynamic PET imaging, followed by CT. The aerosol delivery tools and set-up can be viewed in Figure 4.3. PET, CT, and MR images (acquired separately) were resampled to uniform voxel size and co-registered for analysis. A fluoroscope was used to place the catheter used in delivery methods 2 and 3, which is visible between the black arrowheads in the dotted box. Example cribriform plate (green), whole brain (yellow), and brain atlas (multicolored) volumes of interest are shown. Atlas quantification was only performed in subjects receiving liquid dosing by catheter.

5.2.3.1 Delivery of F-18-FB-insulin as Aerosol via Standard Tubing

Delivery of aerosolized F-18-FB-insulin to the Rhesus Macaque nasal cavity was conducted using a modified Omron MicroAir vibrating mesh nebulizer (Omron Healthcare, Hoffman Estates,

Illinois, United States). The apparatus described in Figure 4.1 was used to deliver 450 mL of F-18-FB-insulin at 4.4 mCi (162.8 MBq, 52002 Ci/mmol at the end of synthesis) to the supine subject's left nare (5-minute delivery duration) as aerosol at 0.1 or 2 liter per minute (LPM) airflow based on optimization studies. A vacuum (40 LPM) was used to scavenge escaped aerosol from the primate's nares and mouth during dosing and direct it to a gas drying column for capture (filled 1:3 activated charcoal to desiccant). Immediately following dosing, the delivery apparatus was disassembled and the fraction of radiotracer deposition on each component was quantified via MicroPET Focus 120 (nebulizer cover, gas drying chamber) or dose calibrator (Biodex ATOMLAB 100 Plus or Capintec CRC-15).

5.2.3.2 Delivery of F-18-FB-insulin as Aerosol via Catheter

Rhesus Macaques were positioned prone on the bed of a OEC 9800 Plus C-arm fluoroscope (Skanray Americas, Romeo, MI, United States) for catheter placement. A surgeon from Charles River Laboratory used a rhinoscope to guide a 3.3f guide catheter with a radio-opaque tip (PediaVascular, Cleveland, Ohio, United States) and a 0.014 floppy wire to the ethmoid sinus, confirming placement via fluoroscope. The catheter was fitted to the dosing assembly with a shortened 1000 μL pipette tip to direct aerosolized F-18-FB-insulin to the target site with 0.5 mL/minute airflow, as identified in optimization studies (n=3). Aerosol was directed into one nostril. Three levels of vacuum were tested at the opposite nostril in efforts to mimic bidirectional flow in an anesthetized subject, which has demonstrated deposition in the upper nasal cavity[77,92]. In addition to the funnel vacuum placed above the subject's face to scavenge leaking aerosol, a nasal vacuum line was either inserted with a seal (high vacuum), positioned adjacent to the nostril with no seal (medium vacuum), or not included at all (low vacuum). The nasal vacuum line was joined with the funnel scavenging line and directed to a scavenging gas drying chamber with 40 LPM airflow as described previously. Dose lost to deposition on dosing components were quantified as a percentage of the administered dose as described earlier.

5.2.3.3 Delivery of F-18-FB-insulin as Liquid via Catheter

The same methods as described previously were used to place a catheter in the ethmoid sinus of Cynomolgus Macaques. The free end of the catheter was connected to a dose-filled syringe that delivered 450 μL of F8-FB-insulin as solution over 4 minutes by syringe pump (7.5 mL/hour rate). Immediately following dosing, subjects were transferred to the MicroPET Focus 220

scanning bed by study personnel and residual activity in the catheter was quantified by dose calibrator.

5.2.4 Imaging

Immediately following dosing, subjects were transferred to a MicroPET Focus 220 scanner for a 120-minute head-focused PET scan and subsequent computed tomography (CT) scan (120kVp, 4mAs, four seconds, 0.625 mm slice thickness, posterior possa filter) on the CERETOM NL3100 scanner (Neurologica, Danvers, Massachusetts, United States). Each subject underwent a single magnetic resonance (MR) imaging session to acquire a 3D T1 Fast Field Echo (FFE) sequence (T_E = 7.021 ms, T_R 14.13 ms, 2 mm slice thickness, 2 averages, flip angle = 8). Images were acquired using a 1.5T mobile MR scanner (Intera, Phillips Medical System).

5.2.5 Image Reconstruction and Co-registration

The PET images were reconstructed (OSEM 3D/MAP) into static (1x 120 minute summed bin) and dynamic (6x 0.5 minute, 3x 1 minute, 2x 2 minute, 22x 5 minute bins) series corrected for decay, scatter, and attenuation by CT. The imaging bed was removed from the CT images. PET and CT images were co-registered and resampled to uniform voxel size (0.6 mm^3) once the imaging bed was removed from the CT.

5.2.6 PET Image Analysis

Initial analyses consisted of F-18-FB-insulin quantification in the nasal cavity, cribriform plate, and brain in all subjects. Whole brain VOIs were determined using a species-specific 3D brain atlas provided by inviCRO (Boston, Massachusetts, United States), and a Charles River surgeon generated the cribriform plate VOI via skull segmentation. Iso-contouring was used to create a background VOI for each subject such that the remaining voxels represented activity present in the nasal cavity. If contamination on the exterior of the subject was observed, the contamination was accounted for using an iso-contoured VOI that was subtracted from the nasal cavity as well. The total administered dose was corrected by subtracting residual dose lost to dosing components from the starting dose. A mixed effects model (unequal n/condition) was used to test dosing method as a factor in residual dose lost to deposition in delivery components followed by a post-hoc Tukey's test to compare mean values directly.

F-18-FB-insulin was quantified in both static and dynamic PET reconstructions for these regions as percent of the total administered dose (also referred to as the injected dose or %ID), %ID/mm^3, and standard uptake values (SUV) in VivoQuant (inviCRO). SUV values are corrected for the subject body weight and VOI size, while %ID/mm^3 are only corrected for VOI size. For dynamic time-activity curves (TACs), mean and standard error of the mean (SEM) values were calculated per timepoint and delivery condition.

For the liquid delivery by catheter group, C_{max} and T_{max} were determined for the field of view, nasal cavity, cribriform plate, whole brain, and individual brain atlas regions as %ID, %ID/mm^3 atlas region volume, and SUV time-activity curves (TACs). Mean and standard error were calculated for SUV TACs, normalized SUV (nSUV) TACs, and C_{max} and T_{max} per region (n=48) and TAC type. For nSUV, activity in each atlas region was divided by the whole brain F-18-FB-insulin activity at the same timepoint. F-18-FB-insulin half-life was estimated for the nasal cavity, cribriform plate, and whole brain by fitting a one-phase decay model to averaged TACs (%ID/mm^3) via least squares regression in GraphPad Prism, starting from T_{max}=27 minutes post-dose onset. AUC was calculated as SUV*minutes for regional SUV time-activity curves, which are normalized by subject body weight. The area of a triangle from (0,0) to (12, F-18-FB-insulin activity$_{@\ T=12min}$) was added to the area under the curve for each region to correct for radiotracer transfer not captured by imaging. Mean, SEM, and AUC (SUV*minutes and VOI/Whole brain*minutes) values were calculated and plotted in GraphPad Prism. Regional AUCs were compared by Tukey's test for both measurements.

A translation was applied to the co-registered PET, CT, and MR images to improve orientation for viewing and figure generation. Iso-contouring was used to generate a CNS volume of interest based on the MR scan (cut-off value of 206 AU, restricted to intracranial and intravertebral compartment), which was only used to generate figures. PET voxels outside of the CNS volume of interest were set to zero to reduce spillover from radiotracer concentrated in the nasal cavity and improve visualization in the CNS for a subset of images. The batlowK colorbar was used[124] for the PET data, and grayscale for the CT and MRI. Images were generated in PMOD 4.2.

5.3 Results

5.3.1 Radiochemistry

Synthesis of F-18-FB-insulin was completed within 81 minutes on average (n=8), with a radiochemical yield of 11.5% (corrected for decay) and radiochemical purity 99.97%. With an average specific activity of 80,779 Ci/mmol (equivalent to 2,988,811.50 MBq/mmol), starting doses (0.45-0.9 mL) were 1.11 mCi on average. In one experiment, the full product was used due to low yield (0.3%, highlighted with a star in Tables 5.2 and 5.3). Synthesis results for each experiment can be viewed in section the Tables section (Appendix B).

5.3.2 Tubing Aerosol Delivery

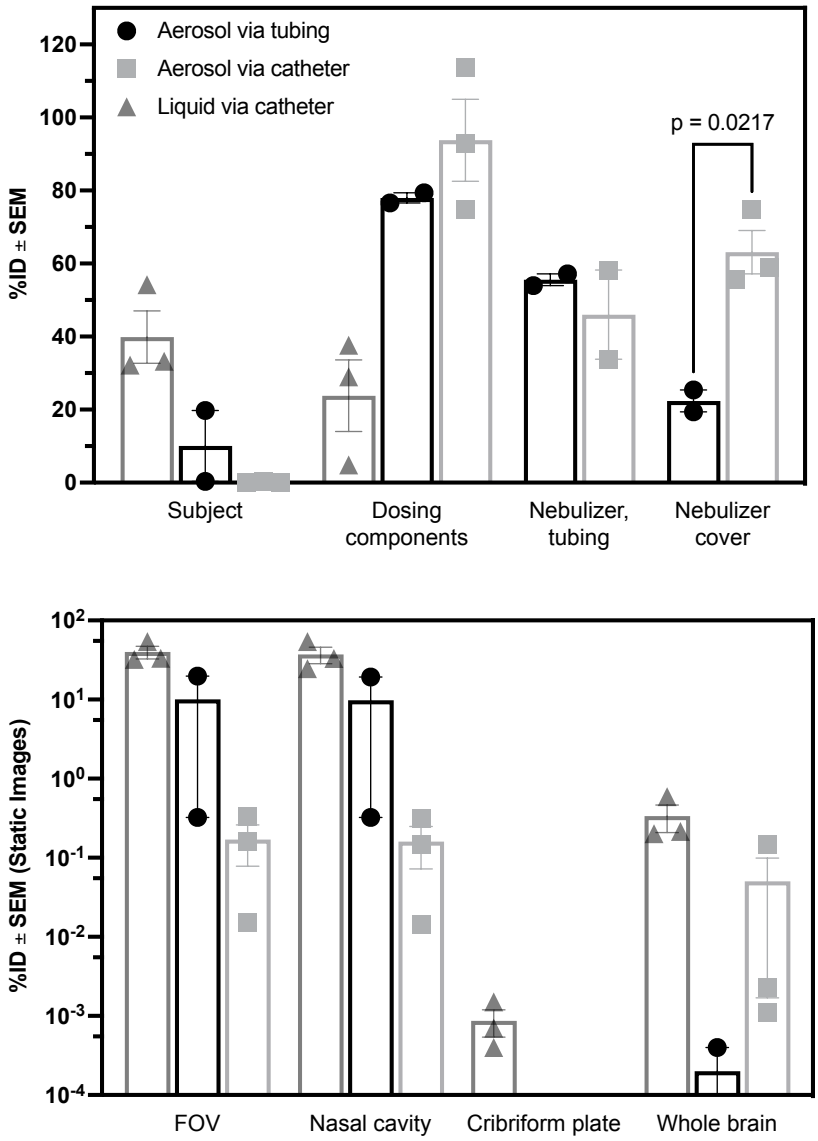

Figure 5.2. Summary of deposited radiotracer fraction in dosing components (top) and subject (bottom) for all delivery methods. Quantification of signal in subject determined by static PET images. For aerosol delivery experiments, the nebulizer and its accessories are included in the dosing components category. Values given as mean ± standard error (SEM).

Starting doses for aerosol delivery via standard tubing averaged 4.4 mCi (162.8 MBq, n=2), in which 10.0% (± 9.7 SEM) was detected in the field of view (FOV) per the static PET scan (Figure 5.2). Nearly half of the dose (55.6 ± 1.6 SEM) was lost to the loading syringe, nebulizer, and scavenging accessories. An additional 22.4% (± 3.0 SEM) was impacted in the nebulizer cover

and unavailable for delivery to the subject. Average deposition in the nasal cavity and brain were 9.8% (± 9.4 SEM) and $2.0x10^{-4}$% per static PET scans, respectively, for aerosol delivery by standard tubing. The subject that received F-18-FB-insulin aerosol via 2 LPM airflow achieved a C_{max} of 15.3% ID in the nasal cavity and 0.01% ID in the brain at t=16 minutes post-dose onset and decreased from there. No signal was observed in the cribriform plate of either subject, or the brain of the subject that received F-18-FB-insulin aerosol via 0.1 LPM airflow. Dose deposited in the subject was primarily concentrated in the anterior nasal cavity, distant from the targeted olfactory epithelium. F-18-FB-insulin did penetrate deeper into the nasal cavity with 0.1 LPM airflow, seen as accumulation at the rostral medial turbinate. It is important to note that nearly 500x the activity was detected in the FOV for the 2 LPM condition. Characterization of radiotracer distribution in CNS subregions was not pursued due to the low overall activity in the brain.

5.3.3 Catheter Aerosol Delivery

The average starting dose for aerosol delivery by catheter was 1.7 mCi (62.9 MBq, n=3). Only 1.9 μCi (± 1.0 SEM) was detected in the field of view (FOV) for the static PET reconstruction, amounting to 0.17% (± 0.09 SEM) of the starting dose (Figure 5.2). Aerosol accumulation on the surfaces of dosing components such as the loading syringe (20.5% ± 13.0 SEM), nebulizer (42.5% ± 7.1 SEM), nebulizer cover (46.05% ± 12.2 SEM) and scavenging components (0.09% ± .05 SEM) contributed to the low delivery efficiency.

A range of deposition patterns were observed in the nasal cavity. In the most successful case, F-18-FB-insulin can be seen in the superior meatus and distributed around the medial turbinate. In the worst case, which occurred under low vacuum conditions, F-18-FB-insulin is primarily observed on the exterior of the primate and was observed in the procedure room following dosing. Both cases were assumed to be contamination from aerosolized F-18-FB-insulin leakage from the dosing apparatus, as contamination by exhaled aerosol was not observed in other experiments.

Despite the low delivery efficiency, F-18-FB-insulin was detected in the brain of all subjects, albeit at low concentrations (range 0.0011-0.0047% ID). Nearly 8.7 million F-18-FB-insulin molecules were estimated in the brain (0.0027% ID ± 0.00011 SEM) per the static PET image and specific activity for the set of experiments. For the dynamic PET reconstructions, 0.47% (± 0.41 SEM) of

the delivered dose was detected in the nasal cavity (PET frame 1, 30 second duration) 12.5 minutes following dose onset. Nasal cavity C_{max} increased to 0.50% (± 0.41 SEM) with longer acquisition frames (1 minute) at 17 minutes post-dose onset. Brain C_{max} was $4.0x10^{-5}$% (± $2.2x10^{-5}$ SEM) at 38.57 minutes (± 9.28 SEM), but no F-18-FB-insulin was detected in the cribriform plate in any scan. As before, characterization of radiotracer distribution in CNS subregions was not pursued due to the low overall activity in the brain.

5.3.4 Catheter Liquid Delivery

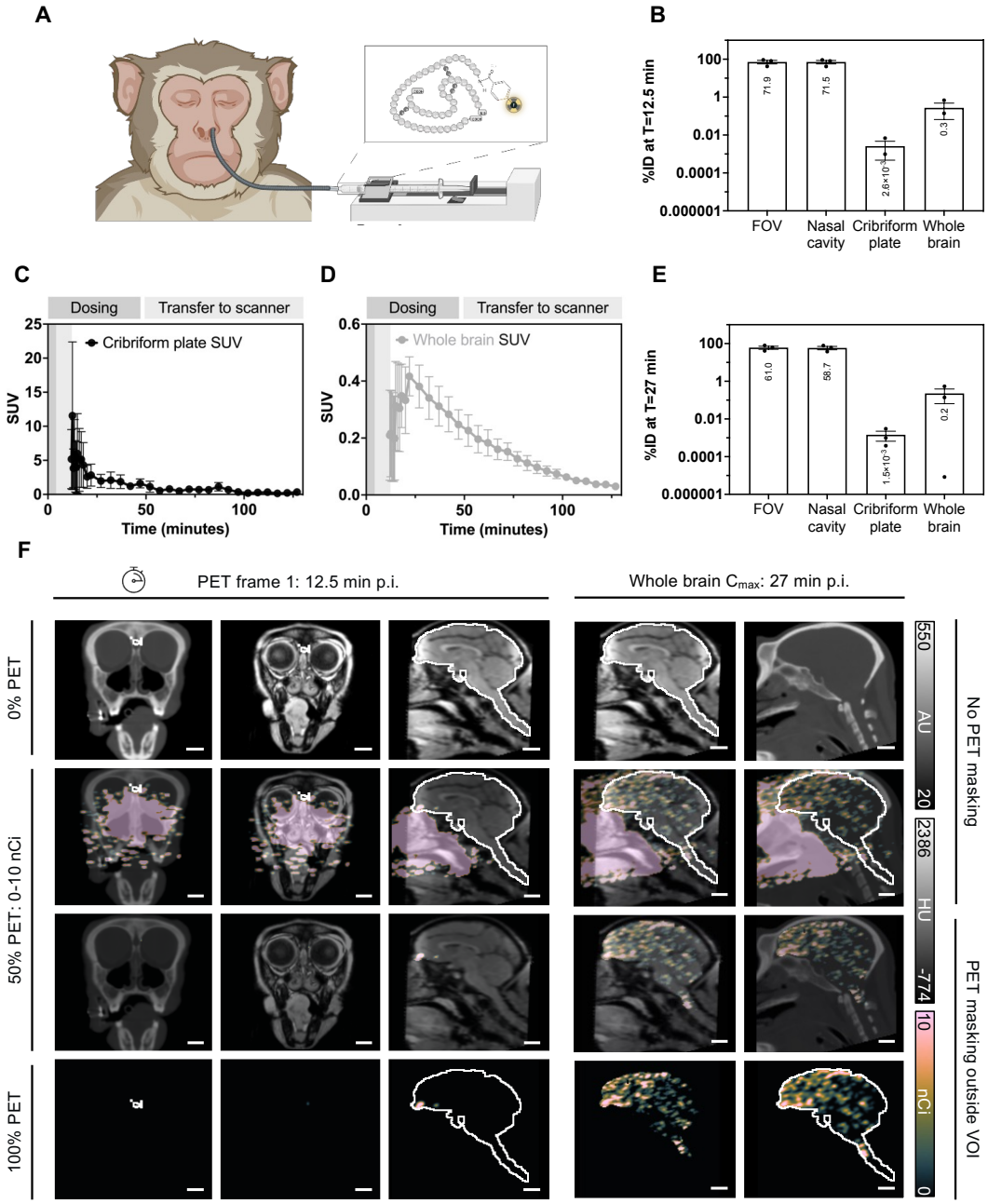

Figure 5.3. F-18-FB-insulin is detected in the cribriform plate and brain following delivery by catheter. The majority of radiotracer delivered in liquid form via catheter (A) is retained in the nasal cavity in the first PET frame (B). C-D. Radiotracer levels in cribriform plate (C) and whole brain (D) over time. E. Average quantification of F-18-FB-insulin in the PET FOV and sites of interest at t=27 minutes post-dose, where brain uptake is highest (C_{max}, n=3). D. Co-registered MR, CT, and PET images in coronal and sagittal slices at the first PET frame (left) and C_{max} (right) from a representative scan. The white VOI outlining the brain and spinal cord was used to mask all PET voxels outside the VOI to zero in rows 3 and 4 to improve visualization of F-18-FB-insulin in the CNS. The batlowK colorbar is used. Plots B-E given as mean ± standard error (SEM). %ID = Percentage of the administered dose, p.i = post administration onset. Scale bar = 1 cm.

Static PET reconstructions estimate F-18-FB-insulin in the nasal cavity, cribriform plate, and brain to be 37.21% (± 8.73 SEM), $8.6x10^{-4}$ % (± $3.6x10^{-4}$ SEM), and 0.34% (± 0.13 SEM) of the starting dose delivered to subjects by liquid instillation (367 μCi ± 254 SEM, Figure 5.2). In the first dynamic PET frame (t=12.5 minutes), 71.47% (± 15.18 SEM) of the delivered dose (%ID) was detected in the nasal cavity (Figure 5.3), accounting for 99.44% of the total signal in the FOV. At the same time, 0.0036% of PET-detected tracer was in the cribriform plate and 0.38% in the brain, accounting for 0.0026% (± 0.0021 SEM) and 0.27% (± 0.21 SEM) of the starting dose, respectively. On average, the whole brain time-activity curve (TAC) peaked at 0.69% ID (Figure 5.7 in Appendix B) within 27 minutes of dose onset, which constitutes 0.97% of the dose initially detected in the nasal cavity. Whole brain F-18-FB-insulin concentration was highest in the first PET frame for 2 of the 3 experiments, indicating that intranasally delivered insulin reaches the brain within 13 minutes of dosing. Interestingly, the 2 scans with SUV_{max} in the first frame were acquired in the female subject (T_{max} range for all brain regions = 12.5-22 minutes), while the male subject had a much wider T_{max} range (22-87 minutes for all brain regions) with the cribriform plate T_{max} lagging at 87-minutes post-dose. On average, F-18-FB-insulin concentration in the brain was 17-fold higher than the background of the scan.

The PET image was dominated by F-18-FB-insulin concentrated in the nasal cavity prior to masking outside of the CNS (Figure 5.3). Unlike the other F-18-FB-insulin administration methods tested, delivery of tracer in liquid form consistently distributed tracer through the nasal cavity, including to the upper nasal cavity where the olfactory epithelium is located. Tracer was observed primarily within the subject as viewed by CT (Figure 5.3F), although contamination was visible on the exterior of the head in one of the three subjects. Signal was observed in the cribriform plate in early PET frames. Doses with higher starting activities may help to visualize activity in different brain regions in the future.

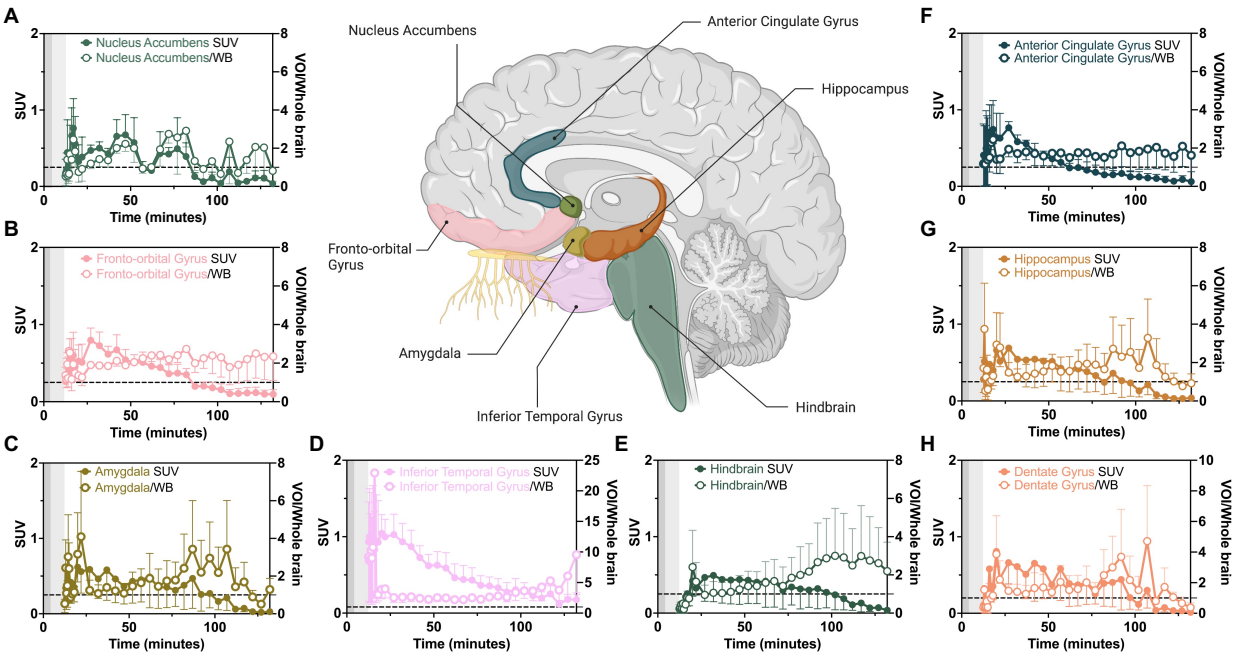

Figure 5.4. F-18-FB-insulin levels over time in brain atlas regions. Brain illustration highlighting the regions with the highest accumulation and their associated time-activity curves (TACs). The specific volumes of interest (VOI) are normalized to whole brain values at the same timepoint (unfilled symbol, right axis) and plotted with SUV over time (solid symbol, left axis). Plots give mean ± standard error (SEM). SEM (n=3) for A. Nucleus Accumbens, B. Fronto-orbital gyrus, C. Amygdala, D. Inferior Frontal Gyrus, E. Hindbrain (does not include Cerebellum), F. Anterior Cingulate Gyrus, G. Hippocampus, and H. Dentate Gyrus. High activity regions that composed of a combination of the regions highlighted in the figure (e.g. Forebrain, Limbic Lobe, Temporal Lobe) are not shown.

Accumulation and clearance of F-18-FB-insulin occurred at different rates for the various regions of interest. A one-phase decay model fit to averaged regional TACs indicate similar half-lives for the nasal cavity (29.95 min), cribriform plate (20.45 min), and whole brain (30.62 min). The decay model fit the averaged nasal cavity and whole brain TACs well ($R^2 > 0.99$), but less so for the cribriform plate ($R^2 < 0.90$), reflected in a wider confidence interval for the cribriform plate half-life (95% CI 13.12-31.45 min). Differences in F-18-FB-insulin kinetics were easily visualized in averaged nSUV atlas region TACs (VOI/whole brain, Figure 5.4). Half-lives quantified by the same approach (R^2 0.62-0.99) differentiate regions with high F-18-FB-availability into high-retaining regions and those with kinetics similar to the whole brain. For example, the fronto-orbital gyrus, inferior temporal gyrus, and anterior cingulate cortex demonstrated sustained activity above the whole brain concentration throughout the dynamic PET scan, but show steeper SUV clearance slopes than other regions highlighted in Figure 5.4. Alternatively, the amygdala, hindbrain, hippocampus, and dentate gyrus cleared tracer slower than the whole brain at later timepoints, demonstrated by their longer half-lives (mean range 40-55 minutes). The oscillating pattern

observed for the nucleus accumbens was unique among the other averaged TACs and was preserved across individual scans (Figure 5.4A).

F-18-FB-insulin accumulation was highest in the limbic lobe, forebrain, and temporal lobe. Within these regions, the F-18-FB-insulin exposure to the inferior temporal gyrus and fronto-orbital gyrus was 2-fold higher than was globally available in whole brain (Figure 5.5). Interestingly, the fronto-

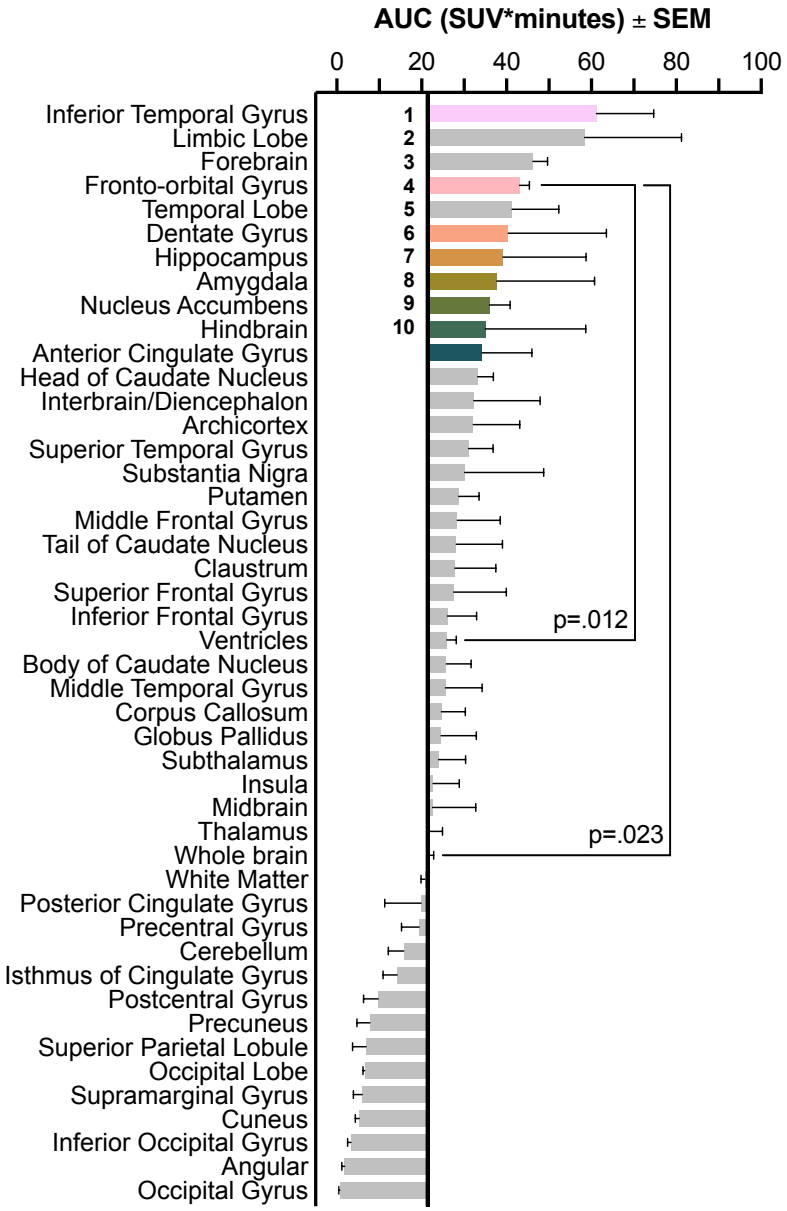

Figure 5.5. Brain atlas regions ranked from highest to lowest accumulation of F-18-FB-insulin. A. Mean AUC values (n=3) per VOI in rank order from largest to smallest. Significance determined by Tukey's test. Statistical differences were also found for the Forebrain and Nucleus Accumbens but are not highlighted on this plot for clarity.

orbital gyrus had statistically greater bioavailability than the ventricles, which is the primary sampling endpoint for intranasal delivery studies in humans and nonhuman primates. The dentate gyrus, hippocampus, amygdala, nucleus accumbens, and hindbrain also demonstrated high levels of accumulation. If nSUV TACs are used to calculate the AUC instead of the SUV TAC, the top 5-10 accumulating regions are reshuffled such that the anterior cingulate gyrus occupies a top 10 position (Figure 5.7 in Appendix B). Top regions for peak concentration (SUV_{max}) but not AUC (e.g., subthalamus, archicortex, and subregions of the caudate nucleus) may function as intranasal delivery through-ways that delivered material to other sites (Figure 5.8 in Appendix B). Conversely, there was consensus between the regions with the lowest AUC and SUV_{max} values, including the occipital gyrus through the postcentral gyrus regions in Figure 5.5.

5.4 Discussion

This work suggests that intranasal insulin acts at frontal, limbic, and medial temporal regions associated with neurodegeneration and cognitive dysfunction in mild cognitive impairment and Alzheimer's Disease, in agreement with prior studies. Although insulin was detected in all regions of the brain, F-18-FB-insulin was primarily delivered to limbic regions and those receiving olfactory nerve (CN I) projections. This finding is supportive of IN delivery as a promising route for AD therapeutics, as a recent study categorized AD patients primarily into "temporo-parietal" or "limbic-predominant" hypometabolic patterns[40]. Additionally, tau and amyloid aggregations initially appear near the entorhinal cortices and associated sites such as the amygdala, hippocampal, and parahippocampal regions[125]. These regions are known to receive CN 1 projections as well. Regions with high F-18-FB-insulin availability and long half-lives are suggestive of high binding rates and/or recycling of the radiotracer, which is in agreement with reports of high IR density in the hippocampus, amygdala, and other temporal regions[126]. With knowledge of insulin's neuroprotective effects, these results paint an optimistic picture for providing relief to patients struggling with cognitive impairment and slowing the rate of neurodegeneration through mitigation of damage induced by tau and amyloid-beta. Without inclusion of CSF, blood, or tissue sampling, we cannot make claims regarding the state or activity of F-18-FB-insulin these regions (whether bound, degraded, or recycled), but would like to include such methods in future efforts.

The quantitative nature of PET imaging enabled us to estimate F-18-FB-insulin concentration in specific regions of the CNS over time, compared to former research that relied on discrete cerebrospinal fluid sampling[68,127], behavioral assays[86], or post-mortem tissue analyses[127,128].

Interestingly, we show that CSF is not a primary accumulation site for N2B insulin, and that fronto-temporal structures receive substantially more of the peptide. The amount of insulin needed at the site of action to improve AD and MCI cognitive performance is not currently known. However, differences in CSF insulin concentration for AD patients and healthy controls helps to contextualize dosing needs. We found the ventricle C_{max} to be 0.010% ID (95% CI 0.006-0.013), which would amount to an addition of 23.9 picomol insulin to the CSF, assuming a 40 IU starting dose[51,85,107] and CSF volume of 0.13 L[129]. Contextually, assuming similar distribution patterns to those found in our study, this addition would increase CSF insulin concentration from 2.5 pM in a moderate/severe AD patient[130] to 186 pM, closing the gap between AD and healthy control levels 250-fold. Overall, we achieved a higher maximum uptake than reported in other N2B studies (C_{max} of 0.639% ID compared to 0.09%)[131], which may be due to our dosing approach and ability to capture earlier post-dose timepoints than in other studies[68]. Future studies can incorporate F-18-FB-insulin into the delivered dose and follow cognitive tasks to determine what levels of insulin are needed to induce desired effects, which may vary regionally depending on the AD subtype.

Earlier studies demonstrated a relationship between insulin resistance and reduced metabolic activity in the precuneus[114] that was preserved from progression following N2B treatment[85,107]. In contrast, we found that F-18-FB-insulin activity in the precuneus was among the lowest of the brain atlas regions, both over time and acutely (e.g. AUC and SUV_{max}), but was present (95% CI 0.00071-0.0066% ID, Figure 5.9). If our results are indeed representative of the intranasal insulin distribution we can expect in man, this may suggest that minor increases in insulin provide protective and/or therapeutic effects. However, unappreciated anatomical differences may exist for man and Cynomolgus Macaques that play a role in distribution to this site, which may explain the discrepancies between the studies. It is also possible that the referenced results were gathered from AD or MCI patients with parietal vulnerability, which was recently highlighted as a distinct pattern of degeneration[40]. The method we've outlined may help to answers such questions related to preferential delivery pathways and treatment responders versus non-responders.

Finally, IN insulin has been shown to travel to the CNS along olfactory and trigeminal (CN V) nerves[71,132], which terminate at regions we've identified as having high F-18-FB-insulin availability. CN I projections sites are reflected in this list, as CN I travels ventrally and caudally along the fronto-orbital gyrus before diverging to the amygdala and diffusely across the temporal lobe[128]. A recent neuroimaging study found that the anterior cingulate gyrus, fronto-orbital gyrus, inferior temporal gyrus, hippocampus, and amygdala are common to 4 olfactory processing pathways in

humans. Interestingly, the caudate was also named as a shared node between the 4 olfactory networks (top 10 in SUV_{max}), and the nucleus accumbens was found to be common to two pathways[133] (top 10 in AUC). These regions speak to 10 of the 11 regions with the highest AUC, in which the remaining region (hindbrain) is a known projection site of the trigeminal nerve (pons). To this end, our results are in good agreement with prior studies that implicate olfactory and trigeminal pathways in N2B transfer of insulin. However, connections between the olfactory bulb, fronto-orbital gyrus, and medial temporal lobe were found be disrupted in AD patients[134], and may reflect structural differences that hinder distribution of N2B insulin. This should be investigated in future experiments, as exclusion of patients with this presentation may eliminate potential confounds when validating efficacy of N2B insulin if distribution is impaired.

REFERENCES

1. Schulingkamp, R.J., T.C. Pagano, D. Hung, and R.B. Raffa, *Insulin receptors and insulin action in the brain: review and clinical implications.* Neuroscience & Biobehavioral Reviews, 2000. **24**(8): p. 855-872.

2. Arnold, S.E., Z. Arvanitakis, S.L. Macauley-Rambach, A.M. Koenig, H.Y. Wang, R.S. Ahima, S. Craft, S. Gandy, C. Buettner, L.E. Stoeckel, D.M. Holtzman, and D.M. Nathan, *Brain insulin resistance in type 2 diabetes and Alzheimer disease: concepts and conundrums.* Nat Rev Neurol, 2018. **14**(3): p. 168-181.

3. Craft, S., J. Newcomer, S. Kanne, S. D'agogo-Jack, P. Cryer, Y. Sheline, J. Luby, A. Dagogo-Jack, and A. Alderson, *Memory Improvement Following Induced Hyperinsulinemia in Alzheimer's Disease.* Neurobiology of Aging, 1996. **17**(1): p. 123-130.

4. *2023 Alzheimer's disease facts and figures.* Alzheimers Dement, 2023. **19**(4): p. 1598-1695.

5. Soto, M., W. Cai, M. Konishi, and C.R. Kahn, *Insulin signaling in the hippocampus and amygdala regulates metabolism and neurobehavior.* Proc Natl Acad Sci U S A, 2019. **116**(13): p. 6379-6384.

6. Pomytkin, I., J.P. Costa-Nunes, V. Kasatkin, E. Veniaminova, A. Demchenko, A. Lyundup, K.P. Lesch, E.D. Ponomarev, and T. Strekalova, *Insulin receptor in the brain: Mechanisms of activation and the role in the CNS pathology and treatment.* CNS Neurosci Ther, 2018. **24**(9): p. 763-774.

7. Benedict, C., M. Hallschmid, B. Schultes, J. Born, and W. Kern, *Intranasal insulin to improve memory function in humans.* Neuroendocrinology, 2007. **86**(2): p. 136-142.

8. Craft, S., A. Claxton, L.D. Baker, A.J. Hanson, B. Cholerton, E.H. Trittschuh, D. Dahl, E. Caulder, B. Neth, T.J. Montine, Y. Jung, J. Maldjian, C. Whitlow, and S. Friedman, *Effects of Regular and Long-Acting Insulin on Cognition and Alzheimer's Disease Biomarkers: A Pilot Clinical Trial.* J Alzheimers Dis, 2017. **57**(4): p. 1325-1334.

9. Craft, S., R. Raman, T.W. Chow, M.S. Rafii, C.K. Sun, R.A. Rissman, M.C. Donohue, J.B. Brewer, C. Jenkins, K. Harless, D. Gessert, and P.S. Aisen, *Safety, Efficacy, and Feasibility of Intranasal Insulin for the Treatment of Mild Cognitive Impairment and Alzheimer Disease Dementia: A Randomized Clinical Trial.* JAMA Neurol, 2020. **77**(9): p. 1099-1109.

10. McNay, E.C. and J. Pearson-Leary, *GluT4: A central player in hippocampal memory and brain insulin resistance.* Exp Neurol, 2020. **323**: p. 113076.

11. Pearson-Leary, J., V. Jahagirdar, J. Sage, and E.C. McNay, *Insulin modulates hippocampally-mediated spatial working memory via glucose transporter-4.* Behav Brain Res, 2018. **338**: p. 32-39.

12. Brunner, Y.F., A. Kofoet, C. Benedict, and J. Freiherr, *Central insulin administration improves odor-cued reactivation of spatial memory in young men.* J Clin Endocrinol Metab, 2015. **100**(1): p. 212-219.

13. Wickelgren, I., *Tracking Insulin to the Mind.* Science, 1998. **280**(5363): p. 517-519.

14. Frölich, L., D. Blum-Degen, H.-G. Bernstein, S. Engelsberger, J. Humrich, S. Laufer, D. Muschner, A. Thalheimer, A. Türk, S. Hoyer, R. Zöchling, K.W. Boissl, K. Jellinger, and P. Reiderer, *Brain insulin and insulin receptors in aging and sporadic Alzheimer's disease.* Journal of Neural Transmission, 1998. **105**: p. 423-438.

15. Rasgon, N.L., H.A. Kenna, T.E. Wroolie, R. Kelley, D. Silverman, J. Brooks, K.E. Williams, B.N. Powers, J. Hallmayer, and A. Reiss, *Insulin resistance and hippocampal volume in women at risk for Alzheimer's disease.* Neurobiol Aging, 2011. **32**(11): p. 1942-1948.

16. Baker, L.D., D.J. Cross, S. Minoshima, D. Belongia, G.S. Watson, and S. Craft, *Insulin resistance and Alzheimer-like reductions in regional cerebral glucose metabolism for cognitively normal adults with prediabetes or early type 2 diabetes.* Arch Neurol, 2011. **68**(1): p. 51-57.

17. Craft, S., L.D. Baker, T.J. Montine, S. Minoshima, G.S. Watson, A. Claxton, M. Arbuckle, M. Callaghan, E. Tsai, S.R. Plymate, P.S. Green, J. Leverenz, D. Cross, and B. Gerton, *Intranasal insulin therapy for Alzheimer disease and amnestic mild cognitive impairment: a pilot clinical trial.* Arch Neurol, 2012. **69**(1): p. 29-38.

18. Chapman, C.D., H.B. Schioth, C.A. Grillo, and C. Benedict, *Intranasal insulin in Alzheimer's disease: Food for thought.* Neuropharmacology, 2018. **136**(Pt B): p. 196-201.

19. Freiherr, J., M. Hallschmid, W.H. Frey, 2nd, Y.F. Brunner, C.D. Chapman, C. Holscher, S. Craft, F.G. De Felice, and C. Benedict, *Intranasal insulin as a treatment for Alzheimer's disease: a review of basic research and clinical evidence.* CNS Drugs, 2013. **27**(7): p. 505-514.

20. Henkin, R.I., *Intranasal insulin: from nose to brain.* Nutrition, 2010. **26**(6): p. 624-633.

21. Reger, M.A., G.S. Watson, P.S. Green, L.D. Baker, B. Cholerton, M.A. Fishel, S.R. Plymate, M.M. Cherrier, G.D. Schellenberg, W.H. Frey II, and S. Craft, *Intranasal Insulin Administration Dose-Dependently Modulates Verbal Memory and Plasma β-Amyloid in Memory-Impaired Older Adults.* J Alzheimers Dis., 2008. **13**(3): p. 323-331.

22. Villemagne, V.L., S. Burnham, P. Bourgeat, B. Brown, K.A. Ellis, O. Salvado, C. Szoeke, S.L. Macaulay, R. Martins, P. Maruff, D. Ames, C.C. Rowe, and C.L. Masters, *Amyloid β deposition, neurodegeneration, and cognitive decline in sporadic Alzheimer's disease: a prospective cohort study.* The Lancet Neurology, 2013. **12**(4): p. 357-367.

23. Born, J., T. Lange, W. Kern, G.P. McGregor, U. Bickel, and H.L. Fehm, *Sniffing neuropeptides: a transnasal approach to the human brain.* Nat Neurosci, 2002. **5**(6): p. 514-516.

24. De Felice, F.G., M.N. Vieira, T.R. Bomfim, H. Decker, P.T. Velasco, M.P. Lambert, K.L. Viola, W.Q. Zhao, S.T. Ferreira, and W.L. Klein, *Protection of synapses against Alzheimer's-linked toxins: insulin signaling prevents the pathogenic binding of Abeta oligomers.* Proc Natl Acad Sci U S A, 2009. **106**(6): p. 1971-1976.

25. Hong, M. and V.M. Lee, *Insulin and insulin-like growth factor-1 regulate tau phosphorylation in cultured human neurons.* J Biol Chem, 1997. **272**(31): p. 19547-19553.

26. Crowe, T.P., M.H.W. Greenlee, A.G. Kanthasamy, and W.H. Hsu, *Mechanism of intranasal drug delivery directly to the brain.* Life Sci, 2018. **195**: p. 44-52.

27. Jiang, Y., Y. Li, and X. Liu, *Intranasal delivery: circumventing the iron curtain to treat neurological disorders.* Expert Opin Drug Deliv, 2015. **12**(11): p. 1717-1725.

28. Kim, J.Y., A. Rasheed, S.J. Yoo, S.Y. Kim, B. Cho, G. Son, S.W. Yu, K.A. Chang, Y.H. Suh, and C. Moon, *Distinct amyloid precursor protein processing machineries of the olfactory system.* Biochem Biophys Res Commun, 2018. **495**(1): p. 533-538.

29. Md, S., S.K. Bhattmisra, F. Zeeshan, N. Shahzad, M.A. Mujtaba, V. Srikanth Meka, A. Radhakrishnan, P. Kesharwani, S. Baboota, and J. Ali, *Nano-carrier enabled drug delivery systems for nose to brain targeting for the treatment of neurodegenerative disorders.* Journal of Drug Delivery Science and Technology, 2018. **43**: p. 295-310.

30. George, J. *Alzheimer's Insulin Study Puzzles Researchers*. [Online Article] 2019 [cited 2019; Available from: https://www.medpagetoday.com/meetingcoverage/aaic/81116.

31. Kim, D.H., M. Blacker, and J.F. Valliant, *Preparation and evaluation of fluorine-18-labeled insulin as a molecular imaging probe for studying insulin receptor expression in tumors.* J Med Chem, 2014. **57**(9): p. 3678-3686.

32. Xi, J., Z. Wang, D. Nevorski, T. White, and Y. Zhou, *Nasal and Olfactory Deposition with Normal and Bidirectional Intranasal Delivery Techniques: In Vitro Tests and Numerical Simulations.* J Aerosol Med Pulm Drug Deliv, 2017. **30**(2): p. 118-131.

33. Erdo, F., L.A. Bors, D. Farkas, A. Bajza, and S. Gizurarson, *Evaluation of intranasal delivery route of drug administration for brain targeting.* Brain Res Bull, 2018. **143**: p. 155-170.

34. Crameri, F., G.E. Shephard, and P.J. Heron, *The misuse of colour in science communication.* Nat Commun, 2020. **11**(1): p. 5444.

35. Levin, F., D. Ferreira, C. Lange, M. Dyrba, E. Westman, R. Buchert, S.J. Teipel, M.J. Grothe, and I. Alzheimer's Disease Neuroimaging, *Data-driven FDG-PET subtypes of Alzheimer's disease-related neurodegeneration.* Alzheimers Res Ther, 2021. **13**(1): p. 49.

36. FDA, *TAUVID (F-18 flortaucipir)*, in *Package insert.* 2020, Eli Lilly and Company.

37. Unger, J.W., J.N. Livingston, and A.M. Moss, *Insulin receptors in the central nervous system: Localization, signalling mechanisms, and functional aspects.* Progress in Neurobiology, 1991. **35**: p. 343-362.

38. Freeman, S.M., S. Samineni, P.C. Allen, D. Stockinger, K.L. Bales, G.G. Hwa, and J.A. Roberts, *Plasma and CSF oxytocin levels after intranasal and intravenous oxytocin in awake macaques.* Psychoneuroendocrinology, 2016. **66**: p. 185-194.

39. Saccone, P.A., A.M. Lindsey, R.A. Koeppe, K.A. Zelenock, X. Shao, P. Sherman, C.A. Quesada, J.H. Woods, and P.J. Scott, *Intranasal Opioid Administration in Rhesus Monkeys: PET Imaging and Antinociception.* J Pharmacol Exp Ther, 2016. **359**(2): p. 366-373.

40. Allison, A.C., *The secondary olfactory areas in the human brain.* J Anat., 1954. **88**: p. 481-488.

41. Gray, S.M., R.I. Meijer, and E.J. Barrett, *Insulin regulates brain function, but how does it get there?* Diabetes, 2014. **63**(12): p. 3992-3997.

42. Craft, S., E. Peskind, M.W. Schwartz, G.D. Schellenberg, M. Raskind, and D. Porte, *Cerebrospinal fluid and plasma insulin levels in Alzheimer's Disease.* Neurology, 1998. **50**: p. 164-168.

43. Wang, Z., G. Xiong, W.C. Tsang, A.G. Schatzlein, and I.F. Uchegbu, *Nose-to-Brain Delivery.* J Pharmacol Exp Ther, 2019. **370**(3): p. 593-601.

44. Lochhead, J.J., K.L. Kellohen, P.T. Ronaldson, and T.P. Davis, *Distribution of insulin in trigeminal nerve and brain after intranasal administration.* Sci Rep, 2019. **9**(1): p. 2621.

45. Fan, L.W., K. Carter, A. Bhatt, and Y. Pang, *Rapid transport of insulin to the brain following intranasal administration in rats.* Neural Regen Res, 2019. **14**(6): p. 1046-1051.

46. Zhou, G., G. Lane, S.L. Cooper, T. Kahnt, and C. Zelano, *Characterizing functional pathways of the human olfactory system.* Elife, 2019. **8**.

47. Zou, Y.M., D. Lu, L.P. Liu, H.H. Zhang, and Y.Y. Zhou, *Olfactory dysfunction in Alzheimer's disease.* Neuropsychiatr Dis Treat, 2016. **12**: p. 869-875.

This appendix provides additional graphs and tables that are not required to understand the body of the text, by may be of interest.

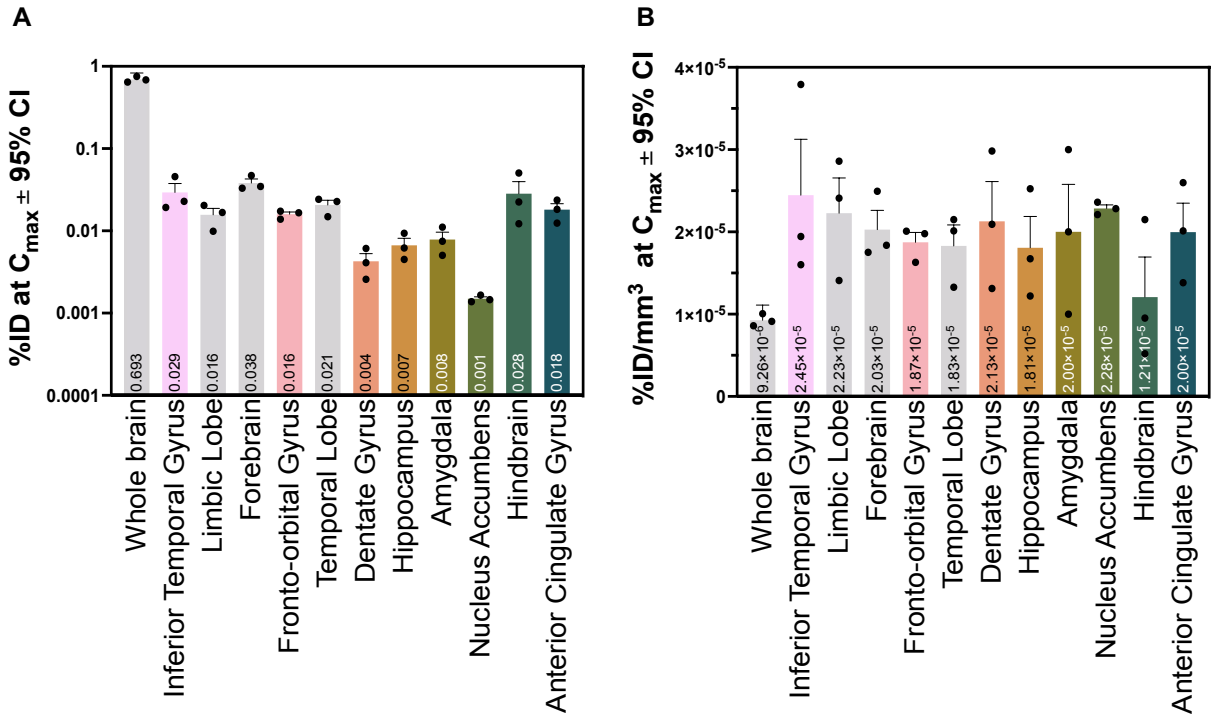

Figure 5.6. Max uptake of F-18-FB-insulin (Cmax) given for regions with highest bioavailability and whole brain as a percentage of the administered dose (%ID). Values in B have been normalized to the VOI volume. Plots given as mean ± 95% confidence interval (CI), with the mean in the bar for each region.

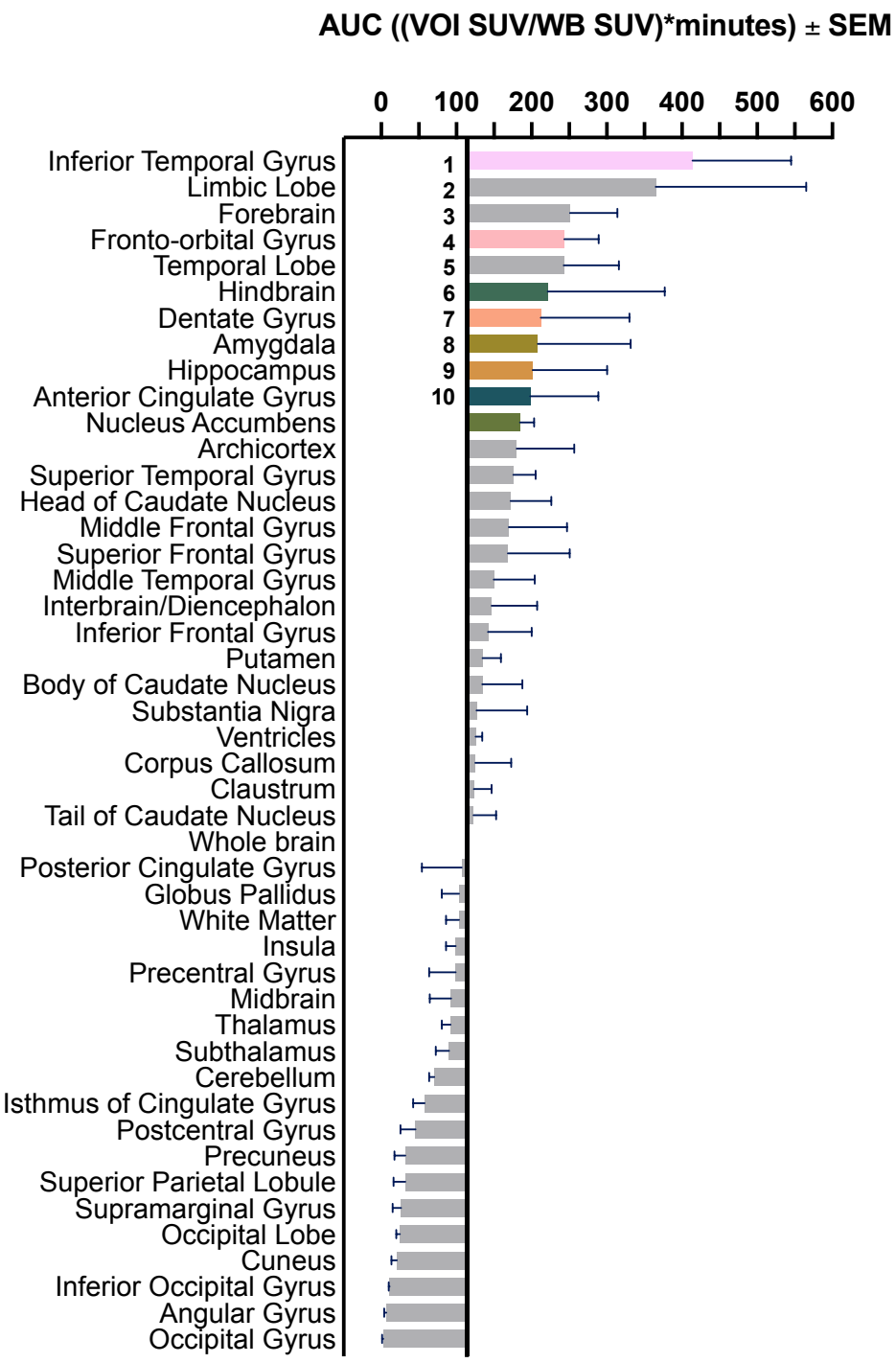

Figure 5.7. Brain atlas regions ranked from highest to lowest accumulation of F-18-FB-insulin. Analogous plot to Figure 4 with AUC values for whole brain normalized TACs given. Plot shows mean ± standard error (SEM).

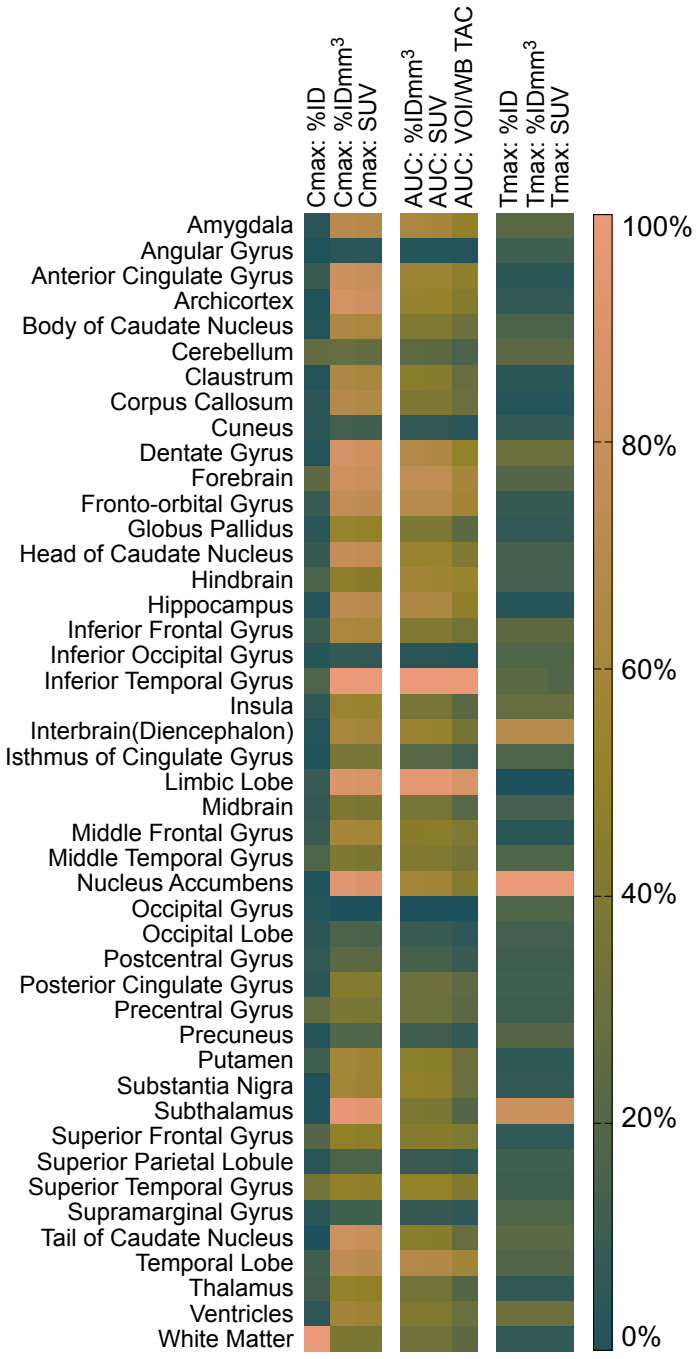

Figure 5.8. Summary of F-18-FB-insulin pharmacokinetics for brain atlas regions. C_{max}, AUC, and T_{max} given in different representations for comparison. Values are normalized to the maximum value (100%) per metric and plotted as a heat map. Colorbar is the batlow scientific color map truncated to the 40-80% range.

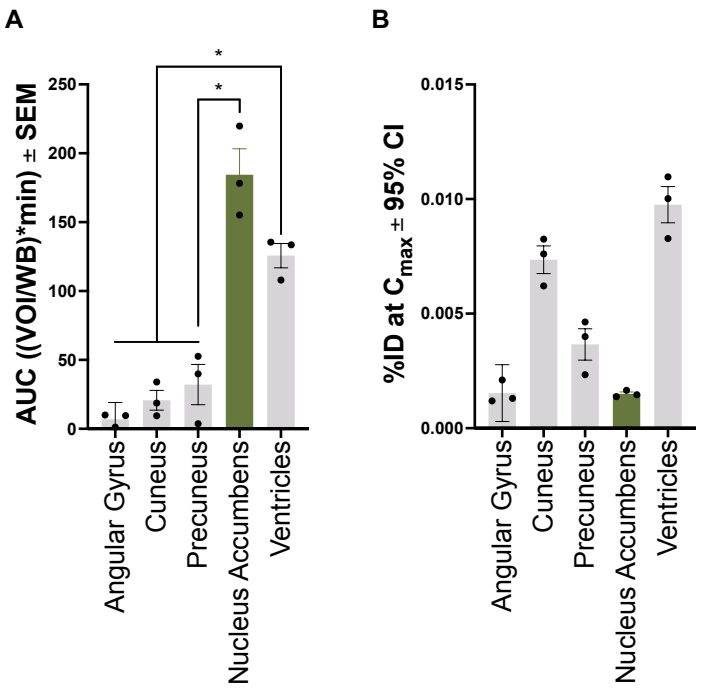

Figure 5.9. Max uptake (C_{max}) given for regions with statistical differences in exposure to F-18-FB-insulin as area under the curve (A) to illustrate real differences in insulin levels. A. The ratio of F-18-FB-insulin in the nucleus accumbens and ventricles (relative to whole brain) is statistically higher than the precuneus – a region of interest for AD and neuroprotection by intranasal insulin. B. At highest, peak F-18-FB-insulin levels are estimated to be above zero with 95% confidence (CI = confidence interval). Asterisks indicate $p < 0.05$ as determined by Tukey's test.

TABLES

Experiment	Species	Sex	Weight (kg)	Dose volume (mL)	Dose activity (μCi)
Aerosol delivery via standard tubing	Rhesus Macaque	M	6.1	0.45	1600.46
Aerosol delivery via catheter	Rhesus Macaque	M	7.4	0.45	971.31
Aerosol delivery via standard tubing	Rhesus Macaque	F	4.8	0.45	2516.68
Aerosol delivery via catheter (I)	Rhesus Macaque	F	5.1	0.60	202.40
Aerosol delivery via catheter (II)	Rhesus Macaque	F	5.2	0.45	1560.00
Liquid delivery via catheter*	Cynomolgus Macaque	M	5.5	0.90	78.65
Liquid delivery via catheter (I)	Cynomolgus Macaque	F	5.7	0.44	872.84
Liquid delivery via catheter (II)	Cynomolgus Macaque	F	5.8	0.50	148.98

Table 5.1. Subject assignment for experiments, organized by subject. Run order within experiments alternated by sex.

Date	Mean	SD	n	SEM	CI lower	CI upper
Total synthesis time (min)	80.88	7.83	8	2.77	75.73	86.02
Starting Activity (mCi)	116.88	72.23	8	25.54	69.38	164.37
Starting Activity (MBq)	4324.38	2672.53	8	944.88	2566.89	6081.86
Product Activity (mCi)	8.84	9.09	8	3.21	2.86	14.81
Product Activity (MBq)	326.75	336.32	8	118.91	105.59	547.91
Radiochemical Yield (%)	6.91	4.51	8	1.60	3.94	9.88
Decay-Corrected Yield (%)	11.50	7.45	8	2.63	6.60	16.40
Radiochemical Purity (%)	99.97	0.10	8	0.03	99.90	100.03
Concentration (mCi/mL)	8.55	8.19	8	2.90	3.16	13.94
Concentration (MBq/mL)	316.16	303.02	8	107.13	116.89	515.43
Total Volume (calculated)	1.50	1.13	8	0.40	0.76	2.24
Drug Concentration (µg/mL)	2.49	2.30	8	0.81	0.98	4.00
Drug Concentration (nmol/mL)	0.42	0.39	8	0.14	0.16	0.68
Total impurity assay (µg/mL)	31.01	30.32	8	10.72	11.06	50.95
Total impurity assay (nmol/mL)	5.23	5.11	8	1.81	1.87	8.59
Specific Activity (Ci/mmol)	80778.83	103807.66	8	36701.55	12513.95	149043.71
Specific Activity (MBq/mmol)	2988811.50	3840888.40	8	1357959.12	463007.54	5514615.46
Dose Activity (µCi)	1114.62	854.84	8	302.23	552.47	1676.77
Dose Activity (MBq)	41.24	31.63	8	11.18	20.44	62.04
Dose Volume (mL)	0.53	0.16	8	0.06	0.43	0.63

Table 5.2. Summary of F-18-FB-insulin synthesis results across all experiments. Due to the low yield, as much dose as possible was administered to the subject on 10/14/2021. CI lower and CI upper denote a 95% confidence interval range.

Date	3/26/20	9/15/20	4/22/21	5/13/21	7/2/21	10/14/21*	10/28/21	12/3/21
Start of Synthesis (SOS)	10:45	10:30	10:27	10:35	10:39	10:37	10:37	10:38
End of Synthesis (EOS)	12:11	11:49	11:51	11:51	11:49	11:56	12:13	11:55
Total synthesis time (min)	86	79	84	76	70	79	96	77
Starting Activity (mCi)	220	194	129	54	158	105	64	11
Starting Activity (MBq)	8140	7178	4773	1998	5846	3885	2368	407
Product Activity (mCi)	7.7	25.5	10.4	1.6	18.6	0.2	6	0.7
Product Activity (MBq)	285	944	383	59	688	7	222	26
Radiochemical Yield (%)	3.5	13.1	8	2.9	11.8	0.2	9.4	6.4
Decay-Corrected Yield (%)	6	21.6	13.6	4.7	18.3	0.3	17.2	10.3
Radiochemical Purity (%)	100	100	100	100	99.73	100	100	100
Concentration (mCi/mL)	17.9	19.207	8.436	1.284	16.5	0.046	4.427	0.581
Concentration (MBq/mL)	662.3	710.7	312.1	47.5	609.7	1.7	163.8	21.5
Total Volume (calculated)	0.4	1.3	1.2	1.2	1.1	4.2	1.4	1.2
Drug Concentration (μg/mL)	1.66	2.86	0.53	2.92	0.349	ND	6.62	ND
Drug Concentration (nmol/mL)	0.28	0.48	0.09	0.49	0.06	ND	1.12	ND
Total impurity assay (μg/mL)	63.09	11	6.52	15.33	13.99	ND	76.1	ND
Total impurity assay (nmol/mL)	10.64	1.86	1.1	2.58	2.36	ND	12.83	ND
Specific Activity (Ci/mmol)	64118	39886	93942	2612	280146	ND	3969	ND
Specific Activity (MBq/mmol)	2372350	1475766	3475864	96639	10365405	ND	146845	ND
Identity Test	Pass	Pass	Pass	Pass	Pass	Pass	Pass	Pass

Table 5.3. Metrics characterizing synthesis results of F-18-FB-insulin by experiment day. Due to the low yield, as much dose as possible was administered to the subject on 10/14/2021.

CHAPTER 6: CONCLUSIONS AND FUTURE DIRECTIONS

6.1 Overall Conclusions

Molecular imaging is a critical tool for the management of neurodegenerative disease. The use of positron emission tomography (PET) and magnetic resonance imaging (MRI) have helped to differentiate patients into Alzheimer's Disease (AD) subtypes, differentiate patients that may benefit from therapies from those that will not, and monitor treatment progression. However, the power of PET imaging is challenged by limitations in access that prevent its widespread adoption. Some of these limitations include the high cost of use, time and monetary costs for experiments and analysis, and low availability of sites equipped with the necessary instrumentation and personnel. The high cost of a failed study may be a barrier to further PET neuroimaging research that is desperately needed. This body of work introduced several methods to lessen that barrier through tools that reduce the risk associated with PET neuroimaging. By improving the efficiency of pre-clinical imaging, substantial savings are offered in experiment and personnel costs to explore and validate novel methods. By optimization dosing and imaging methods in subject models, potential pitfalls can be addressed in advance of expensive studies that could improve the likelihood of successful implementation. Solutions that utilize tools that are already approved for human use and are widely available to scientific professionals improve the likelihood of adoption by others, which is a major focus of the work.

6.1.1 Custom Tools for High Throughput PET Neuroimaging in Pre-clinical Models

These studies demonstrated high-throughput PET/MR imaging capable of sensitive quantification in phantoms, mice, and rats using the high-throughput accessory system that was designed, constructed, and validated for in vivo studies. The new system enabled rapid exchange of subject sets to quickly gather robust data from a large cohort of animals. The tools described were built from polyvinyl chloride (PVC) and 3D printed parts, which are low cost and accessible at many research institutions. This approach is beneficial in several ways. First, imaging more animals in a day reduces the number of days needed, reducing statistical error from experimental design. Second, subject staging was conducted only once for longitudinal imaging studies, eliminating a repeated, time-consuming task from the experiment. Third, cost to conduct the experiment was reduced by more than half, including hourly cost of instrument use, consumables, and personnel hours. Efficient and organized staging of animals was a benefit of this system that has the

potential to be widely applied across fields. Overall, this high throughput approach can serve as a platform to bolster future research by enabling quick-turnaround animal trials with increased efficiency and reduced error due to experimental design.

PET is more powerful in combination with other imaging modalities. Thus, consideration was given for how improvements to the high throughput imaging system could enable more widespread application for multi-modality imaging. Given that 3D printers are increasing in ubiquity and are inexpensive to use, common 3D-printed materials with desirable properties for pre-clinical research were screened for interference with common pre-clinical imaging modalities. Materials that were durable and did not interfere substantially with computed tomography, PET, or fluorescence imaging were identified. We additionally demonstrated that 3D prints made via stereolithography were preferred over fusion deposition modeling for radioactive decontamination. This information will be useful for those that wish to implement the methods described in Chapter 2, enabling researchers to select the most desirable materials for their 3D-printing applications.

6.1.2 Nose-to-brain Transfer of PET Agents for Neuroimaging

The use of anatomically informed models to pilot new dosing methods made it possible to identify unexpected challenges in nose to brain (N2B) aerosol delivery prior to the start of a costly in vivo study. The results presented in Chapter 4 outlined a stepwise approach to evaluate the performance of aerosol delivery tools using fluorescent and nuclear imaging agents to quantify deposition amounts and patterns. The utility of 3D printed nasal models to predicting primary sites of deposition in living subjects was demonstrated. Additionally, challenges posed by device design were identified, which could inform future collaborations between academia and industry to improve devices using evidence-based approaches. These methods could be applied to evaluate aerosol delivery products that may be unvalidated and planned for use in an upcoming study or adapted to a new application. This approach is intended to encourage biomedical scientists to explore new uses for existing devices, potentially reducing costs for specific-use devices, and reducing barriers to clinical translation.

Nose to brain transfer was achieved using existing clinical tools and was validated by PET neuroimaging in Cynomolgus Macaques. A range of methods to deliver F-18-FB-insulin to the primate nasal cavity were tested and the best method was identified. Ultimately, direct delivery of

radiotracer to the upper nasal cavity via catheter resulted in the greatest concentration in the brain, detected 27 minutes post-dose on average. F-18-FB-insulin was most available to limbic and fronto-temporal regions, which are vulnerable in several neurodegenerative diseases including AD. This work demonstrated the efficacy of a noninvasive and translatable method to track the fate of intranasal therapeutics following dosing and is believed to be broadly applicable for assessment of other therapeutic agents. With this technique, prevailing dose formulations, absorption enhancers, and/or delivery approaches can be identified and optimized to reduce the barriers to efficacious N2B therapeutics in the clinic.

6.2 Future Directions

All aspects of the research described in this dissertation were conducted with human translation in mind. Potential future efforts towards human translation are described below.

6.2.1 High Throughput Imaging Tools

Multi-modal imaging is a rapidly expanding subsegment of the growing clinical and pre-clinical imaging pre-clinical markets. Rising incidence rates of disease across the globe is a primary driver of growth in these markets and is expected to continue[58,61,135]. An additional driver of the imaging instrument marker is the need for improved efficiency of costly imaging systems, which could be achieved by improving the throughput of data acquisition or increasing the value of the instrument purchase. Augmentation to existing instruments with accessories that enable efficient data collection and enable end users to combine modalities with ease, possibly in novel ways, could improve the value of the instrument purchase. Given the existing needs and demonstrated utility of our high-throughput imaging system, future efforts will focus on the incorporation of findings outlined in Chapter 3 of this dissertation to make the tools widely applicable. In the regard, invention disclosures were made along with commercialization efforts as part of the MSU's MTRAC funding to enable future licensing to a key market player or launch a company that will sell the product, making it commercially available for use.

This product is expected to be highly valued by customers in this market according to end-user interviews and a value-in-use study. Pricing for the full product system (custom beds plus staging area) could be set between $3,000 and $6,000 according to the value-in-use study, split between the staging area ($1200) and an individual bed ($1200) to remain competitive. This estimate was

bolstered by the $3,000 average price point given by end-user interviewees when asked what they would be willing to spend for prototype #1 of the technology. Selling for $6,000 would render 91% of sales revenue as profit production cost for prototype #1, which cost $500 to make for the 8-bed set and is expected to be reduced for the new prototype. Further funding to evaluate alternative methods of production that may be faster and more cost-effective will be sought, which may support a lower price point for end users. Ultimately, commercialization of these tools is an important step towards dissemination of the methods described and an additional step towards reducing the barriers to PET neuroimaging research.

6.2.2 Nose-to-brain Transfer of PET Agents for Neuroimaging

6.2.2.1 Nonhuman Primate Nasal Cavity Phantom

Pilot studies using the nonhuman primate nasal cavity phantom were useful to develop the delivery method but have room for improvement in predictions for dose deposition amounts and patterns. The predictive power of the phantom was likely limited by its basis on a single subject, and the exclusion of the rest of the face. An improved model would be derived using input from several subjects and include the shape of the head/face using varying rigidities to reproduce malleable soft tissue. Additionally, this model was intended to simulate aerosol delivery to an anesthetized and intubated primate with no nasal breathing. Therefore, simulated breathing was not critical to our model. Researchers using the approach we outline to predict aerosol delivery to subjects with control over their breathing, like humans, may wish to simulate inhalation and exhalation in their phantom[136]. If these limitations are addressed, prediction of device efficacy in vivo may be improved.

6.2.2.2 Stability of F-18-FB-insulin Precursor

Although the F-18-FB-insulin product passed the identity test in all experiments, insulin quantification by integration of high-performance liquid chromatography (HPLC) traces proved difficult in two of the three final studies. This may be due to storage and/or stability conditions for the precursor compounds, as there were 18 months between the first and last dosing experiments. Investigating the stability of named compounds would be a worthy future direction, to increase shelf life and prioritize only the best reagents for experiments to encourage successful results and interpretation.

6.2.2.3 CSF and Blood Sampling

Future studies should prioritize quantification of F-18-FB-insulin post-dose in blood and cerebrospinal fluid samples. Confirmation by sampling in future studies will help to validate or correct image data and compare results to human trials. Additionally, the samples can be screened for degradation products to provide information about the pharmacodynamics of the tracer. The liquid F-18-FB-insulin catheter delivery approach outlined in this document can be used to address these questions.

Comparisons of dose compositions and administration routes as they relate to distribution profiles for F-18-FB-insulin would also be of interest. Although we intended to investigate factors with improve transfer to brain, this goal was de-prioritized to focus remaining experiments on achieving convincing transfer of F-18-FB-insulin to the brain. Similarly, evaluating the impact of dose formulation on stability and transport efficiency would be an important route of investigation. Both metrics have potential for improvement through the addition of stabilizers or absorption enhancers, respectively.

6.2.2.4 Translation to Humans

A natural next step would be to use the liquid delivery by catheter method to image F-18-FB-insulin in human subjects and evaluate transfer of insulin to various brain regions by this approach. One goal would be to validate the delivery device. Another goal of such a study would be to determine the effect of dose level on delivery, which has been unknown to this point. With knowledge of the percent dose deposited and percentage transferred to the brain, alternate delivery methods, formulations, etc. can be screened to determine optimal conditions for N2B transfer. Our method to calculate half-life in the nasal cavity can be used to identify methods that improve residence time, and therefore may improve transfer from nose to brain. These results could be used eventually to design a study that measures improvements in cognitive performance with insulin treatment.

The geometry of the nasal cavity is complex and influenced by biological and environmental factors that may not be controlled for in the clinic. For example, narrow nasal passageways may be further slimmed in a congested patient or obstructed in a patient with a deviated septum. These examples have potential to confound the results of a clinical study if they are not investigated in

advance, increasing the risk of misleading results for candidate intranasal therapeutics. Given that most studies reported in humans have administered intranasal insulin in an aerosolized form, which was found to be inefficient, care should be taken to eliminate factors that may render ambiguous results. Given the high success of liquid delivery by catheter, tools which support both targeted delivery of therapeutic to the upper nasal cavity and compliance in patients should be an area of focus for device development.

REFERENCES

1. *Global Small Animal Imaging Market $2.9 Billion by 2027*. Available from: https://www.ihealthcareanalyst.com/growing-demand-adoption-preclinical-multimodal-devices-small-animal-imaging-market/.

2. *Small Animal Imaging Market is Forecast to Reach a Value of US$ 4,879.3 Mn by 2028 at a CAGR of 8.6%*. Available from: https://www.einnews.com/pr_news/589732337/small-animal-imaging-market-is-forecast-to-reach-a-value-of-us-4-879-3-mn-by-2028-at-a-cagr-of-8-6-siemens-ag.

3. *Global Small Animal (In-Vivo) Imaging Market – Industry Trends and Forecast to 2029*. Available from: https://www.databridgemarketresearch.com/reports/global-small-animal-vivo-imaging-market.

4. Häubermann, S., A.G. Bailey, and C. Maul, *A System to Reproduce Human Breathing Patterns: Its Development and Validation.* Journal of Aerosol Medicine, 2000. **13**: p. 199-204.